Alma Mater Studiorum – Università di Bologna

DOTTORATO DI RICERCA IN

NANOSCIENZE PER LA MEDICINA E PER L'AMBIENTE

Ciclo 33°

Settore Concorsuale: 02/B1

Settore Scientifico Disciplinare: FIS/03

STUDIES OF THE CHARGE CARRIER DYNAMICS AND PHOTOELECTROCATALYTIC PROPERTIES OF V-MODIFIED TIO_2 THIN FILMS

Presentata da: Alberto Piccioni

Coordinatore Dottorato

Prof. Dario Braga

Supervisore

Prof. Federico Boscherini

Co-supervisore

Prof. Luca Pasquini

Esame finale anno 2021

TABLE OF CONTENTS

TABLE OF ACRONYSMS

AFM	Atomic Force Microscopy
CV	Cyclic Voltammetry
E	Electron
EDS	Energy Dispersive X-ray Spectroscopy
EIS	Electro-Impedance Spectroscopy
ESA	Experimental Station Alvra
EXAFS	Extended X-ray Absorption Fine Structure
FE	Free Electron
FEL	Free Electron Laser
FTAS	Femtosecond Transient Absorbance Spectroscopy
GPC	Gas Phase Condensation
IPCE	Incident Photon to current Conversion Efficiency
IRF	Instrument Response Function
NP	Nanoparticle
PEC	Photoelectrochemical
RF	Radio-Frequency
TAS	Transient Absorbance Spectroscopy
TE	Trapped Electron
TH	Trapped Hole
UV	Ultraviolet
XAFS	X-ray Absorption Fine Structure
XANES	X-ray Absorption Near Edge Spectroscopy
XES	X-ray Emission Spectroscopy

ABSTRACT

This thesis aims to study the modifications induced by the introduction of foreign elements, in particular vanadium (V), in titanium dioxide (TiO_2), an oxide semiconductor used for photoelectrocatalytic applications, such as water-splitting for hydrogen production and air and water remediation. The modification of this material is necessary to improve its conversion efficiency of light into chemical energy. In fact, its main limitation is the poor visible light absorption due to its wide energy gap, that ranges from 3.0 to 3.2 eV, depending on the polymorph. To sensitize TiO_2 to visible light, several strategies were adopted in the past years; among all, the introduction of elements such as 3d metals or non-metals in TiO_2 matrix turns out to be very effective.

In this work, V was introduced during the preparation of the sample, either in form of thin films or nanoparticles (NPs), using radio-frequency (RF) magnetron sputtering and inert gas phase condensation (GPC) technique, respectively. A structural characterization by X-ray diffraction (XRD), atomic force microscopy (AFM), Raman spectroscopy, and X-ray photoelectron spectroscopy (XPS) showed that V does not induce critical changes in TiO_2 matrix; X-ray near edge absorption spectroscopy (XANES) was used to determine the local environment of V and Ti, revealing that V is substitutional.

Understanding the consequences of such modification on the charge carrier dynamics is crucial for the improvement and development of new materials for photoelectrocatalytic applications. The mechanisms behind light absorption, charge transport and catalytic reactions take place over several orders of magnitude of time, from femtoseconds up to seconds. Every single process contributes to the final performance of the materials. In this thesis, to probe the very

first steps of the conversion process, femtosecond transient absorbance spectroscopy (FTAS) was adopted, to provide the basis for the interpretation of the photoelctrocatalytic behavior of V-modified and unmodified TiO_2, used as photoanodes in a photoelectrochemical (PEC) cell for water-splitting. In particular, three different pump wavelengths from ultra-violet (UV) to the visible range were used (300, 390, and 530 nm), in order to cover the relevant photoactive spectral range of modified TiO_2. FTAS clearly revealed that vanadium accelerates electron-hole recombination upon UV irradiation, explaining the lower incident photon-to-current conversion efficiency (IPCE) in the UV spectral range with respect to unmodified TiO_2. In the visible range, for modified samples, FTAS revealed the presence of a transient signal due to free electrons and trapped holes after pumping at 530 nm. These results were supported by the new photoelectrocatalytic activity in the visible range, which was attributed to a V-induced introduction of intragap levels at $\approx$ 2.2 eV below the bottom of the conduction band. Similar results were obtained for thin films and nanoparticle based samples. IPCE spectra showed that incorporation of vanadium in TiO_2 extends water splitting in the visible range up to $\approx$ 530 nm, a significant improvement compared to unmodified TiO_2 that is active only in the UV range $\lesssim$ 390 nm.

INTRODUCTION

In 2015, the United Nations Framework Convention on Climate Change (UNFCCC), among which there are European Union and its Member States, signed the so-called Paris Agreement, whose main goal is to face the global climate changes and to reach climate-neutrality before the end of the century. In particular, signatories agreed a long-term goal to keep global warming below 2 °C above pre-industrial level.[1] The boom of coal consumption, oil and gas to power the world's growing business activity, caused an average increment of the global temperature by 1 °C in the past 150 years, resulting in a large amounts of greenhouse gas emission. As a consequence, in the coming decades, the world faces a complex challenge, i.e. continue to grow economically while simultaneously reducing CO_2 emissions.[2]

So far, numerous governments and companies showed their desire to reach net-zero CO_2 emissions in the near future but there is a wide gap between these pledges and the current state of clean energy technology. While the technologies in use today can deliver a large amount of the emission reductions, they are insufficient on their own to bring the world to net zero emission and, as a consequence, energy efficiency and renewables are fundamental for achieving these climate goals. Much of these emissions, in fact, come from sectors where the technology options for reducing them are limited, such as shipping, trucks, aviation and heavy industries like steel, cement and chemicals; the decarbonization of these sectors will largely demand the development of new technologies. Many of the clean energy technologies available today need more work to bring down costs and accelerate deployment.[3]

As is often the case, there are no single or simple solutions to achieve the goal of net-zero emissions. Reducing global CO_2 emissions will require a broad range of different technologies in

all sectors of the economy, in various combinations and applications. There are four key technologies that are fundamental for reach net-zero emission:

- electrification of end-use sectors such as heating and transport,
- application of carbon capture, utilization and storage,
- use of bioenergy,
- the use of low-carbon hydrogen and hydrogen-derived fuels.

However, each of these areas faces challenges in making all parts of its value chain commercially viable in the sectors where reducing emissions is hardest.[3]

This is the global scenario in which hydrogen is going to play a key role for a clean, secure and affordable energy future. The advantages of hydrogen are well known: it is light, storable, reactive, has high energy content per unit mass, and can be readily produced at industrial scale.[4] However, widespread use of hydrogen in global energy transition faces several challenges. First of all, today, most of hydrogen is produced by natural gas, using a process called Steam Methane Reforming (SMR) that produces so-called "grey hydrogen"; under this definition there are all the techniques that require use of natural gas or coal, therefore emitting CO_2. The CO_2 emissions can be strongly reduced by CO_2 capture and storage (CCS), through which CO_2 is captured and injected in geological reservoirs or the ocean; in this case, we talk about "blue hydrogen".[5] Alternatively, hydrogen can be produced by electricity via water electrolysis. Using electricity from the grid or directly connected to renewables off-grid plants, electrolysis offers a flexible way to supply hydrogen. The latter solution also has the potential advantage of fully using green electricity and take advantage of falling renewable cost. The industry calls this "green hydrogen" since it only uses renewables sources, i.e. ones that do not generate CO_2 emissions.[2]

1.1 Hydrogen production via water electrolysis

Electrolysis is as a key means for enabling renewable energy penetration into all sectors, with electrolytic hydrogen being produced at, or transported to, the points of use. In addition, electrolysis enables increasing amounts of intermittent renewable energy to be connected to electricity grids, and also for storing renewable energy which is difficult or prohibitively expensive to connect to the grid, by capturing the surplus of energy generation that will be increasing in time.[6] In Figure 2.1 a schematic view of a possible green hydrogen production and utilization process is reported.

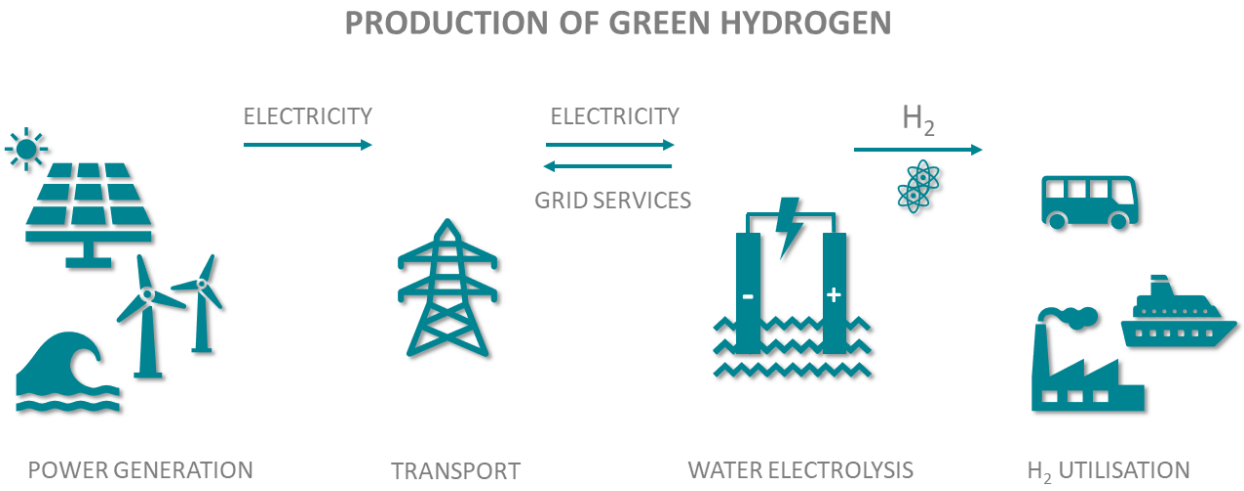

Figure 2.1: Green hydrogen production and utilization process.[7]

From a physical point of view, electrolysis is the process of using electricity to split water into hydrogen and oxygen. Commonly, this reaction takes place in a unit called electrolyzer, a device consisting in two noble metal-coated electrodes (cathode and anode) separated by an electrolyte or ionic conductor, which are powered by a continuous voltage supply in order to deliver the required energy to drive the water splitting chemical reaction.

This approach can be further improved by considering a direct solar water splitting process, called photoelectrochemical water splitting, in which solar energy is directly used to produce hydrogen without going through the intermediate electricity-production step. In this case it is even easier to consider hydrogen as stored solar energy in the form of chemical bonds, that can later directly or indirectly react with oxygen to release energy.[8] The water splitting process takes place in a photoelectrochemical (PEC) cell, in which the main component is the electrode made by an oxide semiconductor, which converts incident light into electron-hole pairs with enough energy to trigger the water splitting reaction and thus produces hydrogen and oxygen. This technique shares all the advantages with photovoltaic-electrolysis systems such as safety, chemical robustness and easily upscalable production process but it has one more potential advantage that is the possibility to enclose the whole process in a single monolithic device thus cutting the production costs.[9,10] Compared to separate photovoltaic and electrolyzer configurations, integrated photoelectrochemical devices have the potential to increase energy conversion efficiency and to reduce hydrogen cost. In particular, the target price per Kg of hydrogen should be in the range of \$2-\$4 to be competitive with steam-reformed hydrogen and more convenient than photovoltaic hydrogen, which is around \$8/Kg.[10]

1.2 Semiconductors for water splitting

The study of materials for water splitting began at the Bell Laboratories in the '50s during the early development of semiconducting materials for electronic devices. Bell Laboratories' researchers immersed in an aqueous solution different semiconductors such as Ge and TiO_2, finding out that the latter was able to evolve oxygen upon illumination. However, the real boom of the research in this field was during the energy crisis of the early 1970, and after the paper by Fujishima and Honda[11], which showed the connection between semiconductor photoelectrochemistry and solar

energy. In particular, they showed the possibility of splitting water and producing hydrogen by illuminating a TiO_2 electrode used as photoanodes in a PEC cell.

Since then, lots of studies and efforts were done in order to find the best material for this application. For direct photoelectrochemical decomposition of water to occur efficiently and sustainably, the electrode must fulfill several key tasks simultaneously: light absorption, charge separation, charge transport and hydrogen and oxygen evolution at its surface. In addition, the system must exhibit long-term stability against corrosion in aqueous electrolytes and have the potential to be made at low cost. So far, no cost-effective materials system satisfies all of these contradictory requirements listed above. This means that some trade-offs have to be made, in order to develop composite photoelectrodes in which different materials fulfill different functionalities.[12,13] The PEC research community is currently taking into account a broad spectrum of promising material classes and there is active research on different approaches such as modification of traditional materials, finding more practical synthesis techniques for expensive, high-performance materials and attempting to discover completely new materials systems.[14] The use of oxide semiconductors such as TiO_2, WO_3, Fe_2O_3, $BiWO_4$ as photoanodes can be considered a reasonable trade-off between costs and performances; they are cheap and really stable against photocorrosion. The main challenge for these materials is the combination of modest light absorption and, in some case poor charge transport properties. Solutions for these challenges have been recently proposed, such as use of mesoporous materials, heterojunctions, guest-host nanostructures, plasmonic effects and doping.

1.3 TiO_2 and its modifications for photocatalytic applications

Among all the oxide semiconductors for photocatalysis, titanium dioxide is one of the most studied since the discovery of its promising properties early in the ’70s by Honda and Fujishima.[11] It has most of the fundamental characteristics suitable for these kind of applications, such as:

- strong oxidation stability,
- stable in aqueous environment,
- non-toxicity,
- cost effective,
- good charge transport.

Thanks to these properties, it has many applications, that go from energy saving, production and accumulation, to environmental applications for air and water remediation.[15]

Titanium dioxide crystallizes in three main polymorphs: rutile, anatase and brookite. All of these polymorphs consist of deformed TiO_6 octahedra connected differently by corners and edges. In particular, anatase (space group $I4_1/amd$) can be considered to be built from octahedra that are connected by their corners, in rutile (space group $P4_2/mmm$), the edges are connected, and in brookite (space group Pbca), both corners and edges are connected (see Figure 2.2). Rutile is known to be the stable form, whereas anatase and brookite are metastable and they readily are transformed in rutile when heated.[16,17]

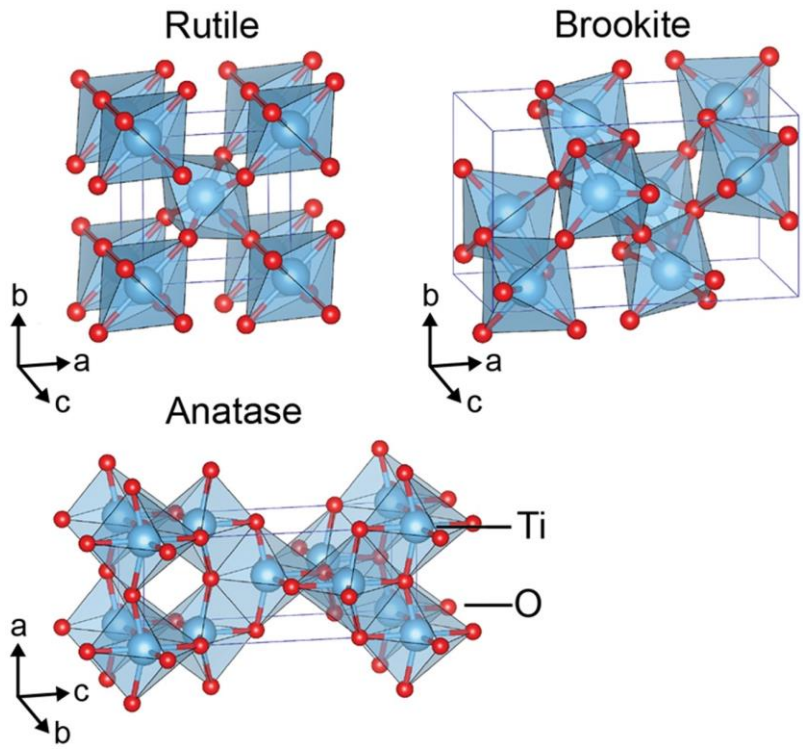

Figure 2.2:Crystal structures of TiO_2 rutile (tetragonal), brookite (orthorhombic) and anatase (tetragonal) polymorphs.[18]

For what concerns photoelectrocatalytic activity, anatase exhibits higher energy conversion performances than rutile, even though its energy gap is slightly larger (3.2 eV) with respect to rutile (3.0 eV).[17,19] However, these energy gap values allows TiO_2 to absorb only the UV part of the solar spectrum, which is just 5% of the total, reducing the conversion efficiency of photons into charge carriers available for photocatalysis. There are several strategies developed in recent years for improving TiO_2 photoelectrocatalytic performances, which aim to improve the overall conversion efficiency by acting in different processes like light absorption, charge transport and kinetics of redox reaction at the semiconductor interface. For example, optical absorption can be extended towards the visible light by modifying TiO_2 with metals (such as Ni, Cr, Mn, V, Fe)[20,21,22] and non-metals (N, S, C, F),[23,24,25,26] or by using plasmonic Au or Ag NPs.[27,28,29,30] Coupling TiO_2 with other materials like in heterojunction systems[31,32] can help the charge separation inside the

bulk and improve transport of charges. Finally, preparing the material in different nanostructured form (such as NPs, nanorods and porous thin films) increases the surface to bulk ratio and helps to gain more active area for triggering redox reactions.[33] During my PhD, I focused mainly on nano-structuring and modifying TiO_2 with a metal (V), studying advantages and disadvantages of these approaches. A key concept to keep in mind while modifying materials, is that the enhancement in one particular property may not be effective or, in the worst case, can even be even detrimental for another one. For example, the improvement of optical absorption does not always correspond to an enhanced photocatalytic activity in a previously inactive spectral range. In fact, absorption from intragap states (created by the introduction of substitutional 3d transition metals, see next paragraph) may not generate sufficiently strong oxidants for the desired reaction, meaning that the absorption spectrum of a photocatalyst does not necessarily match its photocatalytic activity spectrum. In addition, these foreign species can also induce charge carrier recombination or act as trapping sites for electrons or holes, eliminating all the benefits brought about by increased light absorption. During the modification process of a material, it is important to evaluate all the possible properties that are affected by this procedure. Advantages and disadvantages have to be considered carefully in order to gain a reliable overview of one modification approach with respect to another.

1.4 Overview of this thesis

In this thesis I am going to present the results obtained during my three years PhD course. I focused on the study of oxide semiconductor materials, in particular TiO_2, employed as photoelectrode in a photoelectrochemical cell for photocatalytic applications. Despite the advantages of this material, such as stability against corrosion in aqueous environments, good charge transport, abundance and thus cost-effectiveness, its main limitation is poor light absorption performance in the visible

range; since its band gap is around 3.2 eV (≅ 390 nm), it can absorb only 5% of the solar spectrum. The strategy here adopted to increase the absorption and conversion efficiency is modification with vanadium, a 3d transition metal. In fact, over the past years, this group of elements turned out to be very effective in extending the light absorption of wide band gap oxide semiconductor towards the visible spectrum, [21,31,34] by introducing occupied intra-gap energy levels that can be excited by photons with energy lower than the energy gap. In particular, V-modified TiO_2 showed that not only light absorption but also photocatalytic activity is extended towards the visible spectral range, thanks to the sufficient energy of holes and electrons produced by visible light to trigger the water splitting reaction.[35,36] Two different synthesis techniques were adopted: GPC for the synthesis of NPs-based photoelectrodes and RF magnetron sputtering for thin-film based photo-electrodes. The structural characterization was performed with X-ray XRD, Raman spectroscopy and XPS, while AFM was used for morphological characterization. Different visible spectroscopic techniques were used in order to study charge dynamics and photoelectrocatalytic performance: in particular FTAS was adopted to investigate how modification with a metal affects charge transport in the bulk after light excitation, providing the basis for the study of photoelectrocatalytic measurements. XAFS was adopted to study the local electronic structure of Ti and V. In the APPENDIX A, a feasibility study of ultrafast X-ray emission spectroscopy at the Alvra beamline at the SwissFEL is also presented. The combination of these advanced characterization and spectroscopic techniques was at the base of the research of my PhD activity, allowing to gain a clearer scenario on the structure, the morphology, the optical properties and the charge carriers dynamics in relation with photocatalytic activity in oxide semiconductors for photoelectrochemical applications.

2 PRINCIPLES OF PHOTOELECTROCATALYSIS

Photoelectrocatalysis is a complex and rich scientific field, bringing together fundamental concepts from chemistry, physics, electronics and thermodynamics. In addition to standard chemical processes involving interactions between chemical and ionic species, electrochemical processes can also involve interfacial interactions between ionic conductors, such as electrolyte solutions, and solid-state electronic conductors, such as semiconductors. Photoelectrochemical processes are based on electrochemical systems exposed to light, in which photons trigger the electrochemical reactions. In semiconductor photoelectrocatalysis, photons typically create electron–hole pairs within the semiconductor that can react with redox chemistry at semiconductor/electrolyte interfaces. Although a complicated set of fundamental electrochemical and solid-state optoelectronic principles govern the behaviour of these systems, there are few useful and basic concepts that can be helpful in providing a broad overview of the PEC water-splitting process, as I will show in this chapter.[14]

2.1 Oxide vs. covalent semiconductors

In order to understand why oxide semiconductor photoelectrodes are good candidates for photoelectrocatalytic applications, it is necessary to start from the properties of this class of materials, composed by transition metal and oxygen atoms, in particular a description of their electronic structure and band diagram. In most covalent semiconductors, such as Si and Ge, covalent bonding dominates. In silicon, for example, the outer 3s and 3p orbitals combine to form hybrid sp^3 orbitals. Neighboring sp^3 orbitals interact to form bonding and antibonding combinations that form the valence and conduction bands of the material, respectively. The bonding in metal oxide semiconductors is very different in nature. Since oxygen has a much higher

electronegativity than any metal, the valence electrons are fully or partially transferred from the metal ion to the oxygen. The bonding character of metal oxides is therefore highly polar or even ionic. A qualitative band picture can be obtained by constructing a molecular orbital (MO) diagram from the individual atomic energy levels. Figure 2.1 shows an example for rutile TiO_2.

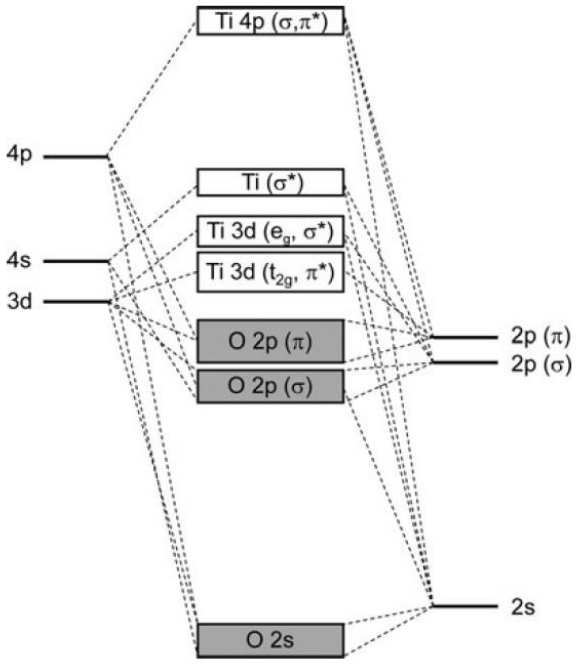

Figure 2.1: Molecular orbital diagram of rutile TiO_2.[12]

The main features of the MO diagram correspond quite well to the calculated band structure for rutile TiO_2, which is shown in Figure 2.2. The valence band is mainly composed of O-2p orbitals, whereas the conduction band is primarily Ti-3d in character. One can think of the valence band as being occupied with the electrons that originally resided on the titanium atoms, before they were transferred to the more electronegative oxygen during the formation of the bond. It should be noted that such a "local" view is inappropriate for covalent semiconductors such as silicon, in which the electrons are completely delocalized over the material. This local vs.

delocalized view is a key feature that distinguishes metal oxide semiconductors from their covalently bonded counterparts.

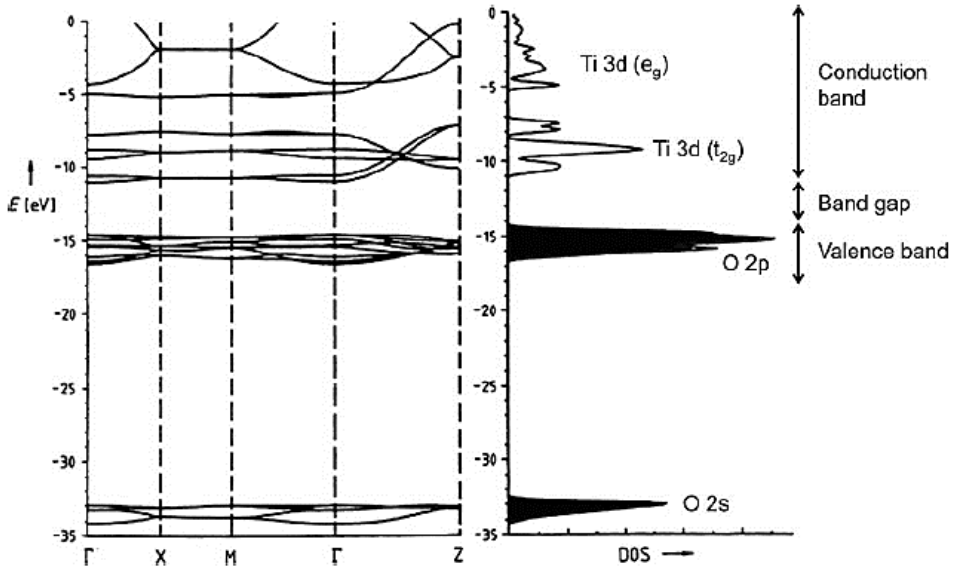

Figure 2.2: Electronic band structure and density-of-states (DOS) of rutile TiO_2. The black parts of the DOS indicate completely filled bands.[12]

2.2 Principles of photoelectrochemical water-splitting

The fundamental operation principles of a photoelectrochemical process are shown in Figure 2.3. In the following, the description of the operating principles of a simple two electrodes cell, composed by a photoanode and a metal counter electrode, is reported. The main component of this system is the photo-sensitive semiconductor that constitutes the working electrode of the cell. It is immersed in an aqueous solution and externally connected with an electrical wire to the counter electrode, usually made of platinum, and immersed in the electrolyte as well. When photons with sufficient energy hit the semiconductor, electron-hole pairs are generated, and they are spatially separated from each other by the electric field present inside the semiconductor at the electrolyte interface (see paragraph 2.3). The photogenerated electrons are swept toward the back contact and

then transported to the counter electrode via the external connection, where they drive the hydrogen-evolution reaction (HER) at the surface.

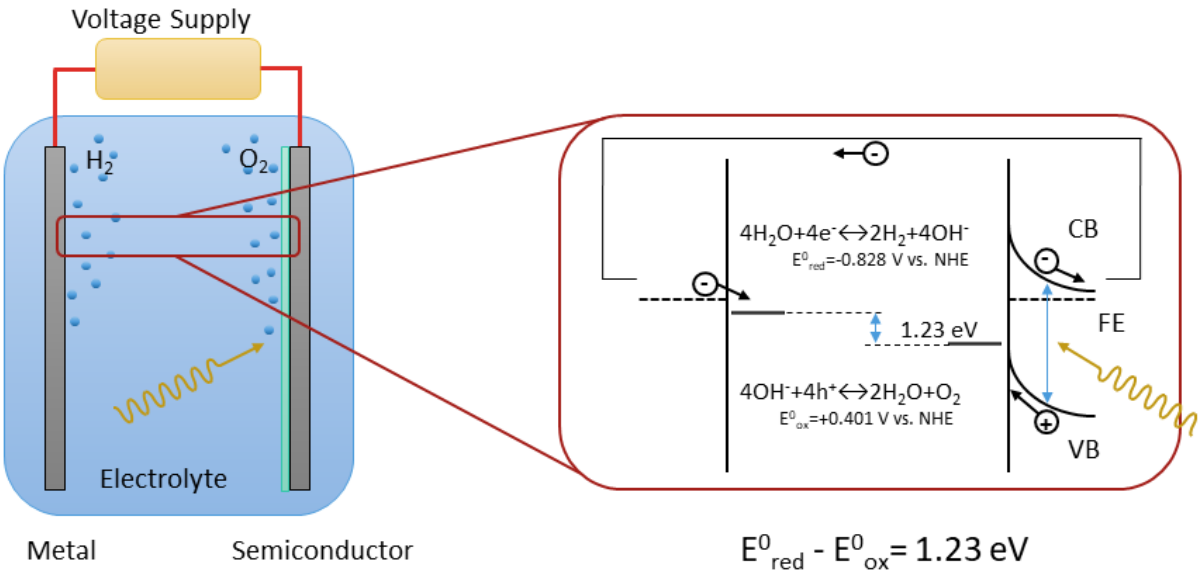

Figure 2.3: Sketch of a photoelectrochemical cell consisting in a photoanode semiconductor electrode and a metal counter electrode. On the right the band diagram of the system is reported.

On the contrary, photogenerated holes are swept toward the interface with the electrolyte where they drive the oxygen-evolution reaction (OER) at the anode surface. These two separated reactions can be modeled as two electrochemical half-reactions. Both must be sustained simultaneously, coupled by their exchange of electrons in the solid state and ions in the solution. Considering the case of an alkaline electrolyte, the reduction and oxidation reactions can be written as:

$$4H_2O + 4e^- \leftrightarrow 2H_2 + 4OH^- \qquad E^0_{red} = -0.828\,V\ vs.\ NHE \tag{1}$$

$$4HO^- + 4h^+ \leftrightarrow 2H_2O + O_2 \qquad E^0_{ox} = +0.401\,V\ vs.\ NHE \tag{2}$$

The Gibbs free energy change for the overall water splitting process is $\Delta G° = +237.18$ kJ/mol and represents a thermodynamic minimum for splitting water into its constituent gases at standard conditions of 25 °C and 1 bar. Since it is positive, energy needs to be supplied to drive the electrolysis process. The corresponding potential is $\Delta E° = E^0_{red} - E^0_{ox} =$ -1.229 V, meaning that the energy gap has to be at least 1.229 eV. However, this value does not take into account unavoidable energy process losses at anode and cathode or in solution, that can increase the actual energy gap needed by tenths of eV.[14]

2.3 The semiconductor-electrolyte interface

When a semiconductor is placed in contact with an electrolyte, like in the case of a PEC cell, electric current initially flows across the junction until electronic equilibrium is reached, a condition in which the Fermi energy (E_f) of the electrons in the solid is equal to the redox potential of the electrolyte (E_{redox}), as shown in Figure 2.4. The transfer of electric charge produces a region on each side of the junction in which the charge distribution differs from the bulk material which is known as the space-charge layer. On the electrolyte side, this corresponds to the familiar electrolytic double layer, that is the compact Helmholtz layer (2-5 Å) followed by the diffuse Gouy–Chapman layer (tens of Å). On the semiconductor side of the junction, the bending of the band depends on the position of the Fermi level in the solid. If the Fermi level of the electrode is equal to the flat band potential, there is no excess charge on either side of the junction and the bands are “flat”. If electrons accumulate at the semiconductor side one obtains an accumulation layer. If, however, they move from the solid into the solution, a depletion layer is formed, leaving behind a positive excess charge formed by immobile ionized donor states.

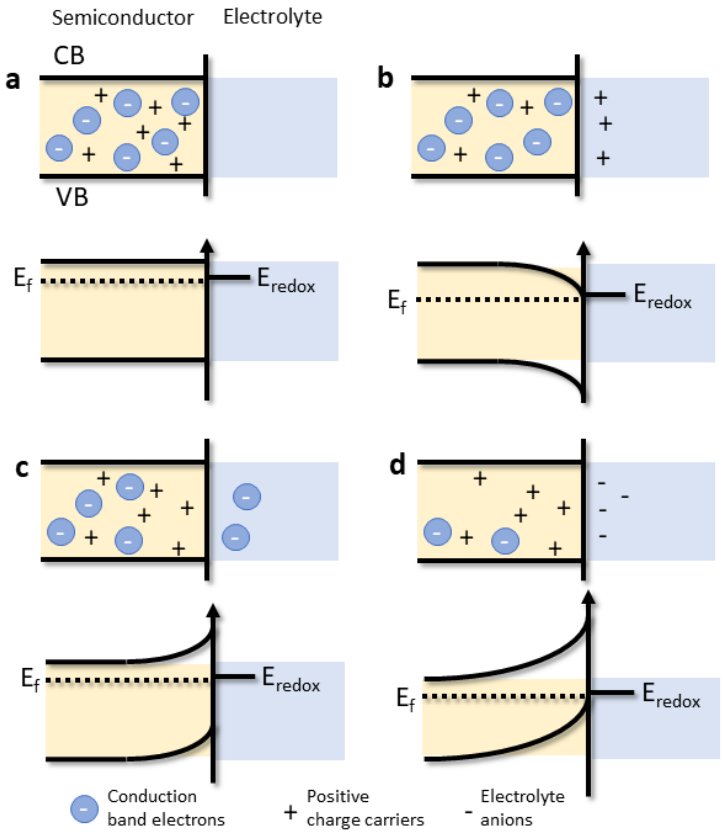

Figure 2.4: Schematic showing the electronic energy levels at the interface between an n-type semiconductor and an electrolyte containing a redox couple. For every case the band diagram and the correspondent charge distribution is reported. The four cases indicated are: a) flat band potential, a condition in which no space-charge layer exists in the semiconductor; b) accumulation layer, in which excess electrons have been injected into the solid producing a downward bending of the conduction and valence band towards the interface; c) depletion layer, in which electrons have moved from the semiconductor to the electrolyte, producing an upward bending of the bands; and d) inversion layer in which the electrons have been depleted below their intrinsic level, enhancing the upward band bending and rendering the semiconductor p-type at the surface.

Finally, the electron depletion can go so far that their concentration at the interface falls below the intrinsic level. As a consequence, the semiconductor is p-type at the surface and n-type in the bulk, corresponding to an inversion layer. The sketch in Figure 2.5 refers to n-type materials in which electrons are the mobile charge carriers. For p-type semiconductors, analogous considerations apply. In this case, positive holes are the mobile charge carriers and the immobile negatively charged states of the acceptor dopants form the excess space charge within the depletion layer.

The physics underlying photocatalysis shows that the energy level of the bottom of the conduction band in a semiconductor like TiO_2 is a measure of the reduction potential of photogenerated electrons, whereas the upper level of the valence band is a measure of the oxidation potential of photogenerated holes. The flatband potential, which is the potential to be applied to the semiconductor to reduce the band bending at the liquid-semiconductor interface to zero (see Figure 2.4), is a very useful quantity in photoelectrocatalysis as it helps the location of the energy of the valence and conduction band edges of a given semiconductor material. It is obtained by measuring the capacity of the semiconductor–electrolyte junction. Flatband potentials have been determined for a large number of materials and some representative examples, reported in form of band edge position, are shown in Figure 2.5. Apart from the type of semiconductor they depend on the nature and composition of the electrolyte. In aqueous solution the flat band potentials of most oxide semiconductors shifts by 0.059 V when the pH is changed by one unit.[37]

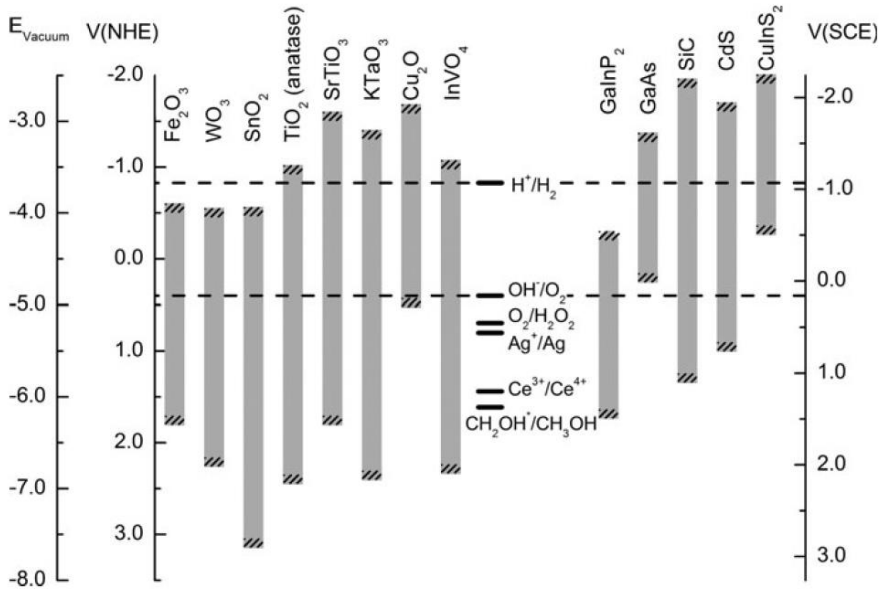

Figure 2.5: Band edge positions for selected semiconductors at pH 14, together with some important redox potentials.[12]

2.4 The photoelectrochemical cell under operating conditions

Figure 2.6 shows the energy diagram of a PEC cell in the dark and under illumination. In this example, the H_2O/O_2 redox couple is assumed to be the most active species and therefore dominates the electrochemical potential of the solution in the dark. The Fermi levels of the semiconductor and metal, which are electrically connected, adjust to a value close to E_{ox} (see Eq. 2).

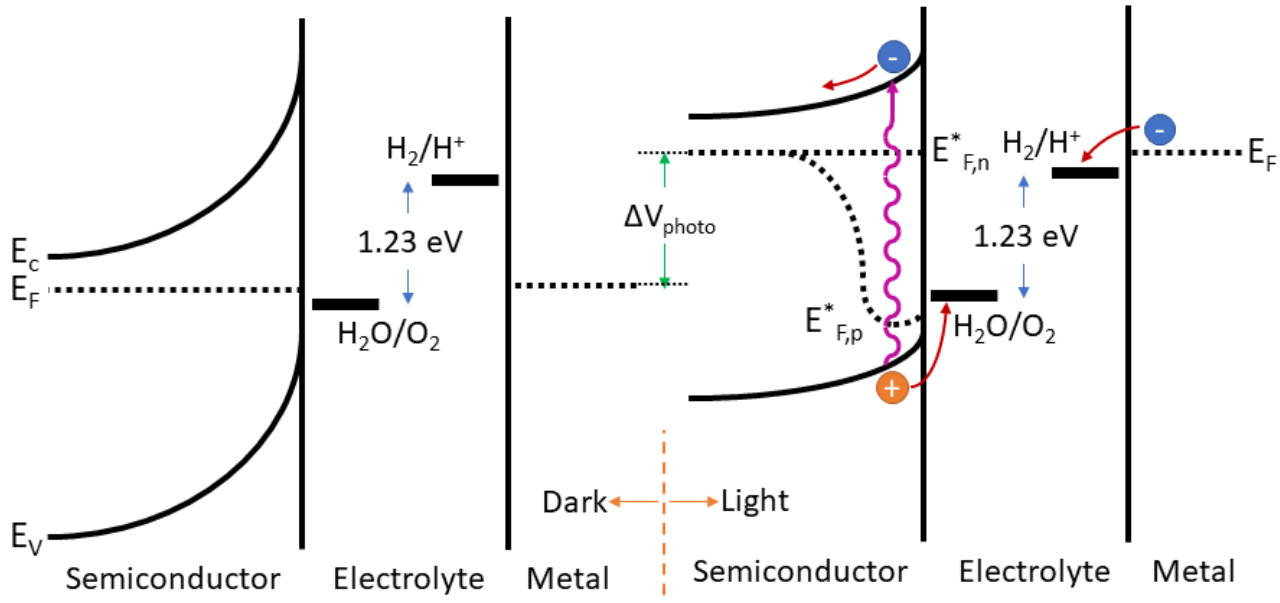

Figure 2.6: Band diagram for a PEC cell based on an n-type semiconducting photoanode that is electrically connected to a metal counter electrode; in equilibrium in the dark (left) and under illumination (right). Illumination raises the Fermi level and decreases the band bending. Near the semiconductor/electrolyte interface, the Fermi level splits into quasi-Fermi levels for the electrons and holes.

Upon illumination electron-hole pairs are created, and the Fermi level increases by ΔV_{photo}, the internal photovoltage. Since the system is no longer in equilibrium, particularly in the space charge region in which the electrons and holes are generated, the use of a single Fermi level is no longer appropriate. Instead, the concept of quasi-Fermi levels ($E^*_{F,n}$ *e* $E^*_{F,p}$) is more appropriate. In fact, they describe the population of electrons separately in the conduction band and valence band, when there is a perturbation that displace the system from equilibrium. Consider n_0 and p_0 the

concentration at the equilibrium of electrons and holes, respectively, and Δn and Δp the relative variation of the concentration induced by the illumination. In an n-type semiconductor, where $n_0 > p_0$ (such as TiO_2), the new concentration n and p will be:

$$n = n_0 + \Delta n \approx n \tag{3}$$

$$p = p_0 + \Delta p \approx \Delta p \tag{4}$$

so that $E_{F,n}^*$ remains horizontal whereas $E_{F,p}^*$is displaced from the value of the Fermi level in the bulk (remember that the perturbation is local). This means that the concentration of holes increases a lot in the illuminated region (which usually is close to the semiconductor/electrolyte interface) and from here they can be injected in the electrolyte to oxidize water. One particular aspect to note, is that the definition of quasi-Fermi level considers electrons and holes in the conduction and valence bands. They do not account for any changes in the occupation of surface or bulk defect states, which limits their predictive value for reactions in which these states are involved.[38]

2.5 Interfacial charge transfer

Charge transfer from the semiconductor to the electrolyte and vice versa depends on the available unoccupied states in the final medium. This means that, for example, electron transfer from the semiconductor to the electrolyte is possible only if the energy of the electron in the solid exceeds the reduction energy of the species in the solution. Controlling the potential applied to the working electrode is equivalent to controlling the energy of electrons within the working electrode. For example, by driving the electrode to more negative potentials (i.e., by connecting the negative side of the power supply to the working electrode), the energy of the electrons is raised, and they can reach high enough energy levels to transfer into empty electronic states of species in the electrolyte.

In this case, an electron current from the electrode to the solution occurs and it is called *reduction current*. On the contrary, by applying a more positive potential, the energy of the electrons can be lowered and electrons from the species in the solution go in more favourable energy states in the electrode (*oxidation current*) (see Figure 2.7).

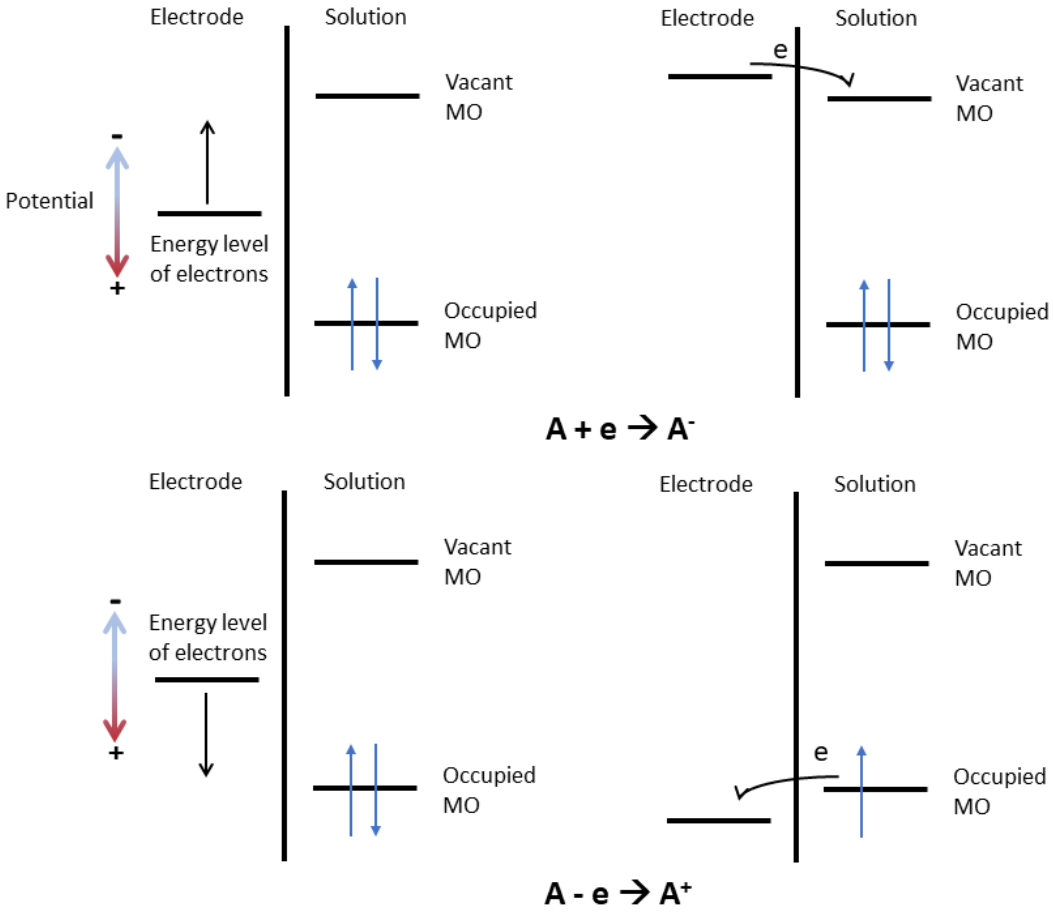

Figure 2.7: Representation of (a) reduction and (b) oxidation process of a species A in solution. The molecular orbitals (MO) of species A shown are the highest occupied MO and the lowest vacant MO. These correspond in an approximate way to the E_{ox} and E_{red} of the A/A^- and A^+/A couples, respectively.

These concepts are valid in general, no matter how the energy is supplied to electrons, whether by an external voltage supply or by illumination. In fact, when the PEC cell is illuminated,

a certain amount of energy is transferred from photons to electrons ($e\Delta V_{photo}$), raising the Fermi level of the system (see paragraph 2.4).

A deeper insight into the electron transfer theory[39], shows that the distribution of energy levels in the electrolyte is actually more complex and it is determined basically by the thermal fluctuation of oriented solvent molecules around ions. As a consequence, the energy level of the central ion fluctuates itself (as seen from the electrode), and assuming this motion to be harmonic, the distribution of the redox states turns out to be gaussian, as reported in Figure 2.8.

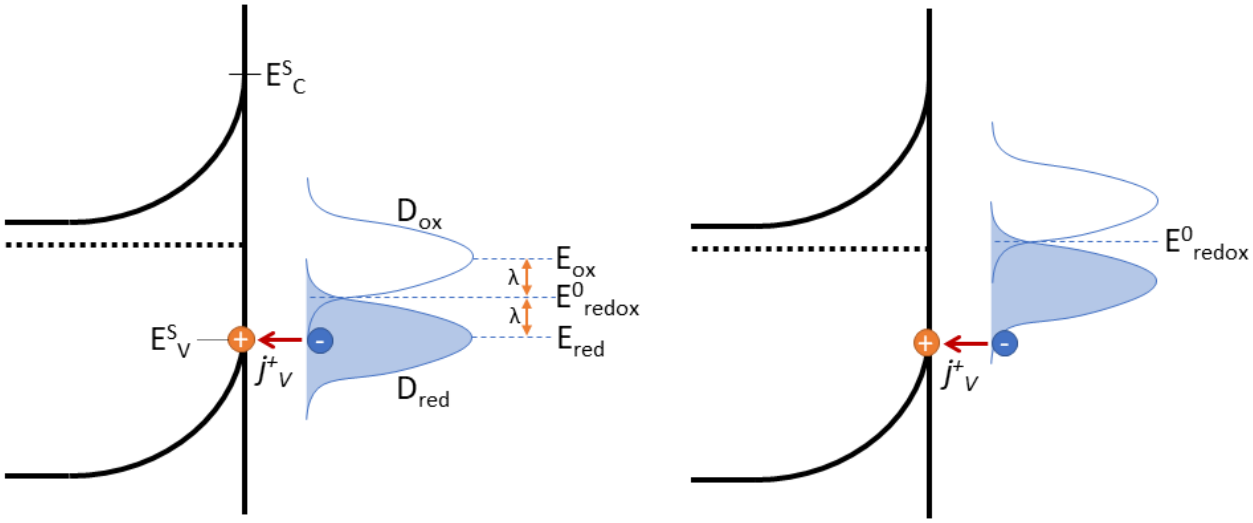

Figure 2.8: Model of the energy levels involved in electron transfer from a redox species in the electrolyte to a photogenerated hole in the semiconductor valence band. A large overlap of the distribution of reduced energy levels in the electrolyte with the energy of the hole (left) gives higher currents than a small overlap (right).

The reduction or oxidation process involves a reorganization of the solvent molecules around the ion in order to accommodate the different charge on it. The electrostatic energy required for this operation is called *reorganization energy* and it is indicated by λ in Figure 2.8. In fact, in semiconductors, charge transfer occurs either at the bottom of the conduction band or at the top of the valence band and, in some cases, even from surface states. In Figure 2.8 the case of

photogenerated holes is reported, allowing the transfer of electrons from electrolyte to the semiconductor. It is important to notice that the probability of electron transfer decreases if E_{red} is too far above E_V^S. The actual charge transfer process takes place via tunneling, and since it is an iso-energetic process, it requires the fluctuating energy levels of ions in the electrolyte to be, at a certain moment, equal to the energy of the electron or hole in the semiconductor. The transfer rate is then proportional to three factors, which are: the concentration of carriers in the semiconductor, the density of available energy levels in the electrolytes and a quantum-mechanical tunneling coefficient.[12,40]

3 SAMPLE PREPARATION

Many synthesis techniques are available for fabricating semiconductor materials for photoelectrodes, each having advantages and limitations that should be kept in mind when choosing a preparation method.[13] In this chapter I am going to examine two physical deposition techniques that I used for preparing nanostructured TiO_2 photoanodes: GPC for the synthesis of NPs-based photoelectrodes and RF Magnetron Sputtering for the deposition of thin film. They are considered physical methods since during the deposition process no chemical reactions in the gas phase and at the substrate surface take place. The main difference between GPC and sputtering is the following: in GPC technique atoms are removed from the source material by thermal means, whereas in sputtering they are dislodged from solid target (source) surface through the impact of gaseous ions.

Concerning the sputtering apparatus, I designed, implemented and tested the entire system, from the hardware part to the software control system developed with LabVIEW.

3.1 Gas phase condensation

Gas Phase Condensation is a bottom-up physical vapor deposition technique for the production of NPs. The process takes place in a high vacuum chamber, filled with an inert gas (typically Helium or Argon). The precursor material is heated in order to produce vapor which is then cooled by collisions with the inert gas until it becomes supersaturated. In this condition, the nucleation of NPs is thermodynamically favored and solid clusters start forming. This process can be described by the classical theory of homogeneous nucleation, in which the energy of a solid cluster of N atoms, ΔG_N, is assumed to be separable into bulk free energy and interface free energy:

$$\Delta G_N = \Delta G_N^{bulk} + \Delta G_N^{interface} = N\left(\mu_{solid} - \mu_{vapour}\right) + \eta N^{2/3}\gamma \quad (5)$$

where μ is the chemical potential, η a shape factor and γ the interfacial energy per unit area. Here it is assumed the cluster to be isotropic, therefore it will form a spherical shape to minimize its surface. As the precursor vapour is supersaturated, it is unstable towards its condensation, meaning that $\mu_{solid} < \mu_{vapour}$ and therefore $\Delta G_N^{bulk} < 0$. The overall free energy features a maximum at the so called critical cluster size N_C, as reported in Figure 3.1, indicating growing instability of the smaller pre-critical cluster.

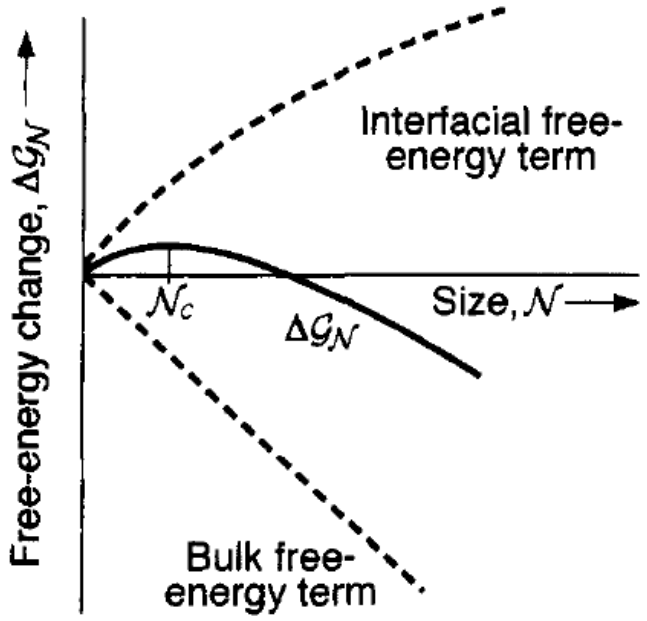

Figure 3.1: The continuous line reports the cluster free energy vs. cluster size for the nonequilibrium system during nucleation. The dashed lines show the two terms that contribute to the total free energy, the bulk and the interface term.[41]

After passing the critical cluster size, the free energy decreases and the cluster formation is thermodynamically favored. The cluster evolution proceeds with the gradual addition and loss of atoms from the vapor phase and via collision of already formed clusters.

3.1.1 Gas phase condensation setup

In Figure 3.2 a 3D sketch of the GPC experimental setup is shown. The system is composed by a main stainless-steel *Thermionics* ultra-high vacuum chamber provided with a pumping system constituted by a *Varian* turbomolecular pump and an *Edwards* rotary pump. The vacuum level is monitored by a *Varian ConvecTorr p-type Pirani* gauge and a *Varian* inverted magnetron gauge pressure sensor.

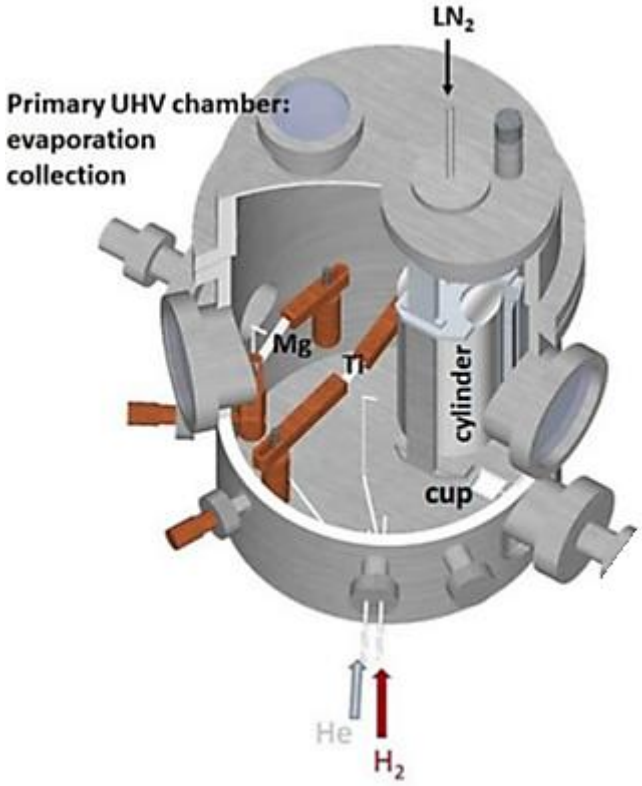

Figure 3.2: 3D sketch of the experimental apparatus for NPs synthesis.

Inside the chamber two pairs of copper electrodes can be used at the same time, each one holding a Joule heated tungsten boat for the thermal evaporation of the metallic precursor. Electrodes are connected to a high current *Thermionics* alternate current generator which can provide a current up to 500 A. For vanadium modified-TiO_2 NPs only one crucible was used since the precursor

material is a metallic powder of titanium mixed with vanadium, the ratio between them defining the relative concentration in the NPs. The evaporation rate of the metallic precursor is monitored by an *Edwards Film Thickness Monitor FTM7* quartz microbalance and can be adjusted by tuning the current flowing through the electrodes. During the growth stage, He is fed into the chamber at a constant flow rate, controlled by a *Bronkhorst* mass flow controller. A second mass flow controller is used to add oxygen during the evaporation, in order to oxidize the NPs. The pressure is dynamically kept constant by means of the rotatory pump. NPs are then collected on a rotating cylinder cooled by liquid nitrogen and, at the end of the process, scraped off the cylinder surface with a blade and stored in a glass vial.

3.2 Sputtering for thin film deposition

Sputtering is one of the most common physical vapor deposition processes for thin film preparation, thanks to its cost-effectiveness and reliability. In this process the precursor material, a solid disc target, is bombarded by energetic ions generated in a glow discharged plasma, situated in front of the target. The bombardment process causes the removal of target atoms, which may then condense on a substrate as a thin film.[42]

3.2.1 DC sputtering

The simplest sputtering system is DC sputtering. It takes place in a high vacuum chamber equipped with two planar electrodes: the cathode, on the top of which the target material to be deposited is placed, and the anode, to which the substrate is attached. The sputtering chamber is filled with sputtering gas, typically argon, at a pressure of 10^{-3}-10^{-2} mbar, which serves as the medium in which the discharge is initiated and sustained. The glow discharge process proceeds in several steps: at first, by applying an initial DC voltage (tens of V) to the electrodes, only a very small

current flows in the system because of the small number of the initial free charge carriers in the gas phase. As the voltage is increased, sufficient energy is transferred to ions to create more carriers through ion collisions with the cathode, which releases secondary electrons, and by impact ionization of neutral gas atoms. Thanks to this charge multiplication the current increases rapidly and large numbers of electrons and ions are created through an avalanche effect until the process becomes self-sustaining. At this moment the gas begins to glow and the ion bombardment spreads homogenously over the entire surface of the cathode.[43] In Figure 3.3 the typical plasma glow of argon gas during the sputtering deposition (picture taken from the sputtering system located in the Department of Physics and Astronomy at the University of Bologna).

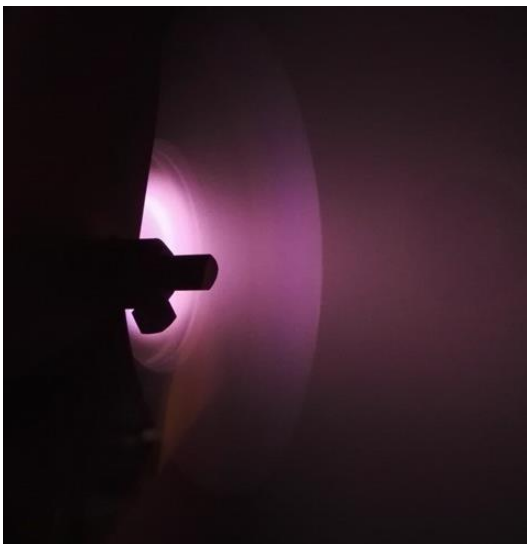

Figure 3.3: Plasma glow of argon gas during the sputtering deposition.

In Figure 3.4 a schematic representation of DC sputtering system is reported.

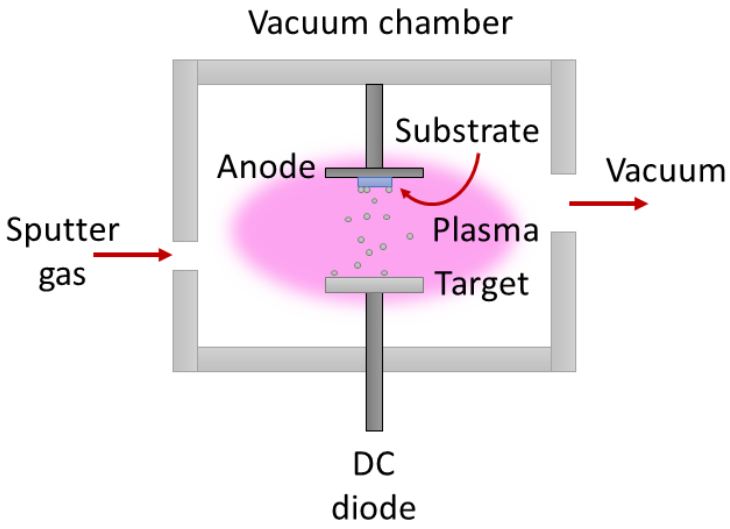

Figure 3.4:DC sputtering system.[44]

It is worthwhile to recall two important parameters of the sputtering process: the sputter yield and the deposition rate. The sputter yield is defined as the number of atoms or molecules ejected from a target surface per incident ion and can be considered a measure of the efficiency of the sputtering process. This quantity is a function of several parameters such as mass, density and binding energy of target atoms, the pressure of the inert gas, the incident angle and the mass of the ions and the entire cross section of the system.[45]

On the other hand, the deposition rate depends on the pressure inside the vacuum chamber ad the current. In fact, if the pressure is low the electron mean-free path between collisions is large and electrons collected by the anode are replaced by ion-impact-induced cathode secondary emission. Therefore, ionization efficiencies are low. By increasing the pressure, the electron mean-free path decreases and more ions are generated. But if the pressure is too high, the sputter atoms undergo increased collisional scattering and are not efficiently deposited. The optimal operating conditions are shown in Figure 3.5.

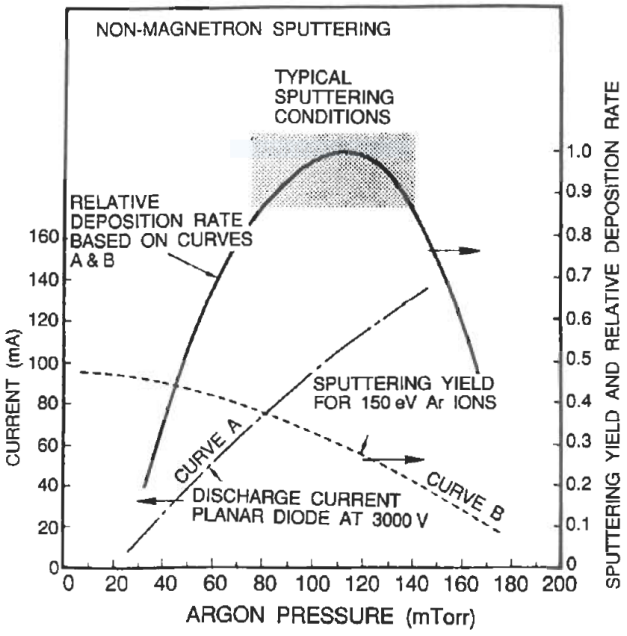

Figure 3.5: Influence of working pressure and current on deposition rate for nonmagnetron sputtering.[43]

3.2.2 Radio frequency sputtering

By substituting the metallic target with an electrically insulating material, i.e. metal oxides, the sputtering discharge cannot be sustained because of the immediate buildup of a surface charge of positive ions on the front side of the insulator, resulting in no current flow through the insulator. To sustain the glow discharge with the insulator target, RF (kHz to MHz) voltage is supplied to the target. RF sputtering essentially works because the target self-biases to a negative potential and once this happens, it behaves like a DC target where positive ion bombardment eject away atoms from the target. The negative self-bias is a consequence of the fact that electrons are considerably more mobile than ions and the latter have little difficulty in following the periodic change in the electric field. As the RF signal is applied to the target, a large initial electron current is drawn during the positive half of the cycle. However, only a small ion current flows during the second half of the cycle. This system enables a net current averaged over a complete cycle to be different

from zero even though there is no charge transport through the target. Therefore, the target bias shifts to a negative potential.[43]

3.2.3 Radio frequency magnetron sputtering

Since sputtering deposition is generally limited by low deposition rates and low ionization efficiencies in the plasma, these limitation have been overcome by the development of magnetron sputtering.[42] A strategy to increase the deposition rate is to lower the sputtering pressure with the addition of magnets under the target. In the magnetron sputtering system, a magnetic field is superposed on the cathode which is parallel to the cathode surface. The electrons in the glow discharge exhibit spiralling motion and the center of the orbit drifts in the direction given by $\boldsymbol{E} \times \boldsymbol{B}$ with the drift velocity of $|\boldsymbol{E}|/|\boldsymbol{B}|$, where $\boldsymbol{E}$ and $\boldsymbol{B}$ denote the electric field in the discharge and the superposed transverse magnetic field, respectively. The magnetic field is oriented such that these drift paths for electrons form a closed loop (Figure 3.6).

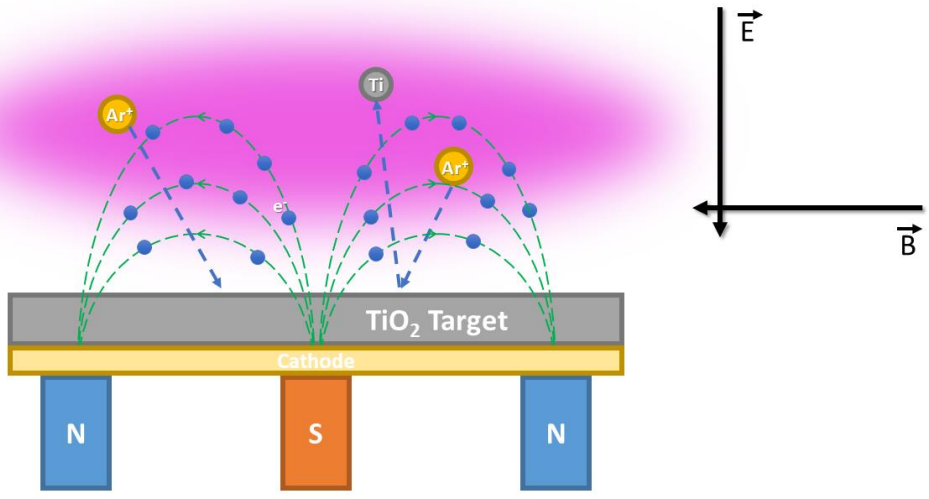

Figure 3.6: Trajectories of electrons near the target cathode of a RF magnetron sputtering system.

This electron trapping effect increases the collision rate between the electrons and the sputtering gas molecules. This enables one to lower the sputtering gas pressure typically to 10^{-2}-10^{-3} mbar. In the magnetron sputtering system, the magnetic field increases the plasma density, which leads to increases of the current density at the cathode target, effectively increasing the sputtering rate at the target. Due to the low working gas pressure, the sputtered particles traverse the discharge space without collisions, which results in high deposition rates.[44]

3.2.4 Radio frequency magnetron sputtering setup

In Figure 3.7 a 3D sketch of the RF magnetron sputtering system is reported. On the right, a photo of the sputtering system (located at the Department of Physics and Astronomy in Bologna) that I used for preparing the sample is also reported. In Figure 3.8 the inner section of the vacuum chamber is shown. The system is composed by a cylindrical ultra-high vacuum chamber at the bottom of which an *Edward EXT 250* turbomolecular pump together with an *Agilent IDP-10* scroll pump is connected. This pumping setup allows to reach 10^{-7} mbar after one day. Pressure is monitored by two different sensors: a *Pfeiffer Compact Full Range Gauge PKR 251* is used during the evacuation and venting procedure, exploiting its wide working pressure range, from 1000 to 10^{-9} mbar, while a more accurate *MKS absolute Baratron* is used during the sputtering evaporation (working range 10^{-1}-10^{-4} mbar). Argon gas is introduced using an *MKS GE50A* flowmeter. Pressure and gas flow are monitored and controlled by means of a control code written in *LabVIEW* . The pure (99.9 %) TiO_2 target, a 2” disc and 0.125” thick, is attached to the *KENOS-2* cathode, equipped with a manual shutter. Substates are attached to the sample holder in front of the target.

The sputtering procedure is the following: first of all, the chamber is evacuated to 10^{-7} mbar and then is backfilled with argon up to 3-5 10^{-2} mbar in order to ignite the glow discharge.

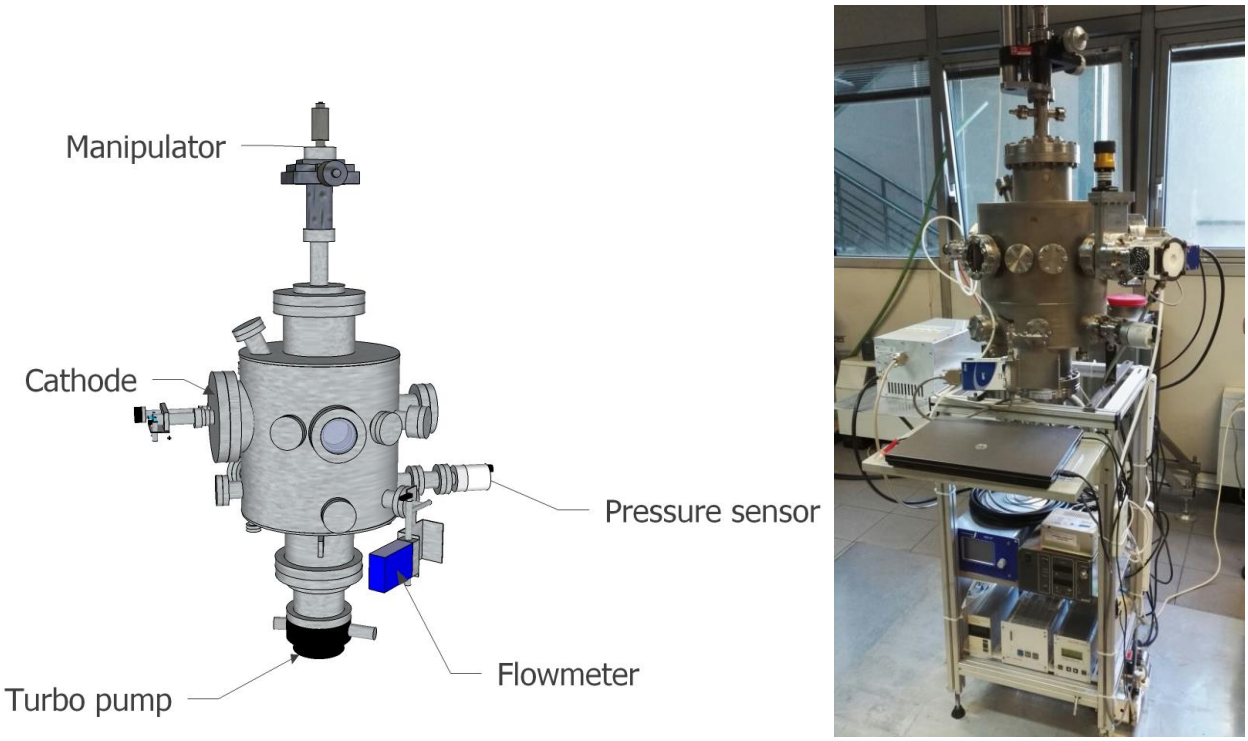

Figure 3.7:3D sketch of the sputtering setup (left) and the instrument used for the preparation of samples (located at Department of Physics and Astronomy in Bologna)(right).

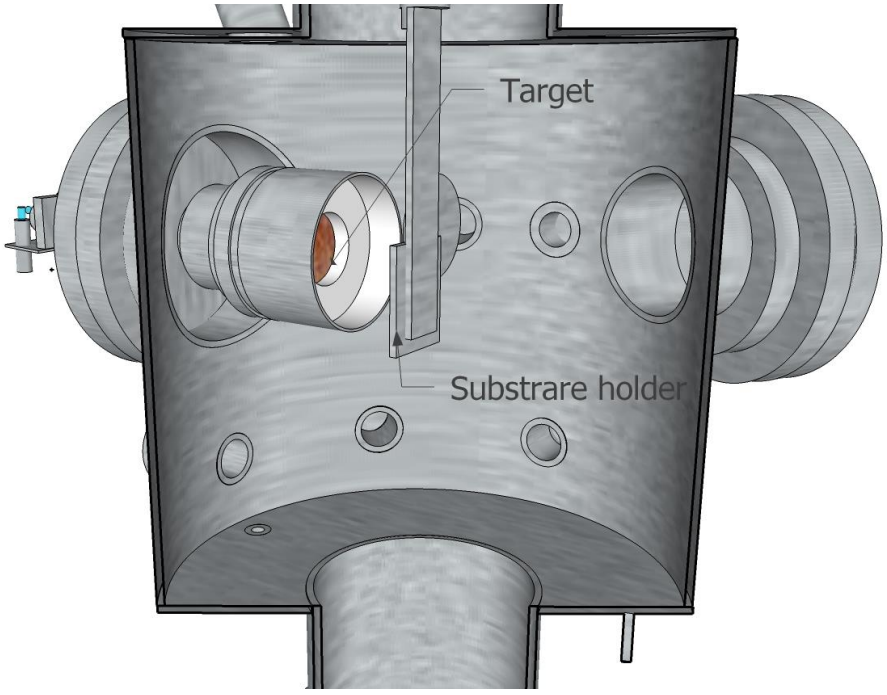

Figure 3.8: Section of the inner part of the vacuum chamber.

Then the pressure is stabilized and dynamically maintained at 8 10^{-3} mbar using the flowmeter and the pumps. The power supplied to the cathode is kept constant at 75 W throughout the evaporation process. In this condition, the deposition rate is ~ 1.73 nm/min (Figure 3.9). The entire system is controlled by a LabVIEW software that I specifically realized.

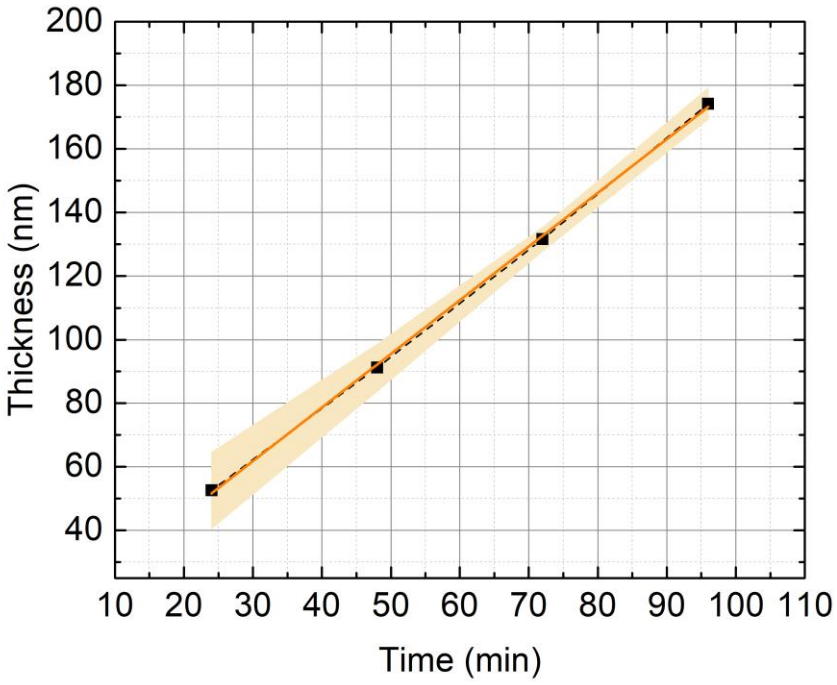

Figure 3.9: Thickness as a function of the deposition time is reported. By performing a linear fit and taking the slope, the deposition rate is calculated (1.7 nm/min).

In order to dope TiO_2 films, small rectangular vanadium pieces are attached with carbon tape on the edge of the TiO_2 target as shown in Figure 3.10 .

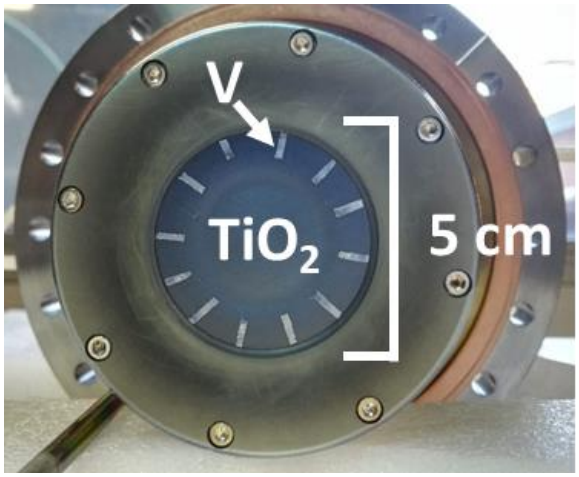

Figure 3.10: TiO_2 target with vanadium pieces.

Finally, it is possible to use a gas mixture of argon and nitrogen, in order to dope TiO_2 with N, using a gas mixer at the gas inlet (see Figure 3.11).

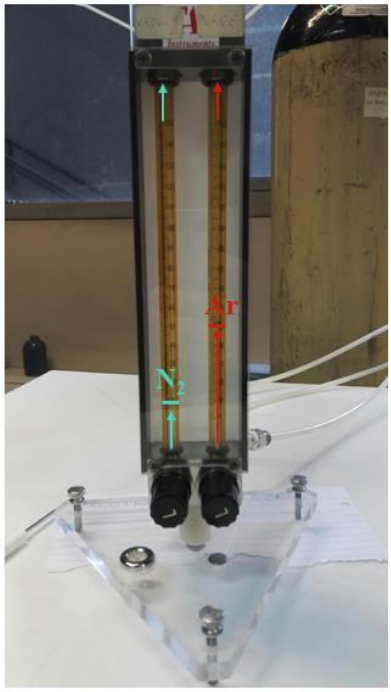

Figure 3.11: Gas mixer used for introducing nitrogen and argon in the sputtering chamber.

4 EXPERIMENTAL APPARATA

In this chapter, I will describe the main experimental techniques and related setups used to perform measurements on TiO_2 based samples. During my PhD course, I used several instruments and experimental techniques in order to gain a wide overview of all the characteristic features of the sample under investigation, such as morphology, crystal and electronic structure, chemical composition, optical properties and photoelectrochemical performances. For the structural and morphological characterization, I collected data from X-ray photoelectron spectroscopy, X-ray diffraction and Raman spectroscopy, meanwhile X-ray absorption near edge spectroscopy was used to determine the electronic structure. Then, optical methods such as transient absorption spectroscopy and photoelectrochemical characterization with photoelectrochemical set up were adopted for study the charge transport. Here I report the main techniques that have been most relevant for my PhD research and activity.

In this context, I made a very significant contribution to the development of the photoelectrochemical setup, from the hardware to the software part; it is still under development in order to improve sample flexibility and automatization of experimental procedures and analysis.

4.1 Photoelectrochemical measurements

Photoelectrochemical characterization includes a wide variety of experimental techniques, such as the measurement of Incident Photon to current Conversion Efficiency spectra, Cyclovoltammetry and Electrochemical Impedance Spectroscopy. The aim of this set of experimental methods is to evaluate the performance of the material as well as its critical limitations. In this regard, the real challenge is the interpretation of data coming from such different techniques and the following

translation into the desired material parameters. Below, the description of the single instruments that are part of the photoelectrochemical setup is reported.

The experimental setup is composed by three main instruments: a PEC cell, a potentiostat and a light source. Additional instruments are: a monochromator, a lock-in amplifier, an analog to digital converter (ADC) and a pyroelectric sensor. The entire system is controlled via a LabVIEW software. A scheme of the setup in shown in Figure 4.1.

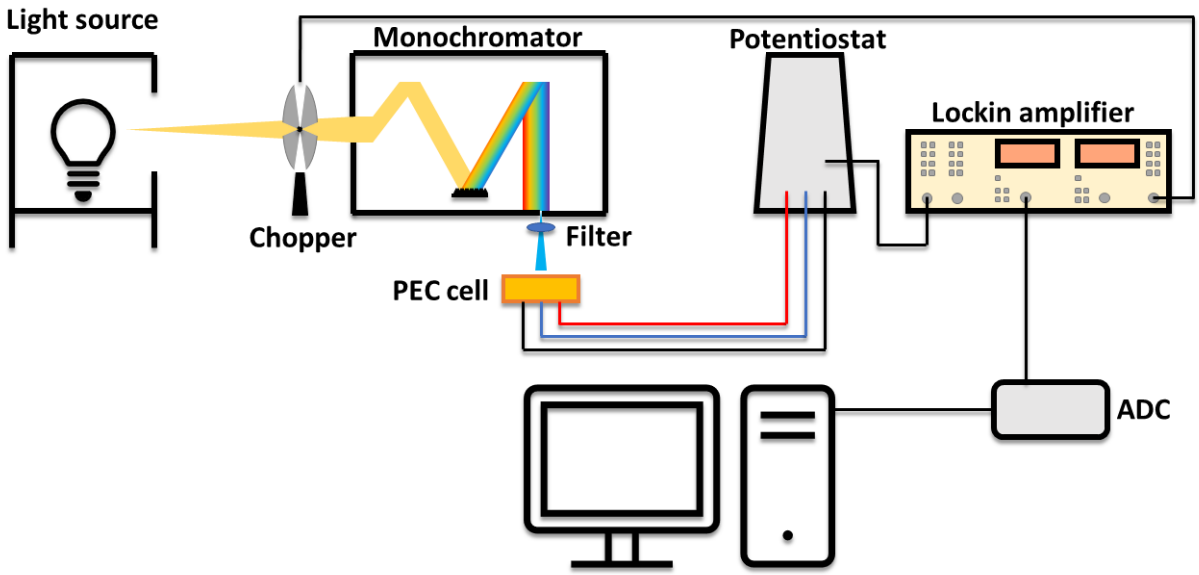

Figure 4.1: Simplified scheme of the setup for photoelectrochemical measurements.

4.1.1 The photoelectrochemical cell

The key component of the experimental setup is the PEC cell, in which the photoanode is installed and tested. In particular, the cell that I used for these measurements was designed and made inhouse. It is made by PEEK, a colourless organic thermoplastic polymer with an excellent chemical resistance. It is constituted by a reservoir to be filled with the electrolyte, in which three

electrodes are immersed: the working electrode (WE), made by the sample under investigation, the counter electrode (CE) to supply current and the reference electrode (Ref), with respect to which the potential applied to the cell is measured. The 3D sketch of the cell is reported in Figure 4.2. The light from the source passes through the quartz window and the electrolyte before hitting the sample.

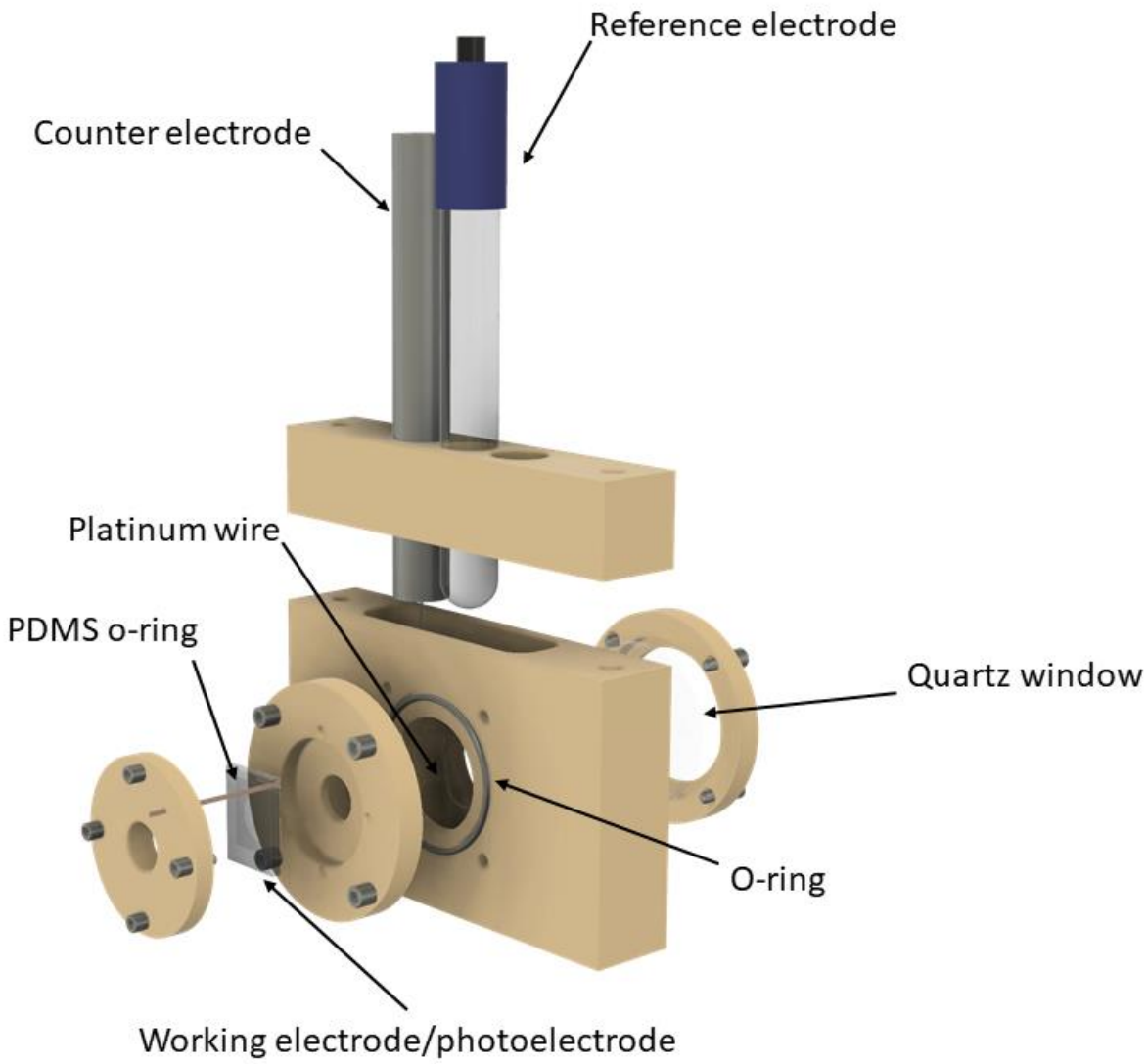

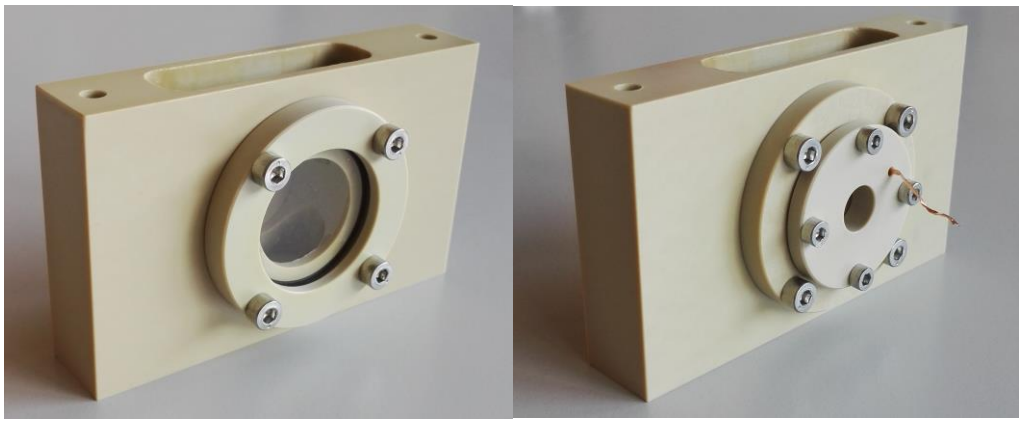

Figure 4.2: 3D sketch and pictures of the photoelectrochemical cell used for photoelectrochemical measurements.

It is important to notice that thanks to this design the wetted area of the photoanode surface is the same as the illuminated one. A PDMS O-ring pressed against the photoanodes and two rubber O-rings are used to seal the cell. The photoanode, whose substrate is composed by Fluorine Tin Oxide (a transparent conductor) coated glass, is electrically connected through an alligator clip to the external circuit using a piece of copper tape. The counter electrode is a platinum wire, held by a metal rod connected to the external circuit with a banana plug. Finally, the reference electrode is based on the Hg/HgO redox reaction whose reference potential has to be shifted by -0.076 V with respect to the commonly used SCE (Saturated Calomel Electrode). The electrolyte is a 0.1M KOH solution (pH 13).

4.1.2 The potentiostat

The potentiostat is really the most important piece of hardware of the photoelectrochemical setup. Its role is to measure the potential difference between the working (WE) and the reference (Ref) electrode and keep it equal to the desired potential difference by adjusting the potential at the counter electrode (CE). The potential reported by the potentiostat and used to plot every measured data is the potential difference between the reference and the working electrode. On the contrary,

the real potential of the counter electrode is unknown and it serves only to supply the voltage and the current necessary to keep the desired potential difference between the reference and the working electrode. We used an *Autolab PGSTAT204* potentiostat equipped with a *FRA32M* electrochemical impedance spectroscopy module to perform all the photoelectrochemical measurements, in combination with NOVA software, provided together with the potentiostat.

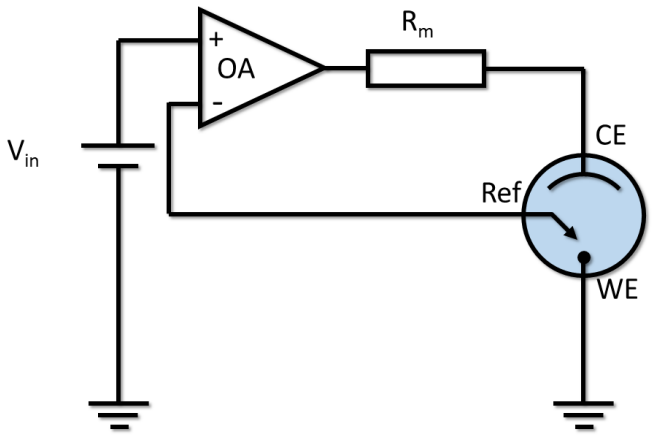

Figure 4.3: Simplified internal circuit of a potentiostat. The main component is the control amplifier (an operational amplifier OA), that allows to keep the voltage between the reference and the working electrode as close as possible to the desired value.

4.1.3 Light source

In order to simulate solar illumination an arc xenon lamp is used, which provides the best match to the solar spectrum rather than halogen lamp or LEDs. To ease the comparison between the performance of different devices, measurements are usually performed under AM1.5G conditions. This stands for "air mass 1.5 global" and refers to the spectral distribution and intensity of sunlight on a 37° south facing tilted surface after it has travelled through 1.5 times the thickness of the earth's atmosphere. The total integrated intensity in this condition is 1000 W/m^2. Another common configuration consists in a xenon lamp coupled with a monochromator for wavelength-dependent

photocurrent measurements. This is the actual setup that I used for photoelectrochemical characterization. The incident spectrum on the sample is reported in Figure 4.4.

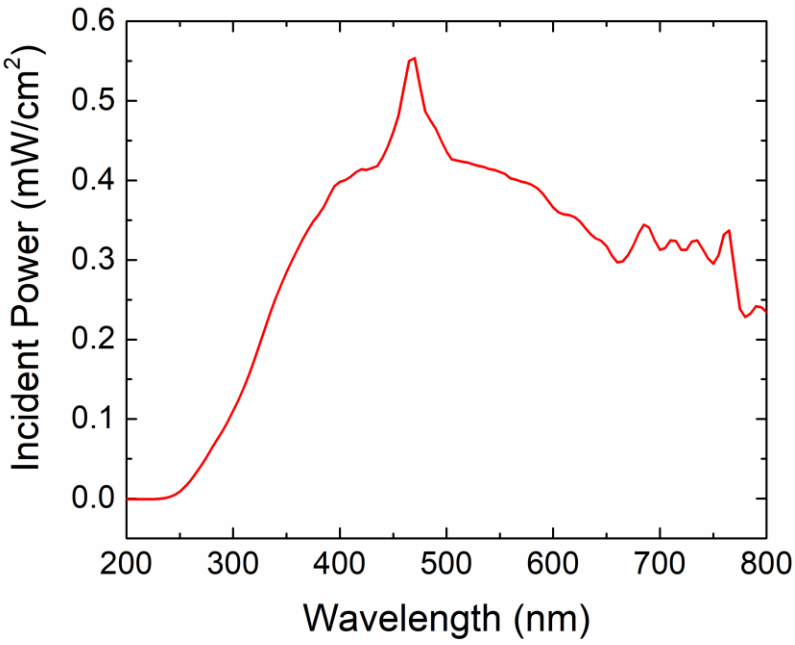

Figure 4.4: Spectral distribution of the Xenon lamp incident on the sample.

4.1.4 Additional components

To perform wavelength-dependent photocurrent measurements, a *Cornerstone 260 Oriel Instrument* monochromator is interposed between the light source and the PEC cell. It provides a monochromatized light beam with a band broadening of 5 nm (FWHM). A long pass filter is placed after the exit slit to remove higher order diffracted light from the grating inside the monochromator. Before the entrance of the monochromator a chopper is placed in order to provide an alternate signal to be amplified with the lock-in amplifier. It receives the chopped signal from the potentiostat and amplifies it. The output is fed into an ADC board connected to a computer by a USB cable, where the LabVIEW software is installed.

4.2 Photoelectrochemical measurements

4.2.1 Incident photon to current conversion efficiency spectra

The spectral response of photoelectrodes can be investigated by recording the photocurrent as a function of the incident wavelength at a constant applied potential. In order to normalize the photocurrent spectrum of the photoelectrode, the intensity of the light source is also recorded using a light intensity sensor (pyroelectric, as in this case). By dividing the photocurrent spectrum by the incident lamp spectrum, the incident photon to current conversion efficiency can be obtained, which can be interpreted as the ratio between the number of incident photons that are converted to electrons and the external outcoming current from the photoelectrode. It is given by:

$$IPCE(\lambda) = \frac{hc}{e}\left(\frac{j_{photo}(\lambda)}{\lambda P(\lambda)}\right) \tag{6}$$

in which j_{photo} is the measured current density and P is the incident photon power. IPCE values in excess of 80% for the photo-oxidation of water have been reported for, e.g., WO_3[46] and for TiO_2 under UV illumination.[47] The difference between the measured IPCE and its maximum value of 100% reflects two possible loss mechanisms: the first is optical, and it is due to the sum of incident photons that are reflected or transmitted, while the second is charge transport related, since it is due to photogenerated electron-hole pairs that recombine before reaching the external circuit. An example photocurrent and IPCE spectra for V-modified TiO_2 is reported in Figure 4.5.

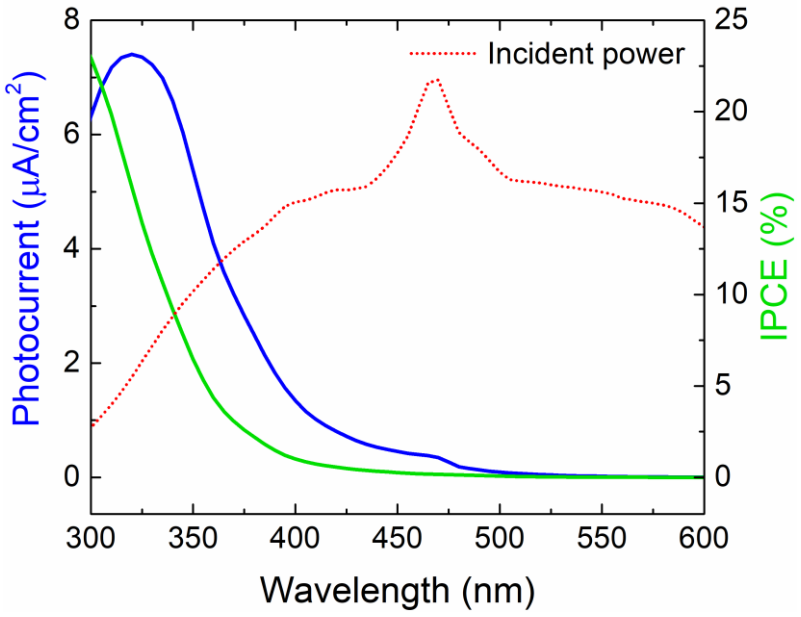

Figure 4.5: Photocurrent and IPCE spectra for V-modified TiO_2 thin film; IPCE was recorded applying 0.5 V bias. The incident spectrum of the light source is also reported in red.

4.2.1.1 Measurement of IPCE spectra with a lock-in amplifier and a potentiostat

The lock-in amplifier (Figure 4.1) used in the PEC setup is a *SR830 Stanford Research System*. It is used to amplify the voltage signal coming from the potentiostat before converting it with the ADC. It is particularly useful when photocurrent signals are low (typically, at the beginning of the optical absorption, in the visible range around 500 nm in the case of V-modified TiO_2 thin film samples), in order to extract it from the dark current noise. The input voltage signal V_{in} of the lock-in amplifier comes directly from the potentiostat and it is proportional to the photocurrent generated I_{phot} during the measurements, specifically:

$$V_{in} = \frac{I_{phot}}{R_{CR}} \tag{7}$$

in which R_{CR} is the current range of the potentiostat, which represents the actual amplification factor provided by the potentiostat. The lock-in amplifier calculates the root mean square V_{rms} of the input signal V_{in} (considering only the component at the reference frequency provided directly by the chopper, see Figure 4.1) and provides an output DC signal V_{out} in the range from 0 V to 10 V; this value is proportional to the root mean squared of the input signal V_{rms} through the following equation:

$$V_{out} = V_{rms} \frac{10\ G_{EXP}}{G_{SENS}} \tag{8}$$

in which G_{EXP} and G_{SENS} are the output and the input gain of the signal, respectively. The crucial part of the entire signal processing is the relation between V_{rms} and V_{in}. It is required to calculate the peak-to-peak value V_{pp} of the input signal, which represents the real value of the photocurrent. Depending on the shape of the input signal, which can be sinusoidal, triangular or squared, the value of peak-to-peak signal is $V_{pp} = 2\sqrt{2}\ V_{rms}$, $2\sqrt{3}\ V_{rms}$ or $2\ V_{rms}$, respectively. Among all the factors that contribute in shaping the input signal, chopper frequency and charge carrier dynamics processes of the sample after light exposure are the most relevant. When passing from dark to light and vice versa the photocurrent reaches its stable value within a typical transient time, depending on the charge dynamics of the sample. If the chopper frequency is close to this transient time, the shape of the signal will be triangular; on the contrary, if the transient time is shorter than the chopper frequency, meaning that charge transport inside the material is efficient and barely affected by recombination mechanisms, the shape of the signal will be squared.

4.2.2 Cyclic voltammetry

Cyclic voltammetry is a powerful technique used to study electron transfer-initiated chemical reactions,. The application of this technique to photoelectrocatalysis can provide important information about the sample under investigation.[48] It consists in performing a linear sweep of the potential applied to the working electrode while recording the current generated. It is usually performed by recording the current both under illumination and in the dark. By subtracting the dark current (current generated with no illumination) from the photocurrent it is possible to separate the contribution of the light to the system response. This is particularly useful when photocurrent values are not so intense and thus comparable with dark current. An example is reported in Figure 4.6 for pure a TiO_2 thin film deposited on a FTO coated glass. An important parameter which can be easily extracted from this data is the onset potential, which is the potential at which the photocurrent starts flowing (intersection of the two curves in Figure 4.6). However, the actual potential that needs to be applied before a photocurrent is observed is often several tenths of a volt more positive than the flat band potential. This effect can be due to recombination in the space charge layer, hole trapping at surface defects, or hole accumulation at the surface due to poor charge transfer kinetics.[49,50] This technique is also useful to choose the right potential at which the IPCE should be performed, in order to maximize the current generated by photons and reducing the contribution of the dark current at high voltage (electrolysis of water). For my samples I choose 0.5 V.

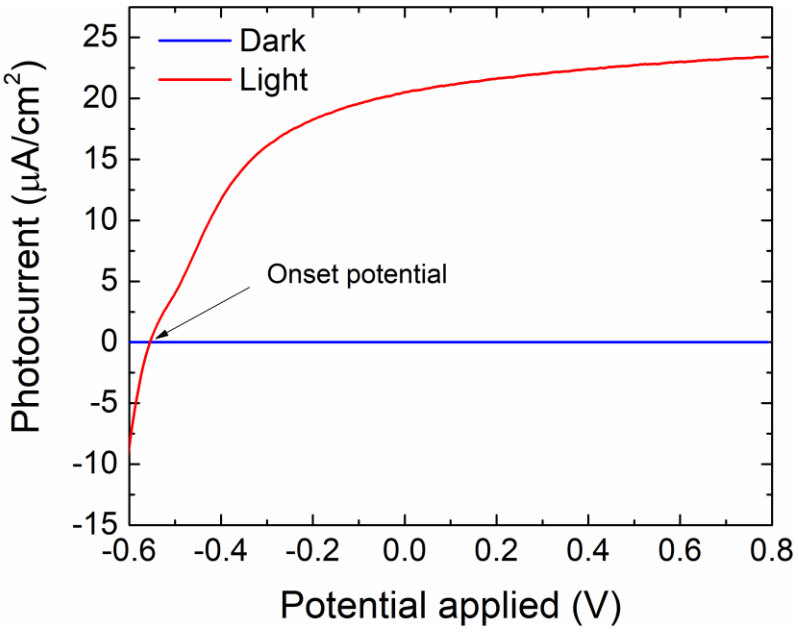

Figure 4.6: Cyclovoltammetry measurements for TiO_2 thin film deposited on FTO coated glass. The dark current is reported together with the photocurrent generated upon illumination with light at λ=300 nm. The onset potential is at the intersection of the two curves.

4.2.3 Electrochemical impedance spectroscopy

Electrochemical impedance spectroscopy is a technique which is used to measure the impedance of an electrochemical system. The fundamental approach of EIS is to apply a small amplitude sinusoidal excitation signal to the system under investigation and measure the response (current or voltage or another signal of interest). A low amplitude sinewave $\Delta E \sin(\omega t)$ of a fixed frequency ω is superimposed on the DC polarization voltage applied to the working electrode, resulting in a current response of a sine wave superimposed on the DC current $\Delta i \sin(\omega t + \phi)$. The current response is shifted in phase with respect to the applied potential. This approach relies on the low magnitude perturbation of the system, so that the first Taylor series expansion factor for the current given by $\frac{di}{dE}_{E_0,i_0} \Delta E$ can be considerrd a good approximation to the total current response,

neglecting higher order Taylor terms. Thus, the impedance of the system can be calculated using Ohm's law:

$$Z(\omega) = \frac{E(\omega)}{i(\omega)} \tag{9}$$

in which $Z(\omega)$ is the total impedance of the system and is a complex quantity with a magnitude and a phase which depends on the frequency of the signal. Therefore, by varying the frequency of the applied signal it is possible to obtain the impedance of the system as a function of the frequency. Typically, in electrochemistry a frequency range from 100 kHz to 0.1 Hz is used.

Data from EIS measurements are usually represented by using two different plots: the Nyquist plot, which consists in plotting the real part of impedance against the imaginary part, which provides a quick overview of the data for qualitative interpretation, but cannot represent the frequency dependency of the real and imaginary part, and the Bode plot, in which the absolute value of impedance and phase shift are plotted as a function of frequency in two separate plots. An example of these plots for a TiO_2 thin film deposited on FTO coated glass is reported in Figure 4.7 and will be discussed in paragraph 6.2.

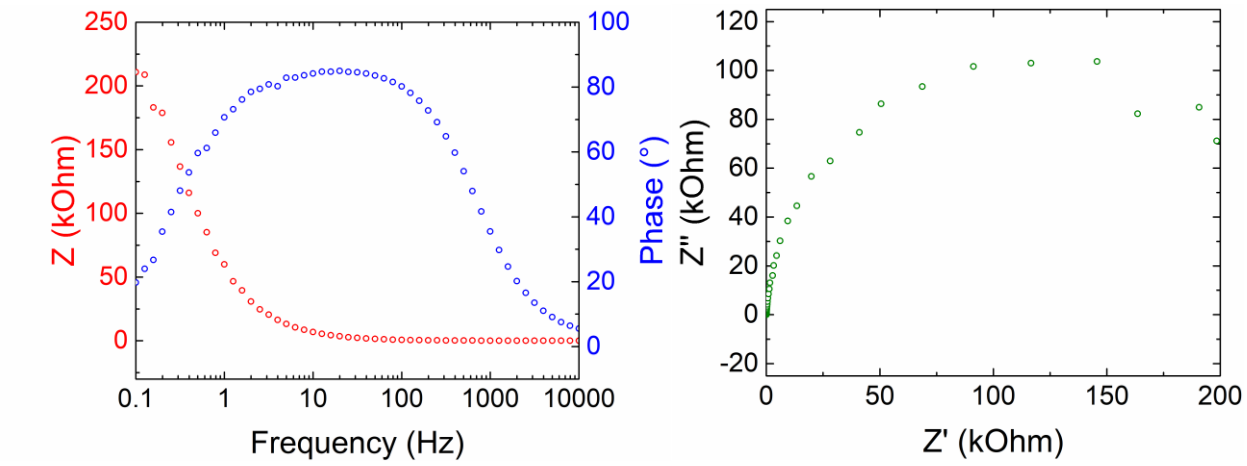

Figure 4.7: Bode (left) and Nyquist (right) plots for a TiO_2 thin film (130 nm) on FTO coated glass.

4.2.3.1 Equivalent circuit model

The characterization of electrochemical systems with impedance spectroscopy requires the interpretation of data with suitable equivalent circuit models. These models are built starting from passive element such as resistors, capacitors and inductors, but also distributed elements such as constant phase elements (CPE), with an impedance of $Z_{CPE} = \frac{1}{Y_0(j\omega)^n}$ (where $Y_0$is the admittance of an ideal capacitance and n ranges from 0 to 1) and Warburg impedance, expressed by $Z = \frac{1}{Y_0\sqrt{j\omega}}$, used when the surface of the photoelectrode is not homogeneous. The circuit is composed by combining these elements in series or in parallel and a certain physical meaning is then assigned to the various elements. The simplest circuit (see Figure 4.8) usually adopted to model photoelectrochemical system is an RC series circuit, where R_s represents the overall resistance that includes contacts, electrolyte and bulk and C_{sc} is the space charge region capacity. The overall impedance of this circuit is:

$$Z^* = R - j\frac{1}{\omega C_{sc}} \tag{10}$$

in which ω represents the angular frequency at which the impedance is measured. From this simple circuit it is easy to notice that the real part of the impedance corresponds to the resistance R and the imaginary part is $-1/\omega C_{cs}$, meaning that the space charge capacitance can be directly determined from the imaginary part of the impedance.

A slightly more complex circuit model (the so-called Randles model[51]) is reported in Figure 4.8, and it includes a capacitor R_{sc} in parallel with C_{sc}; it is often used also as starting point for more complex models. The parallel resistor takes into account the flow of charge following the chemical reactions that take place at the semiconductor/electrolyte interface.[52]

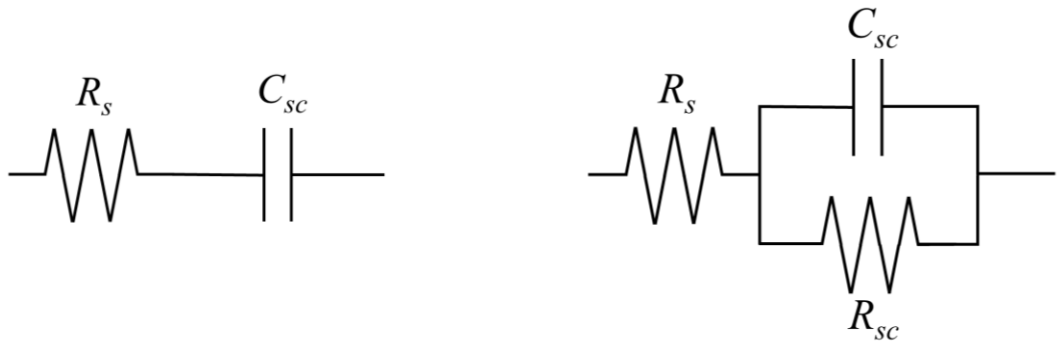

Figure 4.8: Basic RC equivalent circuit (left) and Randles equivalent circuit (right).

4.3 X-ray methods

As already stated in paragraph 2.1, the description of the atomic and electronic structure is fundamental for understanding the relation between transition metal oxide performance and their photoelectrocatalytic properties. In this regard, XAFS spectroscopy is a well-established technique used extensively for the characterization of semiconductors in solid or liquid, crystalline or

amorphous, bulk or nanoscale form.[53] The investigation of local properties such as oxidation state of the metal, metal-oxygen distance, structural distortions and degree of disorder can be performed with XAS, since it excites an electron from a core level (1s, 2p of the metal and 1s of the oxygen) to an unoccupied band (metal 2p, 3d and oxygen 2p), thus being element specific.[54]

XAFS is based on the measurement of energy-dependent fine structure of the X-ray absorption coefficient near the absorption edge of a selected element. In general, when an X-ray beam of intensity I_0 passes through a sample with a thickness t, its attenuation is given by Lambert-Beer's law:

$$I_t(t) = I_0 e^{-\mu(E)t} \tag{11}$$

in which I_t is the transmitted intensity and $\mu(E)$ is the energy-dependent X-ray absorption coefficient. For wide energy regions, it is a function of the incident photon energy, varying approximately as:

$$\mu(E) \sim \frac{dZ^4}{mE^3} \tag{12}$$

in which d is the density of the sample and Z and m are the atomic number and mass, respectively. Thus, $\mu(E)$ decreases with increasing photon energy. However, if the photon energy is equal to or exceeds the binding energy of a core electron a new absorption channel becomes available so that the photon is annihilated and creates a photoelectron and a core-hole. The consequence is a sharp increase in the absorption coefficient as shown in Figure 4.9. Above the absorption edge, the difference between the photon energy and the binding energy is converted into kinetic energy of the photoelectron and $\mu(E)$ continues to decrease on average with increasing photon energy. The

core-hole created is then filled in a short time of the order of 10^{-15} s by an electron from a higher energy state, releasing the corresponding energy difference via fluorescence X-ray or Auger emission.

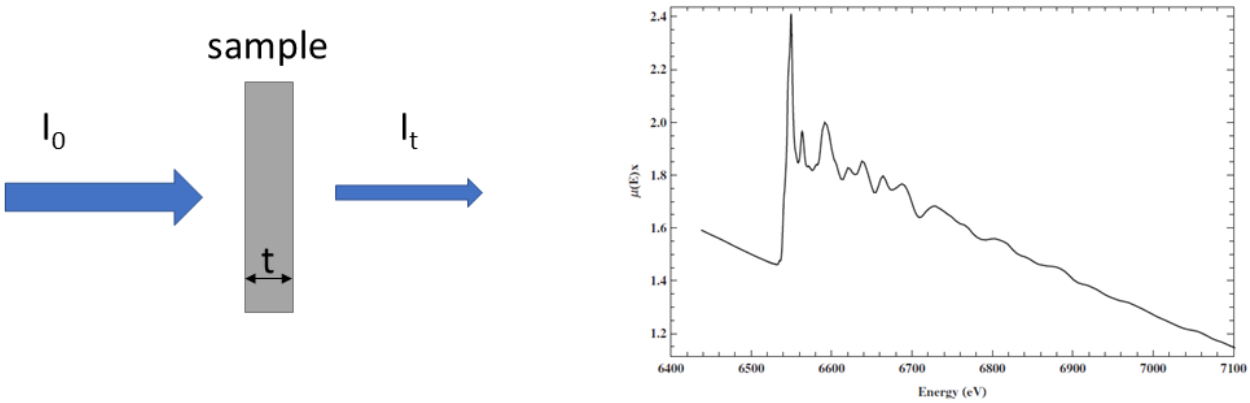

Figure 4.9: Schematic of incident and transmitted X-ray beam (a) and absorption coefficient μ(E) versus photon energy E around the MnO K-edge (b).

4.3.1 X-ray absorption fine structure

The term XAFS conventionally comprises EXAFS (Extended X ray Absorption Fine Structure) and XANES (X ray Absorption Near Edge Structure), according to the energy with respect to the absorption edge. The physics behind these techniques is fundamentally the same but different approximations and theoretical approaches are employed. XAFS is intrinsically a quantum mechanical phenomenon and it is based on the transition rate between a core level and final states, induced by a weak time-dependent perturbation such as an electromagnetic wave. Time-dependent perturbation theory states that, to first order, the transition rate is proportional to the product of the squared modulus of the matrix element M and the density of states $\rho(E_f)$, as expressed by the following equation:

$$\mu \propto |M|^2 \rho(E_f) \propto \left|\langle f|H_p|i\rangle\right|^2 \rho(E_f) \tag{13}$$

where $|i\rangle$ and $|f\rangle$ are the initial and finale states, respectively, and H_p represents the perturbation Hamiltonian that causes the transition, that is the electromagnetic field of the photon in this case.[55] Thus, the modulation of the absorption coefficient can be caused by both factors. When the energy of incident photons corresponds to the smallest binding energy of a core hole level of the atom, an electron is excited to an unoccupied bound state of the absorbing atoms. The consequence is a strong increase in the absorption coefficient at a particular X-ray energy, which corresponds to the difference between the core level and the unoccupied state. By increasing the energy of incident photons, the atom can absorb more energy so that the photoelectron can be excited to continuum state, generating a propagating wave that is scattered by neighbouring atoms, as illustrated in Figure 4.10.

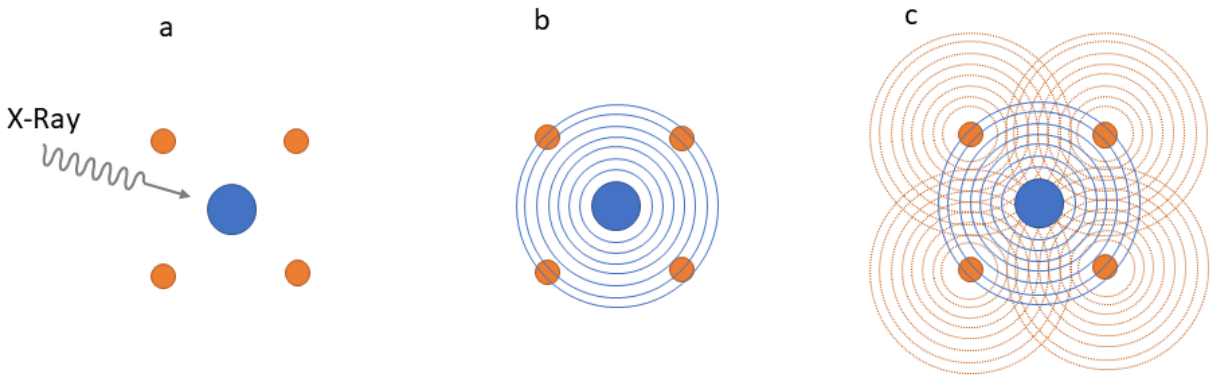

Figure 4.10:Phenomenological origin of XAFS. a) the X ray beam excites one of the core electrons of the blue atom. b) the excited photoelectron starts propagating as a wave until it reaches the atoms surrounding the absorber. c) The propagating electron wave is scattered creating an interference pattern that is extended also in the center of the absorber atom where core electrons are located. This interference process gives rise to modulations of the absorption coefficient.

This outgoing wave interacts with the backscattered wave from neighbouring atoms, causing interference effects based on the spatial geometry of the absorber environment and the wavelength

of the photoelectron, defined as $\lambda = \frac{2\pi}{k}$, where $k = \frac{p}{\hbar}$ is the photoelectron momentum. As a consequence, the final state is an energy superposition of outgoing and scattered waves. Since the initial state is highly localized on the absorbing atom, the matrix element M in equation (13) depends on the final state wave function at the site of the absorbing atom. Constructive and destructive interference of outgoing and scattered waves thus increases and decreases the absorption probability, generating an energy dependent fine structure of the absorption coefficient.[53,56]

4.3.1.1 X-ray absorption near edge spectroscopy

As the name suggests, XANES is based on the analysis of the XAS spectrum near the absorption edge (see Figure 4.11), which is due to the transition of the photoelectron to unoccupied bound and continuum states within ~ 50 eV of the absorption edge. This technique is sensitive to the chemical bonding, exhibiting for example characteristic features for different oxidation states of the absorbing atom. In data analysis, measured XANES spectra are typically compared to standard XANES spectra or simulated spectra of well known samples,[57,58] and using a linear combination fitting procedure the quantity with which they are present in the sample under investigation is calculated.

4.3.1.2 Extended X-ray absorption fine structure

When energy exceeds ~ 50 eV above the absorption edge, the photoelectron is promoted to a continuum state. Therefore, spectral features in this region do not depend on chemical bonding but on the atomic arrangements around the absorbing atom. EXAFS can measure the coordination number, interatomic distances and structural and thermal disorder around a particular atomic

species. Theoretical calculations of the fine structure in EXAFS range have improved enormously during the last two decades and simulations with sufficient accuracy are now available.

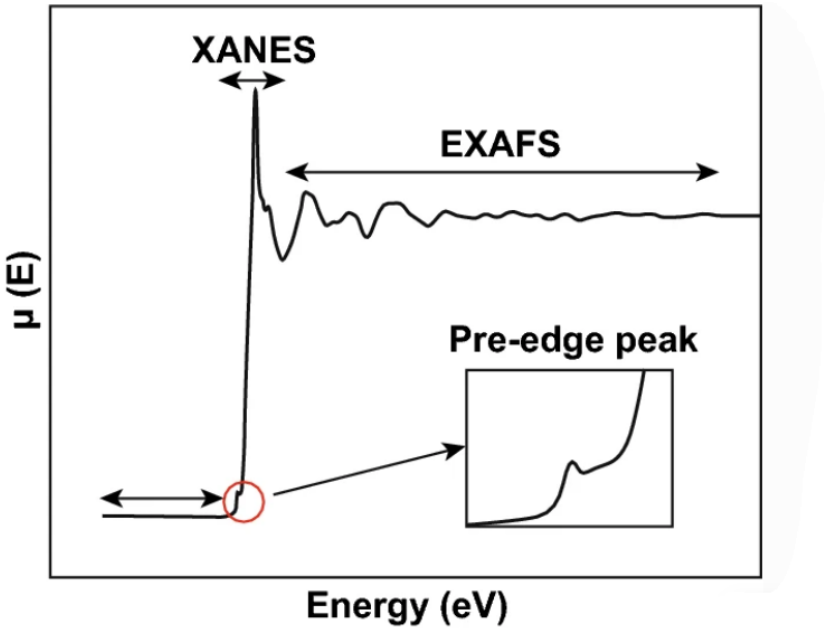

Figure 4.11:Schematic of XAFS including pre-edge XANES and EXAFS region.[59]

4.3.2 Pump probe X-ray spectroscopy with free electron laser

During my PhD, I spent three months at the SwissFEL facility in Switzerland, Villigen, as a visitor student, to perform a feasibility study of femtosecond time-resolved X-ray spectroscopy experiments on solid samples. I collaborated with the group of ALVRA beamline, which is specialized in measuring ultrafast dynamics of photochemical and photobiological systems using a variety of X-ray scattering and spectroscopic techniques, including serial femtosecond crystallography (SFX), X-ray scattering (XDS), X-ray absorption and emission spectroscopy, inelastic X-ray scattering (IXS). The possibility to perform the study of charge carrier dynamics with chemical sensitivity provided by X-rays and femtosecond resolution is a unique feature provided by free electron laser. In fact, as shown in the next paragraph, despite its excellent time

resolution, optical transient spectroscopy clearly lacks chemical sensitivity, while conventional XAS experiments provide element specific information but lack time resolution. Therefore, an experiment with a chemically sensitive X-ray spectroscopic technique such as XAFS with sub-ps time resolution can be useful to associate one or more element specific excitation pathway to the optical response on the time scale in which it occurs, an objective which can be reached only with an XFEL source.[60]

The general idea behind a pump probe X-ray spectroscopy measurement is the following: the sample is excited with an ultrashort pump pulse at a specific wavelength (typically in the visible or in the UV range) and some time before the probe pulse arrives, which in this case is an ultrashort (down to femtoseconds) X-ray free electron laser pulse with a photon energy tuned above the absorption edge under investigation.[61] The fluorescence spectrum emitted from the sample is then analyzed by a dispersive spectrometer, which uses a cylindrically bent crystal to disperse along the longitudinal axes and focus the signal on a 2D position sensitive detector, as shown in Figure 4.12.[62]

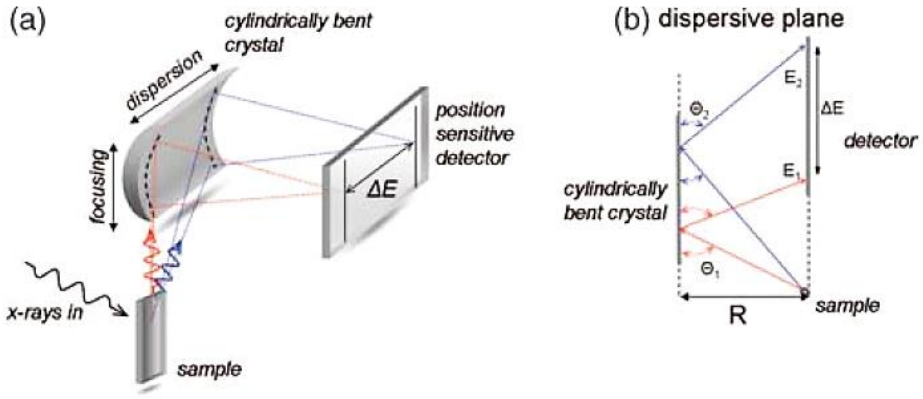

Figure 4.12: (a) Schematic of the von Hamos geometry. (b) Projection along the axis of dispersion.[62]

There are a few examples of pump probe X-ray spectroscopy performed with femtosecond relevant to the subject of this thesis. Santomauro[63] and co-workers performed a XAS experiment at the Swiss Light Source to probe the dynamics of the trapping of the photogenerated electrons in TiO_2, concluding that electrons are localized in correspondence of Ti atoms in a time lower than 300 fs, leading to the formation of Ti^{3+} centers. In addition, they confirmed that electrons are localized at Ti penta-coordinate sites. The dynamics of the photoexcitation was also investigated at SACLA, in Japan, in the case of WO_3 NPs. Uemura[64] et al. observed that immediately after optical excitation, tungsten is initially reduced from W^{4+} to a mean oxidation state of 5.3. Subsequently, tungsten oxide undergoes a change in its local structure within the following 200 ps.

All the listed cases refer to ex-situ or in-situ (on solvent dispersed particles) experiments, in which, in most cases, the oxide semiconductors or the complexes are photoexcited and the dynamics of the photogenerated carriers is followed. As a matter of fact, pump and probe XAS at FEL facilities, are still in its very early days, to the point that studies under operando condition are very rare, and are mainly obtained by adding electrolytes that act as charge donor or acceptor and not by applying an external potential[61], as a standard operando measurements requests.

4.3.3 X-ray Photoelectron Spectroscopy

X-ray photoelectron spectroscopy is a surface sensitive technique, which consists in illuminating the surface of a material with X-rays and measuring the spectrum of the emitted electrons as a function of their kinetic energy. Two characteristics make this technique very powerful: the surface sensitivity, which is in the order of a few nanometres, coupled with the ability to reveal information on the chemical states of the elements in the sample. The sample is irradiated with soft X-rays (energies lower than ~6 KeV) and the kinetic energy of the emitted electrons is analysed. The

ejection of a photoelectron comes from the complete transfer of the X-ray energy $h\nu$ to a core level electron in the sample. The X-ray photon energy can be expressed by the following equation:

$$h\nu = E_b + E_k + \phi_{spec} \tag{14}$$

in which E_b is the binding energy of the electron, E_k is its kinetic energy and ϕ_{spec} is the spectrometer work function. To determine the binding energy of the ejected electron equation (14) has to be rearranged to obtain:

$$E_b = h\nu - E_k - \phi_{spec} \tag{15}$$

in which the term on the right hand side are either known ($h\nu$ and ϕ_{spec}) or measured during the experiment (E_k). This concept is reported in Figure 4.13.

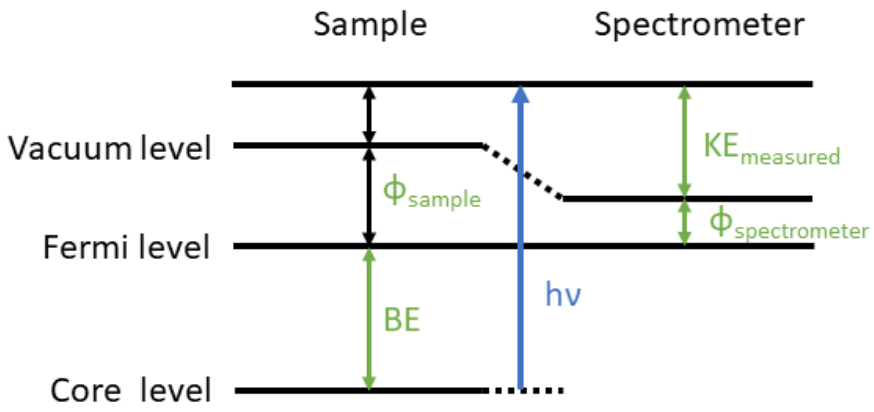

Figure 4.13: Energy level diagram that illustrates the basic of equation (14).

An example of XPS spectra for V-modified TiO_2 and TiO_2 thin films is reported in Figure 4.14.

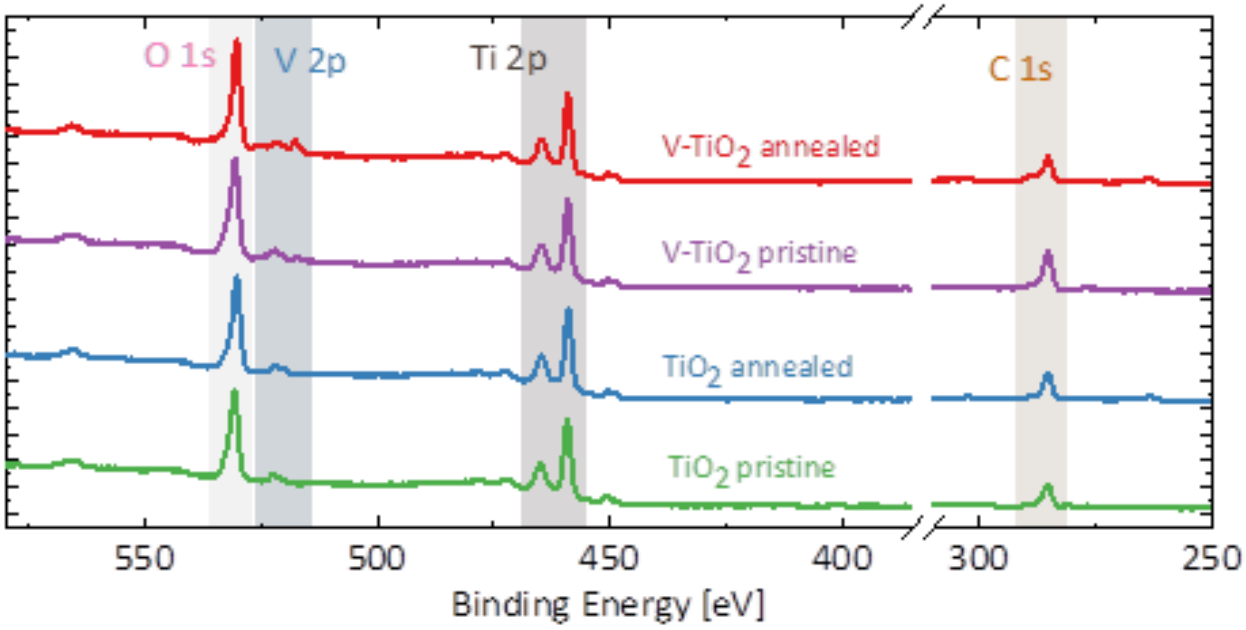

Figure 4.14: Survey XPS spectra for pristine and annealed TiO_2 and V-TiO_2 thin films.

Like other core level spectroscopy, such as XANES, XPS has the ability to determine the chemical environment of atoms present in a sample. The chemical environment, including factors like nearest neighbors and the oxidation state of the element, affects the binding energy of the photoelectron peaks. For most transition metals, the binding energy is primarily affected by the oxidation state of the metal; in fact, if an atom has lost some electron density and exhibits a positive charge, it is more energy demanding to remove an electron from that atom, and the binding energy will be higher.[65]

As already mentioned, the peculiar and thus interesting aspect of XPS is its surface sensitivity. Photoelectrons can travel only a very short distance (~5-20 Å for kinetic energies in the 5-2000 eV range) inside a solid without suffering inelastic collisions with other electrons, phonons or impurities. The energy dependence of the electron mean free path, defined as the average distance that an electron with a given energy travels between successive inelastic

collisions, is expected to follow the universal “U-shaped” curve, in most materials, as reported in Figure 4.15.

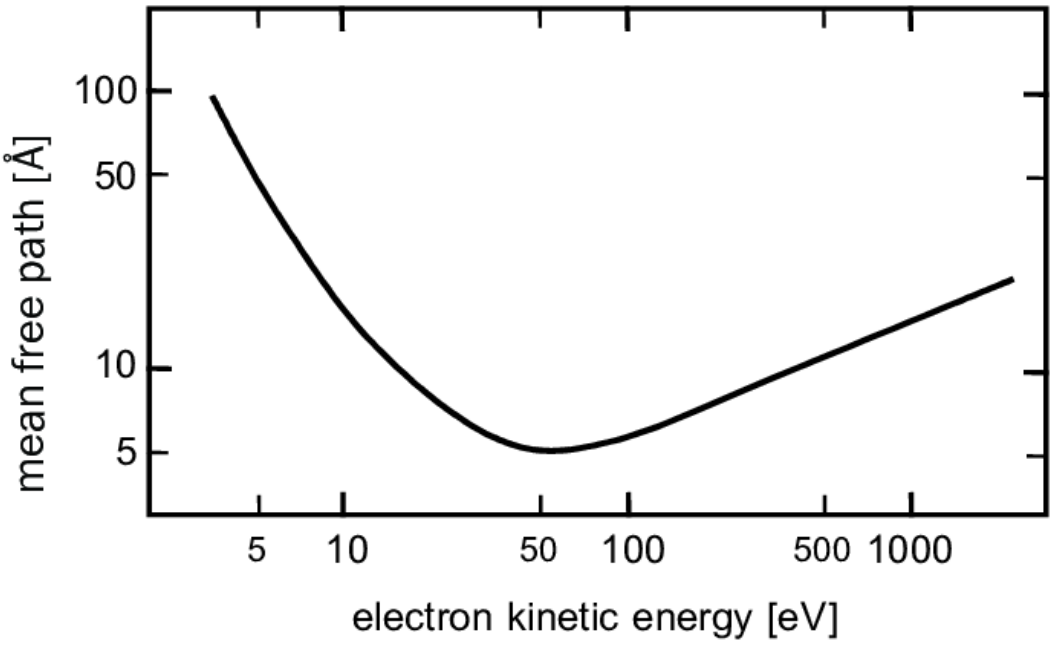

Figure 4.15: "Universal curve" of the photoelectron mean free path as a function of kinetic energy.

Actually, this curve may not be so universal, and much work, especially on the high energy side is still necessary. However, the presence of a minimum is well established. Since scattered electrons rapidly lose memory of their initial state, their contribution to the final spectrum is a shapeless background. Meanwhile, only electrons that do not undergo inelastic processes contribute to the signal with a peak. This explains why XPS information come from the very first atomic layers of the sample.[66]

4.4 Transient absorbance spectroscopy

TAS (Figure 4.16) is a powerful technique for studying charge carrier dynamics in semiconductors, which is characterized by phenomena extending over a wide range of time scales, from seconds

down to attoseconds.[67,68,69] The use of this technique in the field of photoelectrochemical energy conversion allows to investigate loss mechanisms in semiconductors associated with photocarrier relaxation, trapping and recombination.[70,71] TAS is based on the following procedure: first of all the sample is excited by an ultrashort monochromatic laser pulse (pump) and after a certain delay a second white pulse (probe) arrives to probe how the absorption of the sample was altered by the first pulse. By varying the delay time of the second pulse with respect to the first one, it is possible to measure the entire time-dependence of the absorption change.

The definition of transmittance is:

$$T = \frac{I_{trans}}{I_{in}} \tag{16}$$

where I_{trans} is the transmitted intensity and I_{in} is the incident intensity on the sample. The absorbance is defined as:

$$A = \log_{10} \frac{I_{in}}{I_{trans}} = -\log_{10} T \tag{17}$$

Since TAS measures $\Delta A \equiv A_{exc} - A_{unpumped}$ by definition, that is the difference in absorbance between the unpumped state of the sample and after its excitation with the pump pulse, this can be expressed by:

$$\Delta A \equiv A_{exc} - A_{unpumped} = \log_{10} \frac{I_{unpumped}}{I_{exc}} \tag{18}$$

It is important to notice that in order to record the absorption change in the sample induced by the excitation pulse, it is not necessary to measure the intensity I_{in} of the incident pulse.[72]

4.4.1 Transient absorbance spectroscopy setup

The layout of the experimental setup for pump-probe TAS measurements is reported in Figure 4.16. It is located at the ISM-CNR in Tor Vergata, Rome. It consists of an 80 MHz Ti:Sapphire oscillator (*Coherent Vitara-T*) that seeds a chirped pulse amplifier with broadband 800 nm pulses of 12.5 nJ. The amplifier produces 4 mJ 35 fs pulses at a repetition rate of 1 kHz. Part of this radiation is used to generate 40 fs pump pulses of different wavelengths in an optical parametric amplifier (*Coherent – Opera Solo*) at a repetition rate of 1 kHz. A white light probe pulse ($\lambda_p = 350 - 760$ nm) is generated in a commercial FTAS spectrometer (*FemtoFrame II, IB Photonics*) by focusing 3 μJ of the 35 fs 800 nm light into a rotating 3 mm crystal of CaF_2. Furthermore, a split beam configuration is employed, in which 50% of the white light passes through the sample while the remainder is used as a reference to account for pulse-to-pulse fluctuations. The pump pulse is loosely focused (circular spot with a diameter of 300 μm) onto the sample with an energy density of 100 μJ/cm^2 for λ_e =300 and 2 mJ/cm^2 for $\lambda_e = 390$ and 530 nm. The diameter of the probe pulse is much smaller (approx. 150 μm) and its delay time with respect to the pump pulse is scanned in time by varying the length of its optical path. The time broadening of the instrument response function (IRF) is approximately 80 fs.

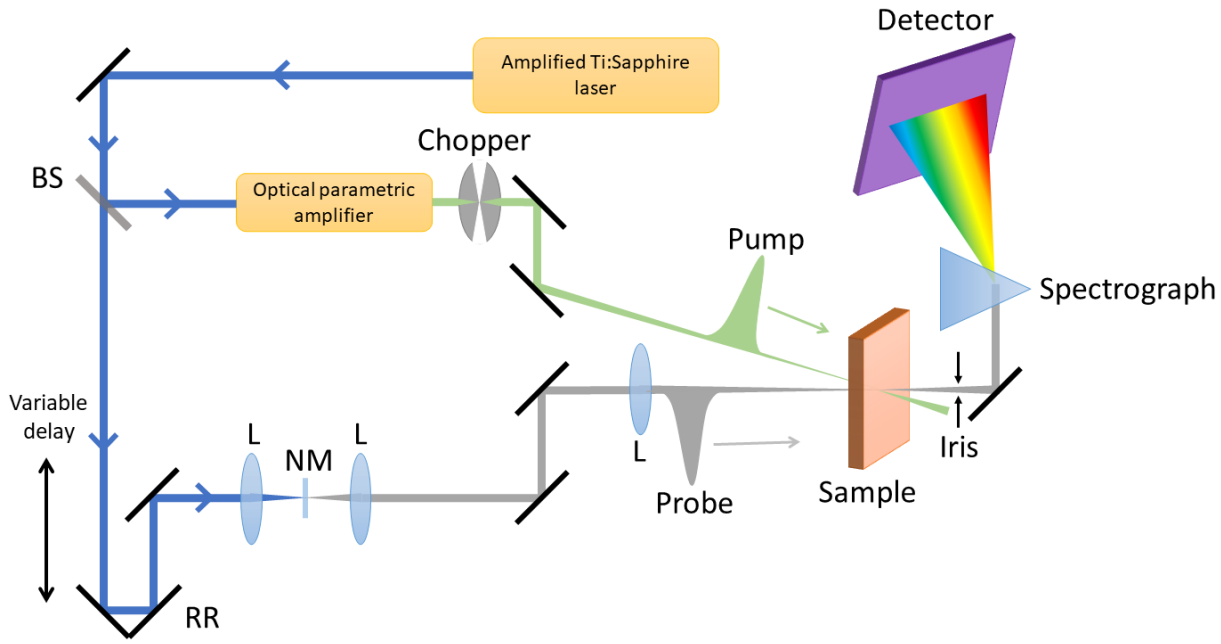

Figure 4.16: Typical layout of time-resolved absorbance experiment: amplified pulses from Ti:Sapphire laser are split into two parts using a beamsplitter BS. One part is used to pump an optical parametric amplifier that produces tunable pump pulses. The other part is delayed in a delay line (a retroreflector RR on a motorized translation stage) and then focused into a nonlinear medium NM, where white light supercontinuum is generated. The generated probe light is overlapped with pump light in the sample. The chopper is periodically closing and opening the pump beam in order to take the probe intensity measurements of the excited and non-excited sample.

The procedure for collecting TAS data is as follows: first of all, the time between the excitation and the probe beam is fixed by adjusting the retroreflector position on the motorized stage. Then, before reaching the sample, the pump beam passes through a mechanical chopper that is synchronized to the amplifier so that every other excitation pulse is blocked. The result is that the probe white light produced by the non-linear crystal and measured by the detector corresponds alternately to the transmission of the pumped I_{exc} and unpumped $I_{unpumped}$ sample; by using then equation (18) the transient spectrum is calculated for different delay times at different pump wavelength.[73] A typical TAS map is reported in Figure 4.17 for a TiO_2 thin film deposited on a quartz substrate.

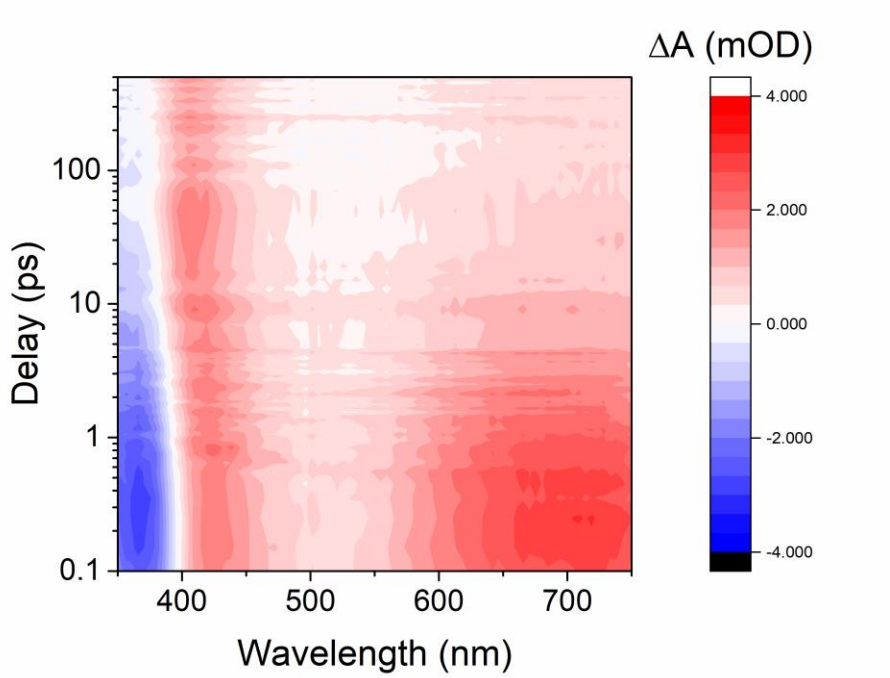

Figure 4.17: Transient absorbance map for V-TiO_2 thin film deposited on quartz substrate obtained with pump at 300 nm.

4.4.2 Interpretation of transient spectra and features

The representation in Figure 4.17 gives a quick overview of TAS data and it is really useful to highlight characteristics of transient spectra at a first sight. In order to extract valuable information, slices of the data are usually taken, cutting along the time axis and obtaining a series of TAS spectrum at different delay times, or cutting along the *y* axis, gaining the evolution in time (kinetic trace) of specified features of the spectrum. Examples of TAS spectra at different delay times and of kinetics traces taken from the map in Figure 4.17 is reported in Figure 4.18.

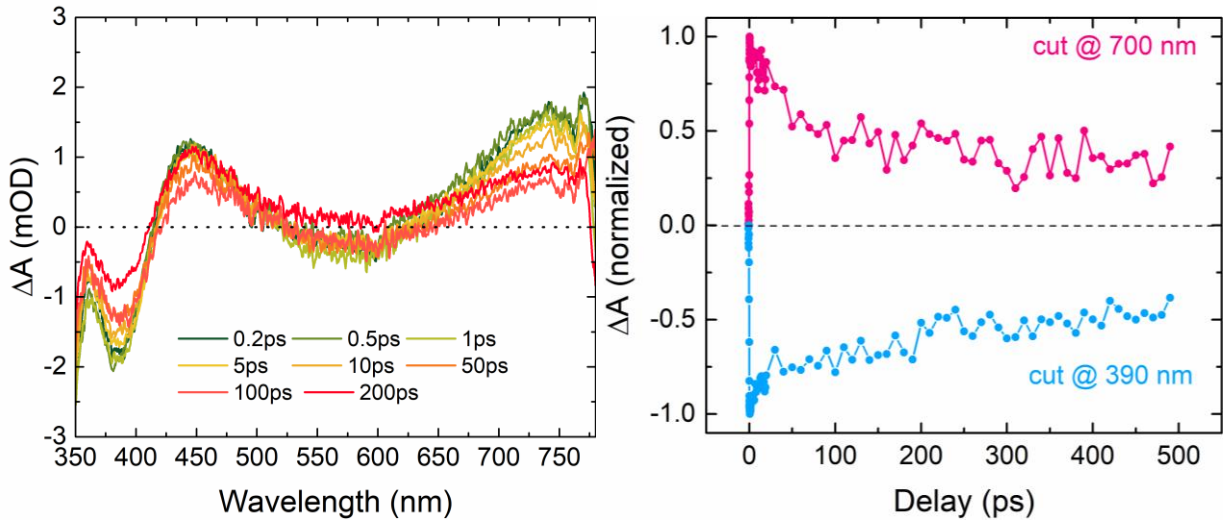

Figure 4.18: TAS spectra at different delay times (left) and kinetic traces (right) taken from map in Figure 4.17.

To understand the different contributions to TAS spectra it is necessary to start from the energy level scheme of an hypothetical oxide semiconductor, as shown in Figure 4.19. When the pump pulse excites the sample, electrons in occupied states close to the Fermi level jump to free states above the Fermi level. The usual case is when the pump pulse has an energy greater than the energy gap so that electrons from valence band can make transitions to the conduction band. This means that the concentration of absorbers (electrons) in the ground state (valence band) decreases and more light, i.e. probe light, is transmitted through the sample. As a consequence, $I_{exc} > I_{unpumped}$, and thus $\Delta A < 0$ (equation (18)). The spectral shape of this negative contribution is called *ground state bleaching* (GSB) and is shown in Figure 4.19. This signal remains until all the electrons return to the valence band, from which they were excited.

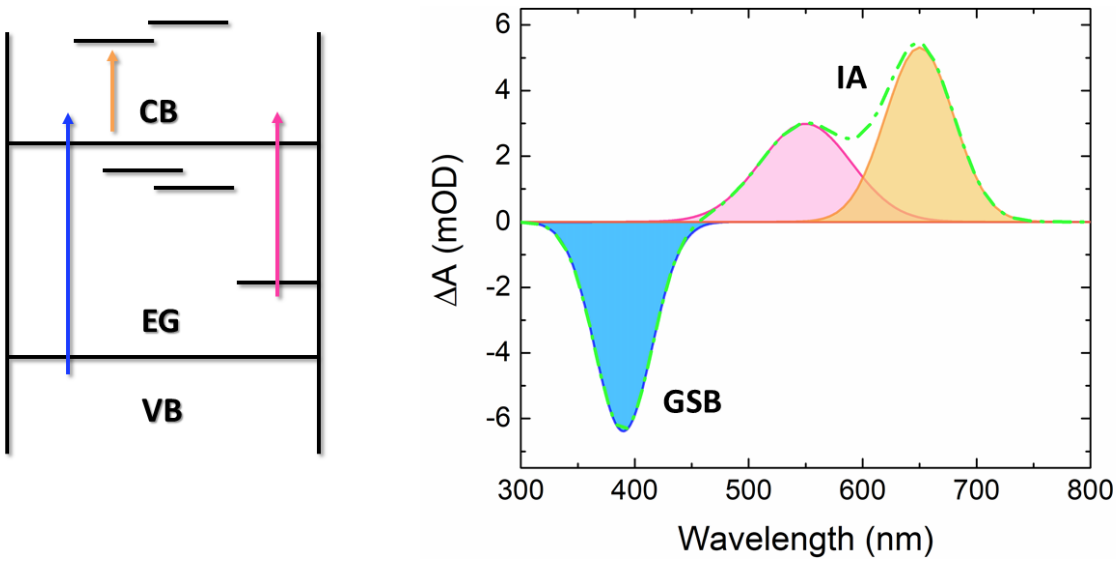

Figure 4.19: Energy levels and relative transitions (left) of an hypothetical oxide semiconductor (VB = valence band, EG = energy gap and CB = conduction band) and relative signatures (right) that appear in TAS spectra (GSB = ground state bleaching, IA = induced absorption). The green dotted line is the sum of all the contributions.

A second contribution, quite common in semiconductor oxides, is the so called *induced absorption* (IA). It originates from electrons excited by the pump pulse in transient energy states, from which they can be excited again to higher energy states by the probe. For example, electrons excited from the valence to the bottom of the conduction band can be excited again in higher energy states still inside the conduction band. This process can only occur when the system is already excited, adding an additional absorption contribution to spectrum. The result is that $I_{exc} > I_{unpumped}$ since the transmitted light is higher in the excited system thanks to the presence of extra absorption and thus $\Delta A > 0$. In oxide semiconductors, this contribution can be related to free electrons in the conduction band or trapped electrons or holes in energy levels inside the energy gap, such as surface states or traps.

The real challenge with TAS spectra is to distinguish all the underlying processes that occur in the system, which show spectral features that are often mixed in the total transient spectrum. Information coming from different characterization such as photoelectrochemical and X-ray measurements or DFT calculations are essential for providing the basis for a reasonable interpretation of the data.[70]

5 MODIFICATION OF TiO_2 THIN FILM WITH VANADIUM

The incorporation of 3d-transition metals in TiO_2 crystal structure is an effective approach to extend light absorption of TiO_2 towards the visible range of the solar spectrum.[74,75,76,36] The introduction of these species in substitutional sites of TiO_2 results in the creation of energy states in the band gap of the host matrix, as reported by Umebayashi et al.[77] They performed *ab initio* calculations for systematically studying the position of V, Cr, Mn, Fe and Co donor states and pointed out the shifting of these intragap states towards the bottom of the conduction band with increasing atomic number, as reported in Figure 5.1; in particular, vanadium was predicted to create an intragap state near the bottom of the conduction band of TiO_2. The energy of the band gap here reported is smaller than that experimentally observed due to the shortcoming of the local density approximation (LDA)[78] and the generalized gradient approximation (GGA).[79]

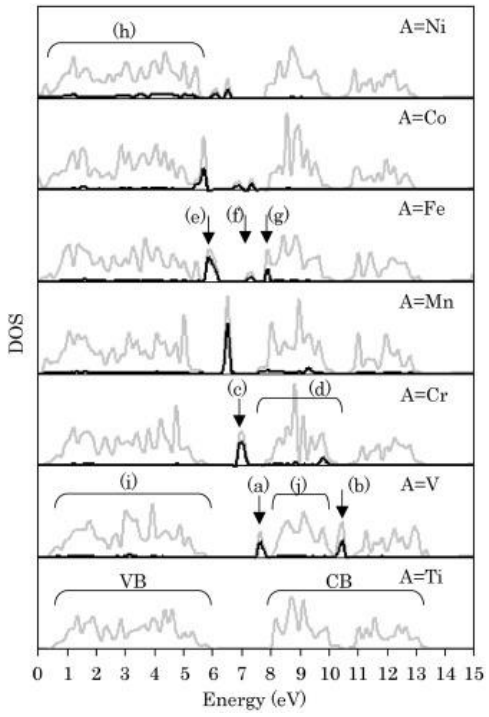

Figure 5.1: Calculated electronic DOS for TiO_2 modified with transition metals in substitutional sites.[77]

5.1 Morphological characterization of the surface of the photoanode

TiO_2 and V-TiO_2 thin films were deposited by radiofrequency magnetron sputtering following the procedure reported at the end of paragraph 3.2.4. For the realization of photoanodes, a soda lime glass coated by a 200 nm thick layer of fluorine-doped tin oxide (FTO) from Ossila was used as substrate, meanwhile, for transient absorbance measurements, quartz substrates (from Electro-Optics Technology) were used, in order to provide UV light transmission. Four levels of V concentration were investigated, corresponding to atomic ratios V/(Ti+V) = 2, 4, 6, and 8 at. %. Accordingly, the samples will be indicated as V-TiO_2 (x%) with x = 2, 4, 6, or 8. The V content of every sample was evaluated by energy-dispersive X-ray spectroscopy (EDS) using a Leica Cambridge Stereoscan 360 scanning electron microscope equipped with an Oxford Instruments X-ray detector for energy-dispersive X-ray microanalysis.

In Figure 5.2 an AFM topography of the surface of a V-TiO_2 (8%) photoanode is shown (with FTO as substrate), while on the right, the surface of a similar sample deposited on quartz for FTAS measurements is reported.

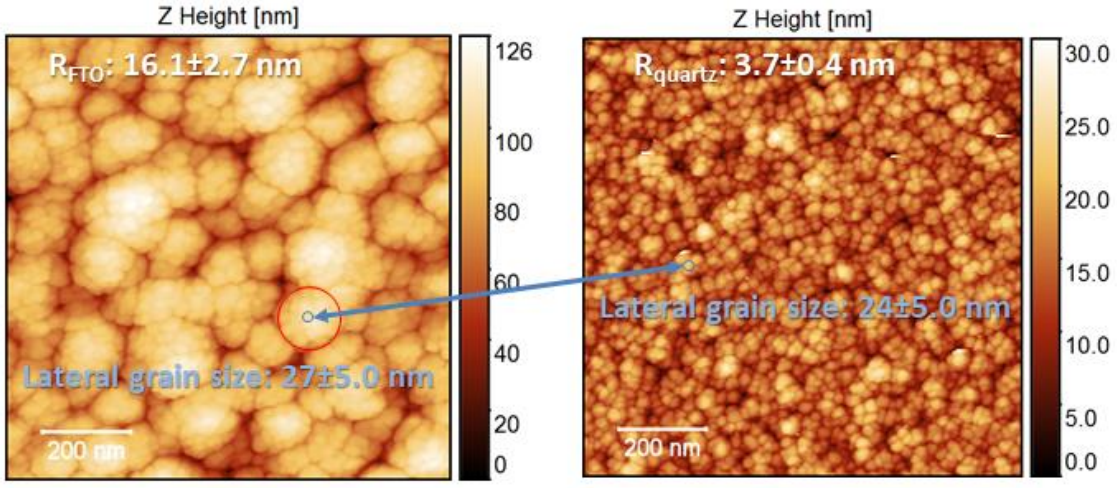

Figure 5.2: Surface morphology of V-TiO_2 (8%) photoanodes on FTO (left) and V-TiO_2 (8%) on quartz (right).

No relevant differences were found between V-modified and unmodified TiO_2 samples. In photoanodes, two different structures are visible: one is clearly induced by the morphology of the FTO surface (red circle) and is not present on the sample deposited on quartz and the other (blue circle) is attributed to TiO_2 crystal grains, with a lateral size of 27 ± 5 nm. The latter structure is also present on the surface of TiO_2 deposited on quartz, with a lateral size of 24 ± 5 nm. The roughness of the two films is 16.1 ± 2.7 nm for photoanodes and 3.7 ± 0.4 for TiO_2 on quartz. The higher roughness of the photoanodes reflects the high roughness of the underlying FTO substrate, which is 15 ± 2 nm. The roughness of the quartz substrates is only 0.7 ± 0.2 nm; therefore, the observed film roughness likely originates from columnar grains of slightly different heights, which is typical of sputter-deposited films.

5.2 X-ray diffraction

XRD was used to identify the crystallographic phases present in the samples and to evaluate possible changes induced by V incorporation. For XRD measurements a *PANalytical X'Pert Pro* automated diffractometer was employed, equipped with an *X'celerator* multielement solid-state detector. The diffractometer was operated in Bragg-Brentano θ/2θ para-focusing geometry using Ni-filtered Cu K_α radiation without a monochromator in the diffracted beam. All samples undergo an annealing treatment after the deposition, which consists in heating them at 400 °C for 16 hours in air, in order to improve the crystallinity. Since the thickness of the samples used for XRD characterization is 130 nm, the signal from the FTO substrate is also detected and it affects the XRD patterns. In Figure 5.3 the XRD patterns for the FTO coated glass, unmodified TiO_2 and modified (4% and 8%) TiO_2 films are reported.

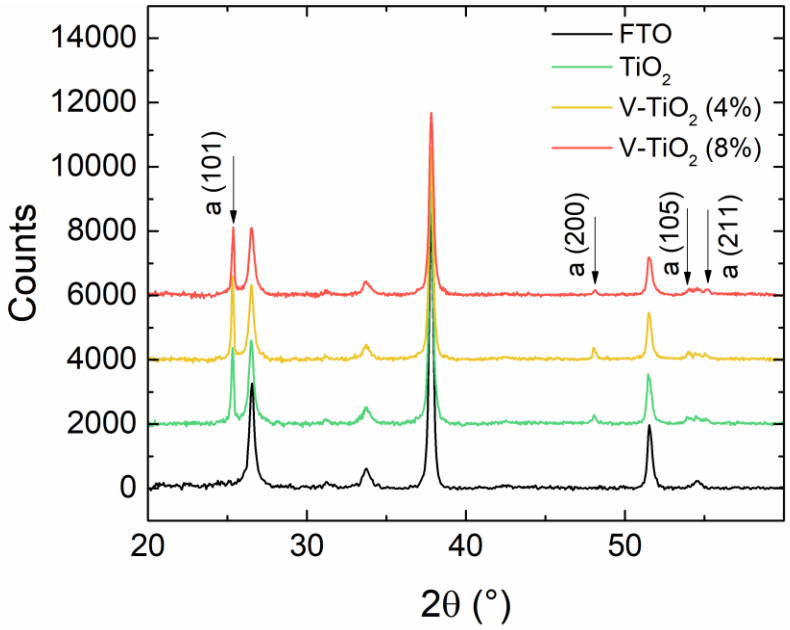

Figure 5.3: XRD patterns of the FTO layer of the substrate, unmodified TiO_2 and V-modified TiO_2 films. The detected Bragg reflections of anatase TiO_2 are indexed; the other peaks come from the FTO layer.

The patterns are dominated by the Bragg reflections arising from the FTO substrate. In addition, the (101) diffraction peak at $2\theta \approx 25.3$, typical of anatase TiO_2 (lattice parameters a = b = 3.783 Å, c = 9.510 Å), is clearly visible in all samples. The other reflections of anatase are much weaker than expected for an isotropic distribution of crystallite orientations or even not visible, indicating that the films are textured with the (101) planes parallel to the surface. The other common polymorphs of TiO_2, that is, rutile and brookite, are not detected. The positions of diffraction peaks are the same for all samples within the experimental uncertainty, indicating that the lattice parameters vary less than 0.1% with the V concentration. This is expected at low V contents given the similar atomic radius of the two elements. The d-spacing of the (101) planes is reported in Table 5.1 as a function of composition and for different thicknesses at the highest V content. The full width at half-maximum (FWHM) of the (101) peak is about 0.16°, compared to an instrumental FWHM of 0.12°, and shows small variations with the composition. Such a small broadening

implies a large uncertainty in the determination of the longitudinal (perpendicular to the sample surface) crystallite size L_s, which was calculated using Scherrer's equation:

$$L_s = \frac{k\lambda}{\beta \cos(\theta)} \tag{19}$$

where k is a dimensionless geometrical factor that depends on the shape of the crystallite (with a typical value of 0.9), λ is the X-ray wavelength of the X-ray source ($\lambda = 0.154$ nm), β is the FWHM of the (101) peaks after the correction with the instrumental FWHM, and θ is the Bragg angle. L_s values are reported in Table 5.1. The crystallite size ranges between 80 and 100 nm for all samples, the only exception being the thinnest V-TiO_2 (8%) film, where the crystallite size is about 60 nm. This result is consistent with the reduced thickness because XRD measures the elongation of the diffracting column in a direction perpendicular to the surface. The crystallite size values should be considered as lower-bound estimates because other factors, such as the root-mean-square microstrain, may contribute to the broadening of Bragg peaks.

Table 5.1: Thickness, (101) lattice spacing and crystallite size as determined from Scherrer's equation (19).

V content (at%)	Thickness (nm)	d (Å)	L_s (nm)
0	130 ± 4	3.514 ± 0.001	80 ± 10
4	130 ± 4	3.515 ± 0.001	100 ± 10
8	130 ± 4	3.517 ± 0.001	75 ± 10
8	200 ± 4	3.513 ± 0.001	84 ± 10
8	50 ± 12	3.514 ± 0.001	59 ± 10

5.3 Raman spectroscopy

Raman spectra were measured on order to determine the dominant phase. They are reported in Figure 5.4.

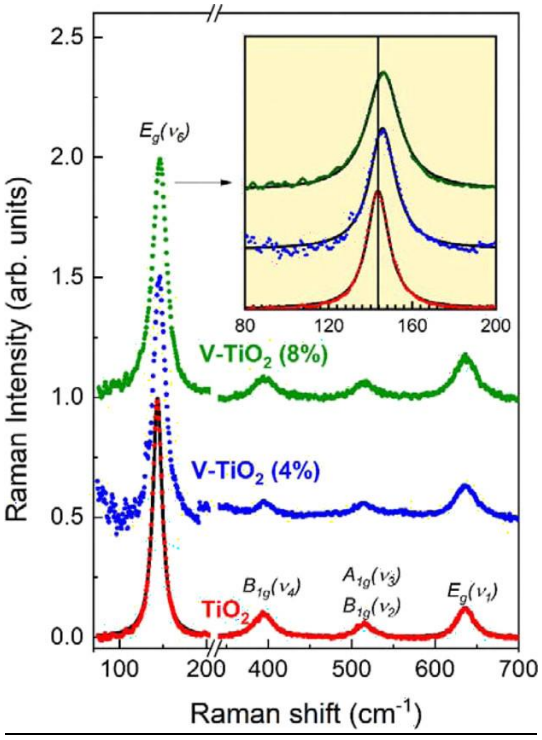

Figure 5.4: Raman spectra of the unmodified and V-modified TiO_2 samples. The colored symbols correspond to the experimental spectra. A representative fitting using Lorentzian lineshapes is shown in the case of the unmodified sample. The inset shows magnification of the spectra around the main $E_g(\nu_6)$ peak along with the corresponding fitting. The vertical line denotes the position of the $E_g(\nu_6)$ peak of the unmodified sample.

Four peaks, at 144, 395, 515, and 636 cm^{-1} corresponding to the E_g, B_{1g}, B_{1g}/A_{1g}, and E_g normal modes, respectively, are evident.[80] They are characteristic of the anatase polymorph, while peaks due to rutile were not detected. Table 5.2 lists the positions and the FWHM of the most intense $E_g(\nu_6)$ peak, which was determined after fitting with a Lorentzian function.

Table 5.2:FWHM, absolute position ω, and shift Δω of the $E_g(\nu_6)$ Raman peak measured on the thin films grown on FTO/glass substrate. The uncertainties are the standard errors of the fitting. The shift is defined as $\Delta\omega \equiv \omega - \omega_0$, assuming $\omega_0 = 144\ cm^{-1}$ for bulk TiO_2.

Sample	FWHM (cm^{-1})	ω (cm^{-1})	Δω (cm^{-1})
TiO_2	12.7±0.1	143.6±0.1	-0.4±0.1
V-TiO_2 (4%)	15.1±0.2	145.8±0.1	+1.8±0.1
V-TiO_2 (8%)	18.9±0.1	146.1±0.1	+2.1±0.1

The FWHM values indicate a good crystalline quality of the films. With the increasing V content, both a broadening and a blue shift $\Delta\omega = \omega - \omega_0$ of the peak (relative to the corresponding value for bulk anatase, ω_0 = 144 cm^{-1}) are observed. A blue shift ofthe $E_g(\nu_6)$ Raman mode was reported for anatase films grown on different substrates.[81] It was linearly correlated with the stress (and strain) in the films, as calculated from the variation of the lattice parameters determined by XRD. According to the data of Alhomoudi[81] and Newaz, a blue shift of ∼2 cm^{-1}, as listed in Table 5.2 for V- modified samples, would correspond to a compressive strain of ∼0.6%. In the present case, however, XRD suggests that the variation of the lattice parameters among different samples is below 0.1%. Therefore, other V-related factors must be responsible for the observed blue shift of the Raman spectral features. Similar blue shifts were previously reported for anatase films deposited on glass substrates at 350 °C; they were attributed to local distortions and to the presence of bonds with different force constants, arising from the incorporation of substitutional V^{4+} cations in the Ti sublattice.[82] These factors may also contribute to the V-induced broadening of Raman features, which is in qualitative agreement with the broadening of the (101) Bragg peak observed at the highest V incorporation level. The incorporation of V in the TiO_2 lattice leads to an increased disorder and to a distribution of bond strengths, which appears to enhance phonon scattering. Size effects as a genuine broadening mechanism can be excluded because they should also induce a peak asymmetry, which is not observed here, and they become evident for a crystallite size smaller than 20 nm, well below the XRD estimate discussed above.[83]

5.4 X-ray photoelectron spectroscopy

XPS was used to quantify the V content in the surface region and to probe its oxidation state. It is important to stress that this technique probes the surface region of the films, which plays the most important role in charge transfer at the semiconductor-electrolyte interface. Ex situ XPS

measurements were performed on both pristine and annealed unmodified TiO_2 and V-TiO_2 (6%) films. The spectra exhibit contributions of O 1s, V 2p, and Ti 2p core levels along with a C 1s contribution originating with adventitious C due to air exposure.[84,85,86] Data analysis was carried out with the CasaXPS codes.[87] A Shirley algorithm was employed to calculate the background of all spectra except the V 2p signal, for which a linear background was used. A symmetric pseudo-voigt line-shape was used for all peaks. Due to air exposure of the samples, the adventitious C 1s signal reported in Figure 5.5 (left), caused by adsorbed organic molecules, is always present. The C 1s signal was fitted by two peaks: the main one due to strictly adventitious carbon and the less intense one, at higher binding energies (~ 288.2 eV), due to highly oxidized carbon[84].

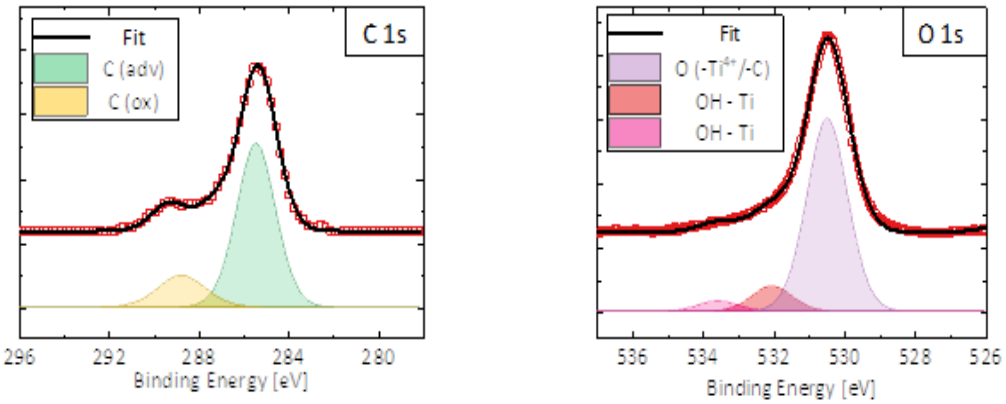

Figure 5.5: XPS spectra of C 1s (left) and of O 1s (right) for the annealed V-TiO_2 (6 %) thin film.

The O 1s main peak (Figure 5.5 (right)) is related to unresolved components due to O bound to Ti or V in the bulk (majority contribution[84]) and to surface C (minority contribution[84,85]). In order to compute the O concentration in the films, the amount of O bound to surface C, estimated from the high binding energy component of the C 1s spectra, was taken into account. The two greater binding energy components of the O 1s spectra are due to O atoms in hydroxyl groups adsorbed by sample surface defects.[86] The intensity of all components was normalized to tabulated cross

sections in order to calculate relative atomic compositions. For what concern Ti, V, and O signals, they indicate, as expected, an O/(Ti + V) ratio of 2.0 ± 0.2.

In Figure 5.6, V $2p_{3/2}$ XPS spectra for the pristine and annealed V-TiO_2 (6%) films are reported.

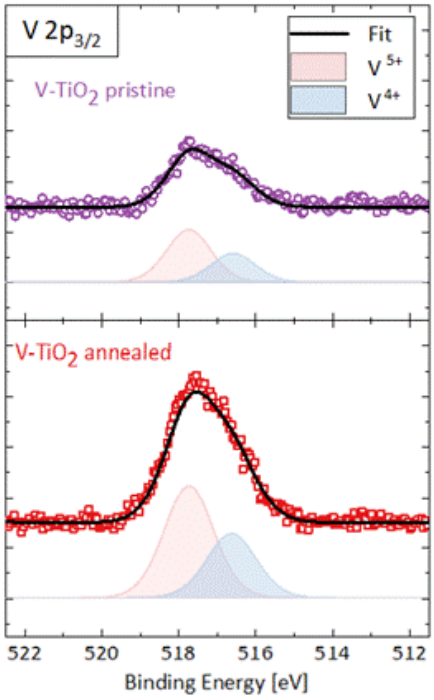

Figure 5.6: V $2p_{3/2}$ XPS spectra of the V-TiO_2 (6 %) film before (top) and after (bottom) annealing. Empty symbols: background-subtracted experimental spectra; continuous lines: fits; filled contours: V^{4+} and V^{5+} fitting components.

By comparing its intensity with that of Ti, it is possible to quantify the V concentration (calculated as V/(Ti + V)) in the surface layer probed by XPS (a few nanometers). For the pristine film, a V concentration of 6 ± 1% was found, in agreement with the EDS determination. Instead, annealing leads to a significant increase of the V concentration to 16 ± 2%, indicating that thermal treatment promotes the migration of V atoms toward the surface. The line shape reported in Figure 5.6 clearly exhibits two components, which were decomposed by a fitting procedure. By comparing the

binding energies of the two components (516.6 and 517.7 eV), which do not change upon annealing, to those reported by Silversit et al.[88], it is reasonable to conclude that V is found in both 4+ and 5+ oxidation states. The fraction of V^{4+} was 0.38 ± 0.10 in the pristine sample and 0.32 ± 0.10 in the annealed sample. These numbers clearly refer to the surface of the films, as XPS is very surface-sensitive. XANES measurements are reported in the next paragraph, in order to gain more information from the bulk part of the sample.

5.5 X-ray absorption near edge spectroscopy

The study of the local environment of V atoms in the TiO_2 host matrix provides an essential prerequisite for understanding the optical properties and the charge carrier dynamics. To do this, X-ray absorption near edge spectroscopy (XANES) was employed. These measurements were performed at the BM08 (LISA) beamline of the ESRF in Grenoble, France, using fluorescence yield acquisition mode.

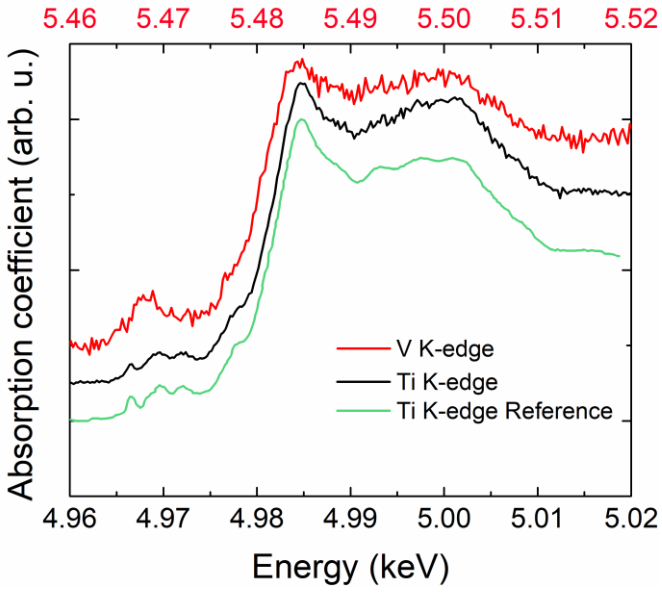

Figure 5.7: V and Ti K-edge XANES of V-TiO_2 (4%) thin films. The green line is a reference spectrum of Ti K-edge for TiO_2 anatase. The energy scale for the Ti K-edge is reported at the bottom, meanwhile the one for the V K-edge is at the top.

Spectra reported in Figure 5.7 were acquired at Ti K and V K-edge for V-TiO_2 (4%) in order to determine the incorporation site of V. A reference spectrum of Ti K-edge in anatase structure is also reported.[89] The presence of a background signal due to Ti K_β made difficult to measure the spectra with a good signal-to-noise ratio. However, a qualitative analysis is still possible. In fact, from Figure 5.7, it is clearly evident a close correspondence of the line shape for Ti and V K-edge in the post-edge. In addition, they are both similar to the reference anatase spectrum. Since the features in XANES spectra depend also on the spatial configuration of atoms around the absorber, if spectra at Ti K-edge and V K-edge are similar it means that their local environment is the same. This indicates that V is substitutional, i.e. V takes the place of Ti inside the host matrix. For what concerns the pre-edge part, the V spectrum is characterized by a spectral feature with a maximum at 5.469 KeV, which is due to dipole and quadrupole transitions to bound hybridized orbitals originating from O p and V d atomic ones.[75] This peak recalls the pre-edge peak present in V_2O_5 and VO_2,[75] but it is difficult to establish a direct correspondence since XANES line shape depends not only on the oxidation state of the absorber but also on its local point symmetry and the elemental composition of its first coordination shells. However, an oxidation state between 4+ and 5+ for V is reasonable. To support these conclusions, it is useful to compare data from XANES and XPS measurements with the same data coming from V-modified TiO_2 samples prepared with different methods. In particular, two studies by Rossi et al.[75] on NPs (in which I collaborated in the photoelectrochemical characterization, see paragraph 7.2 for more details) and by El Koura et al.[89] on thin films, report a detailed analysis of V local environment in TiO_2 modified with this element, supporting their conclusions with ab initio spectral simulations of Ti and V K-edge XANES spectra. The relevant results for the comparison with my samples are reported in Table 5.3.

Table 5.3: Comparison between structural and electronic characterization of V-modified TiO_2 samples taken from two different studies by Rossi et al.[75] and by El Koura et al.[89]

Reference	Rossi et al.[75]	El Koura et al.[89]	This thesis
Samples	NPs (IGC)	Thin film (Sputtering)	Thin film (Sputtering)
Materials	V-TiO_2	V-TiO_2	V-TiO_2
XRD	Mix of Anatase and Rutile	Anatase	Anatase
XANES	*Ti K-edge*: characteristic line shape of a mix of anatase and rutile structure	*Ti K-edge*: characteristic line shape of anatase structure	*Ti K-edge*: characteristic line shape of anatase structure
	V K-edge: pre-edge peak similar to V_2O_5 in shape and VO_2 in intensity, main edge line shape similar to a mix of anatase and rutile structure	*V K-edge*: pre-edge peak at 5.470 keV similar to VO_2 in intensity and between VO_2 and V_2O_5 in energy position, main edge line shape similar to anatase structure	*V K-edge*: pre-edge peak at 5.469 keV, main edge line shape similar to anatase structure
XPS			Prevalence of V^{5+} near the surface, migration of V cations close to the surface after annealing

Ab initio simulation	Good agreement with experimental XANES results for anatase and rutile	Good agreement with experimental XANES results for anatase and rutile

All the features pointed out in the previous qualitative discussion are in full agreement with more accurate and quantitative analysis reported in the papers I cited above. Putting together data from XRD, XPS and XANES it is possible to confirm with a good level of confidence that V occupies substitutional sites inside TiO_2 structure without introducing relevant modification in the host matrix and its oxidation state varies from 4+ in the bulk to 5+ close to the surface of the thin film.

6 CONVERSION EFFICIENCY AND PHOTOELECTROCHEMICAL CHARACTERIZATION OF VANADIUM MODIFIED TiO_2 PHOTOANODES

In Figure 6.1 IPCE spectra of V-modified TiO_2 photoanodes are reported for different V concentrations and film thicknesses. These measurements are useful to highlight the change in spectral response induced by the introduction of V.

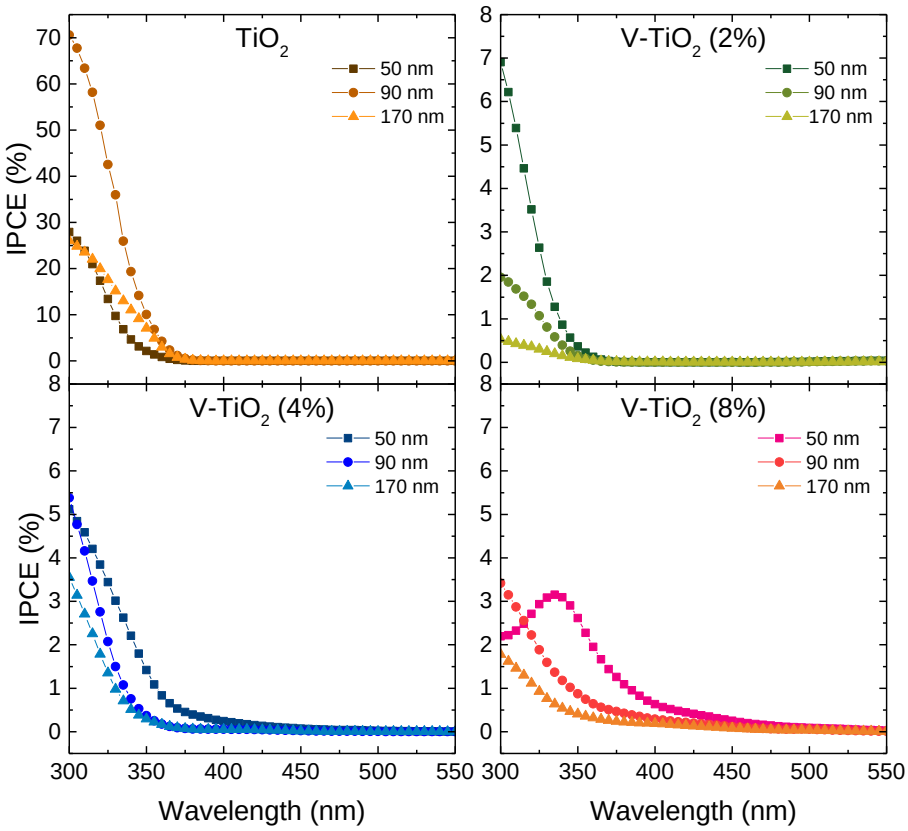

Figure 6.1: IPCE spectra of V-TiO_2 (0, 2, 4 and 8%) photoanodes for different film thickness, recorded at 0.5 V using the experimental setup described in paragraph 4.1.

Since the photoelectrocatalytic activity of photoanodes revealed by IPCE is not related only to light absorption, but also to charge transport, it is possible to extract valuable information

regarding the charge carrier dynamics in the bulk, providing the basis for a deeper analysis in the next paragraph using transient absorption spectroscopy. In discussing these spectra, it is useful to distinguish two spectral ranges: the visible range for wavelengths longer than 390 nm and the UV range for wavelengths below 390 nm.

6.1 Thickness dependence

By considering samples with the same V content but different thickness, it is possible to analyze the dependence of IPCE on the film thickness. In Figure 6.1 a comparison between different thicknesses (50 nm, 90 nm and 170 nm) is reported for different V content (0%, 2%,4% and 8%). I will discuss separately the trends in the spectra for V-modified and for unmodified photoanodes. In this regard, it is important to recall that the conversion efficiency depends on a trade-off between light absorption and charge carrier recombination in the bulk. This translates in an optimal thickness that maximizes light absorption and minimizes charge recombination. Evidence of this is the behavior of the unmodified samples, for which the best performing photoanode has a thickness of 90 nm, which is between 50 nm and 170 nm. The Lambert-Beer law, which relates the attenuation of light to the properties of the material through which the light is travelling, is:

$$I(x) = I_0 e^{-x/\delta} \tag{20}$$

The penetration depth δ corresponds to the distance from the sample surface in which the incident intensity I_0 decreases by 63.2%. It is expressed by $\delta = \lambda/4\pi n_2$ (n_2 being the imaginary part of the refractive index) and it ranges between 17 nm and 40 nm, using values of n_2 taken from refs [90,91], with $\lambda = \lambda_e = 300$ nm. This means that a thickness of 90 nm corresponds to 2 to 4 times δ, meaning that the absorption of light is around 90% in the sample with this thickness. In thinner

photoanodes, part of the light pass through the film without being absorbed, meanwhile in the thicker one, the recombination of charges causes a reduction of the total photocurrent generated. On the contrary, for V-modified photoanodes there is a decrease of IPCE in both UV and visible ranges with increasing film thickness. This behavior can be understood considering the effect of the limited thickness (comparable to the attenuation length for UV radiation) combined with the enhanced recombination rate at high V incorporation (this will be discussed in the next paragraph). Following the previous reasoning, the longer path that electrons have to travel through the bulk before reaching the FTO substrate together with the increasing recombination rate induced by V brings to a reduction of the collected photocurrent. This effect is probably the responsible of the peak in the IPCE curve for the 8% modified 50 nm film at about 340 nm.

6.2 Doping level dependence

The overall photoelectrocatalytic activity in the UV range decreases with V incorporation. This is visible in Figure 6.2 in which samples with the same thickness and different V content are compared. On the other hand, the photoelectrocatalytic activity in the visible range (up to ≈ 550 nm) increases with the V content. In particular, the unmodified sample is completely inactive as expected, but also the 2% modified one does not show any activity in this range. On the contrary, for the 4% sample a weak tail is present while for the 8% modified sample the gain in photoelectrocatalytic activity is well visible.

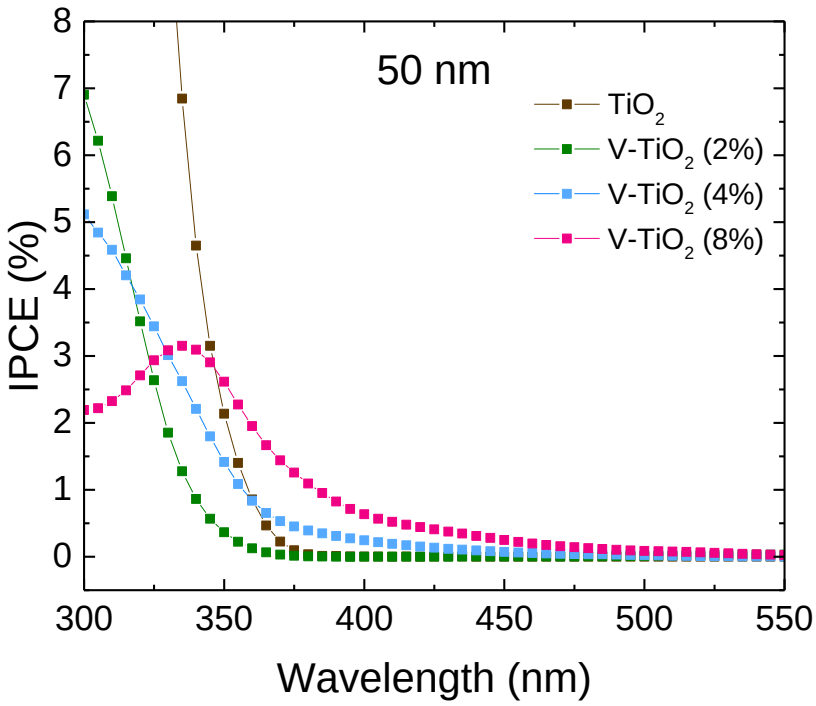

Figure 6.2: Comparison between IPCE spectra of V-modified and unmodified TiO_2 thin films with a fixed film thickness (d = 50 nm).

To study the charge carrier dynamics in these photoanodes under UV illumination, electrochemical impedance spectroscopy was performed using a sinusoidal wave 10 mV rms generator in a range between 10 kHz and 0.1 Hz, applying 0.5 V to the photoanode (same voltage bias as in the IPCE spectra). Data were collected in the dark and upon monochromatic UV illumination (300 nm, 0.1 mW/cm^2) for pure TiO_2 and V-TiO_2 (8%). Results are reported in Figure 6.3. The equivalent circuits used to fit EIS data are different for pure and V-modified samples. In particular, for TiO_2 a simple Randles circuit[51,52] was used, in which the series resistance R_s takes into account several contributions of the system such as the resistance of FTO/TiO_2 interface, the resistance of bulk and electrolyte, and C_{sc} and R_{sc} represent the capacity and resistance of the space charge region at the semiconductor/electrolyte interface, respectively.

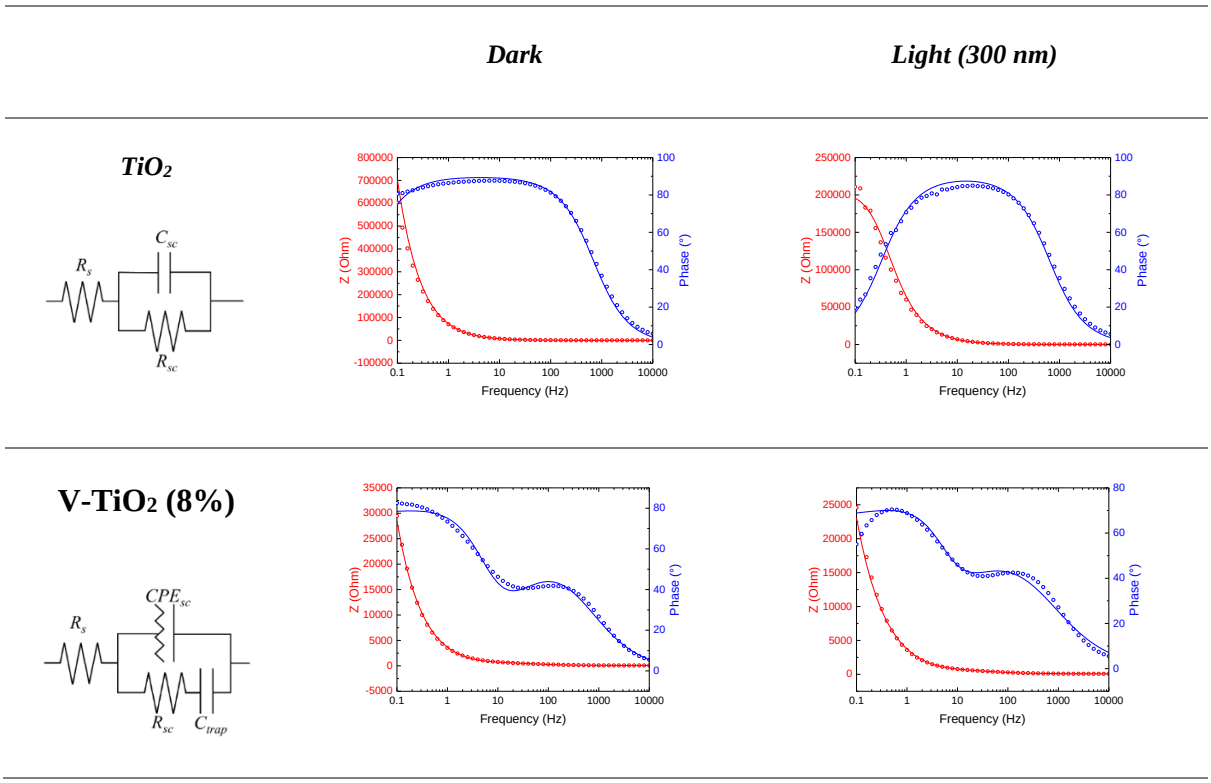

Figure 6.3: Bode plots of TiO_2 and V-TiO_2 (8%) samples obtained with EIS in the dark and upon UV illumination (300 nm). The fits with the equivalent circuits are also reported.

The values of the circuit components obtained from the fit are reported in Table 6.1.

Table 6.1: Values of equivalent circuit components for pure TiO_2 in the dark and upon UV illumination

TiO_2	**Dark**	**Light**
R_s (Ω)	106	106
C_{sc} (μF)	2.19	2.35
R_{sc} (kΩ)	2770	205

While R_s remains constant in the dark and under UV illumination, the value of C_{sc} increases slightly, while R_{sc} decreases from 2770 kΩ in the dark to 205 kΩ. This considerable change is probably due to the electron-hole formation in the space-charge region under UV illumination and the consequent migration of these charge carriers towards the semiconductor/electrolyte interface

(holes) and the back contact with FTO (electrons). In fact, as CV measurements shown in Figure 6.4, the photocurrent under monochromatic UV illumination is relatively high considering the small incident power. For V-TiO_2 (8%) a different equivalent circuit was required to fit the EIS data. Specifically, it was necessary to replace the capacitor with a constant phase element (CPE_{sc}) which is often adopted to described systems with surface or bulk states in the bandgap[12], as in the case of V-modified photoanodes. Moreover, the addition of a capacitance C_{trap} in series with R_{sc} was necessary. The values of the circuit components found from the fit are reported in Table 6.2.

Table 6.2: Equivalent circuit components values for V-TiO2 (8%) in dark and upon UV illumination.

V-TiO₂ (8%)	**Dark**		**Light**	
R_s (Ω)	71		68.2	
CPE_{sc} (μMho)	26.7	N = 0.767	45.7	N = 0.692
R_{sc} (kΩ)	0.98		1.42	
C_{trap} (μF)	27		17.9	

The presence of the series capacitance could be related to the vanadium intragap level, which induces an accumulation of THs (see TH signal under UV illumination in FTAS measurements) at the surface of the semiconductor.[92] This capacitance appears responsible for the non-resistive behaviour at low frequency under illumination, witnessed by the high value of the phase for V-TiO_2, within this frequency range, with respect to pure TiO_2. Therefore, the poor performance of the V-modified films in the UV region, shown in IPCE spectra and confirmed by CV measurements in, can be attributed to trapping and recombination of charge carriers, in agreement with the interpretation of FTAS measurements. UV illumination has a small effect on the electrochemical impedance spectra of V-modified films, which is consistent with the small photocurrent in Figure 6.4. The main change is a small decrease of the phase at low frequency,

indicating a more resistive behaviour. This could originate from trap filling by photogenerated charges and with the availability of an easier conduction path for excess carriers. However, the small entity of the light-induced changes makes it difficult to discuss quantitatively the corresponding changes in the values of circuital elements.

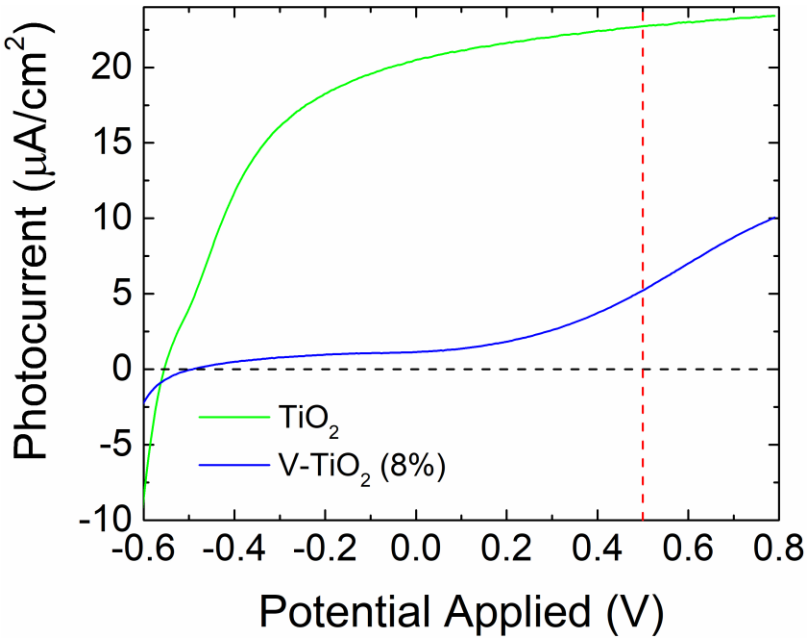

Figure 6.4: Differential cyclovoltammetry measurements (light-dark) performed with illumination at 300 nm. Red line indicates the potential used for IPCE and EIS measurements.

7 TIO_2 CHARGE CARRIER DYNAMICS INVESTIGATED BY ULTRAFAST TRANSIENT ABSORBANCE SPECTROSCOPY

Before studying the charge carrier dynamics inside unmodified and V-modified TiO_2 thin films, preliminary static transmission spectra were measured for different film thickness and V content, in order to investigate their optical properties. Samples were deposited on quartz substrate to avoid light absorption in UV range (typical of standard glass). Results from transmission spectra are reported in Figure 7.1.

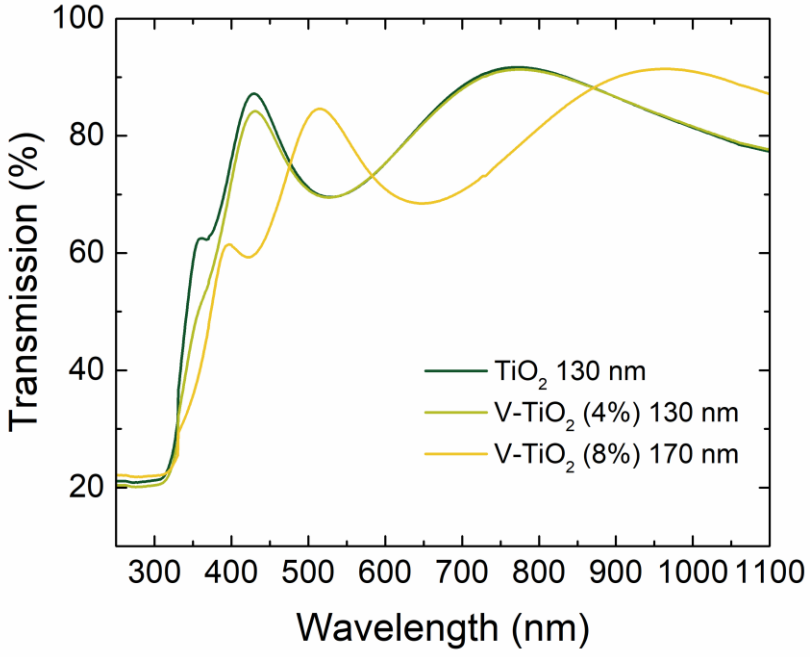

Figure 7.1: Transmission spectra of V-modified TiO_2 thin films (4% and 8%) and pure TiO_2.

As expected, transmission starts decreasing at around 400 nm, which corresponds to light absorption due to electron excitation from valence to conduction band. However, it is difficult to determine the exact band gap value from this data, since they clearly present some extra peaks that affect the whole spectrum. These peaks are due to the thin film interference effect, which is typical

of thin films with very low roughness, in which light waves reflected by the upper and lower boundaries of the film interfere with each other, either enhancing or reducing the transmitted or reflected light. In Figure 7.2 a schematic representation of the phenomenon is reported.

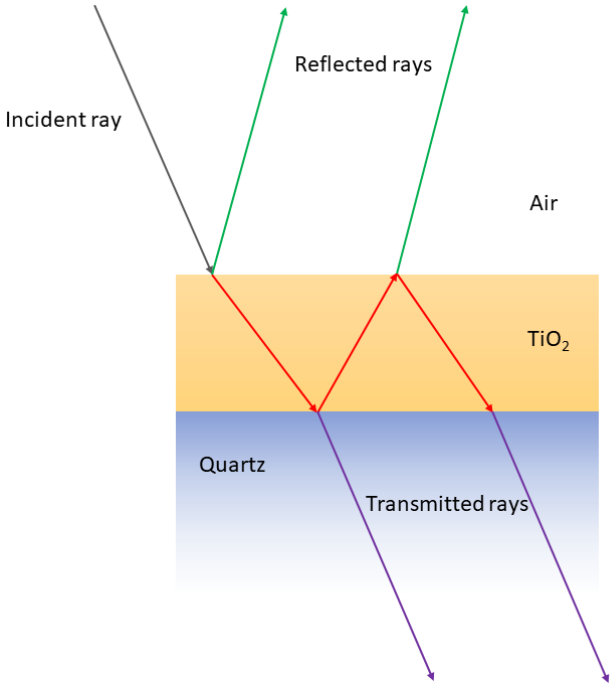

Figure 7.2: Schematic representation of thin film interference effect due to constructive and destructive interference between transmitted rays and reflected rays.

The position of these peaks depends on the film thickness and on the refractive index of the materials in which light propagates, while the intensity is related to the surface roughness (the higher is the roughness the less is the intensity of the interference pattern). It is possible to reproduce these spectra using the free code Optical,[93] that simulates experimental transmission measurements of multilayer systems in which some layers are treated as coherent, meaning that internal interference is taken into account, (TiO_2) and others as incoherent, where internal interference is ignored (quartz, since it is way thicker than TiO_2). The input structure used for the simulation is composed by two layers: the top layer (upon which the light impinges) is TiO_2 and

it was considered a coherent medium for the propagation of light, while the bottom layer is quartz, 1 mm thick and incoherent. By manually changing the thickness and the roughness of the TiO_2 film, it is possible to recover the structure that best reproduces the experimental data. Results of the simulations are reported in Figure 7.3 compared with experimental data.

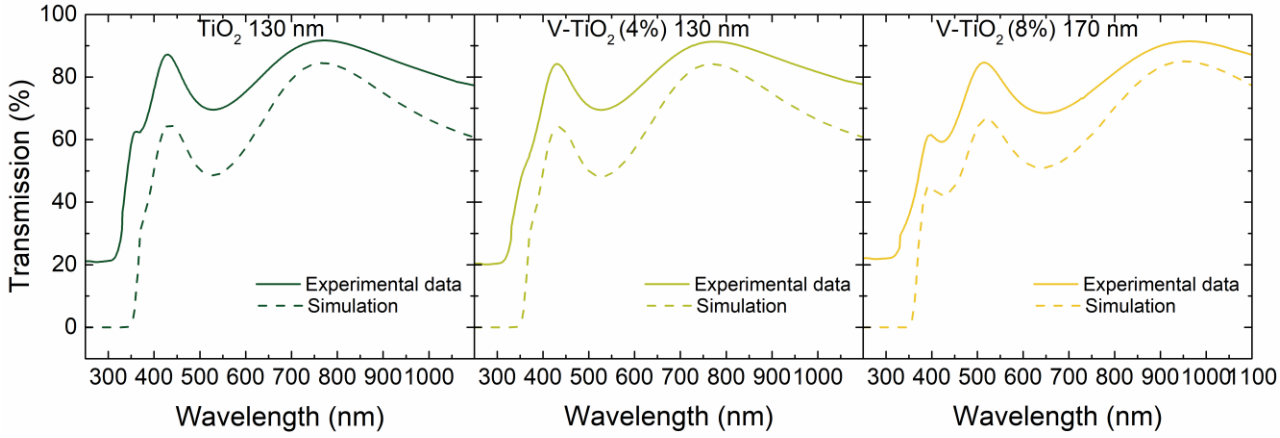

Figure 7.3: Comparison between experimental and simulated optical transmission for TiO_2 and V-TiO_2 thin films.

The values of thickness and roughness obtained by this procedure are reported in Table 7.1. The thickness obtained in this way is compatible with the nominal thickness of each sample, while the roughness is overestimated with respect to the one obtained from AFM images (3.7 ± 0.4 nm). This discrepancy could be due to several factors, such as local inhomogeneity of the illuminated surface of the sample and differences between the tabulated refractive index used for simulation with respect to the real one.

Table 7.1: Thickness and roughness obtained from the simulations of the static optical transmission spectra.

	TiO_2/V-TiO_2 (4%)	**V-TiO_2 (8%)**
Thickness (nm)	135	170
Roughness (nm)	12	15

7.1 Transient absorbance spectroscopy

Fast transient absorbance spectroscopy is a very powerful method, which can help to correlate the photoelectrocatalytic efficiency to the charge carrier dynamics; it can exhibit very high temporal resolution (down to tens of femtoseconds) and can separately probe the transient dynamics of electrons and holes, thanks to the wide spectral range (from UV to IR).[94] The identification of transient signals due to specific charge carriers and relaxation pathways has been reported in several studies in past years.[95,96,97,98] In general, three main spectroscopic signatures are observed in TiO_2, ascribed to trapped holes (THs), trapped electrons (TEs), and free electrons (FE, as described in the Drude-Lorentz model). Schneider et al.[99] summarized the results concerning THs and electrons: the maximum of the TH signal is found in the range from 400 to 630 nm, while the maximum of the TE signal is in the range from 620 to 2500 nm. This wide ranges for the position of the maxima is due to the use of different holes or electron scavengers during the measurements. On the other hand, FE do not give rise to peaks in FTAS spectra but generate a monotonically increasing background, which extends from the visible to the IR region with a power-law dependence on the wavelength. These assignments have been recently confirmed by ab initio methods.[100] Ultrafast spectroscopy was also applied to track photoexcited charge carriers in doped TiO_2.[101,102] Ikeda et al observed a second-order kinetics due to electron-hole recombination, the rate constant of which increases with increasing dopant concentration.[102] Similarly, in TiO_2 - M - TiO_2 multilayer films (M==Co or W) Sun et al.[101] showed that doping does not change the wavelength dependence of the TA spectra but that it induces a faster decay of the spectral features.

In this work, femtosecond transient absorbance spectra were recorded at increasing delay time following excitation at three different pump wavelengths, which are λ_e= 300, corresponding to photon energy above the anatase band gap, 390 nm, with a photon energy right at the edge of the

band gap and 530 nm in the visible range. Unmodified and V-modified (4% and 8%) TiO_2 thin films deposited on quartz substrate were analyzed.

7.1.1 Pump at 300 nm

In Figure 7.4 the transient signals obtained following the excitation at 300 nm are reported. In particular, maps on the right and cuts along the wavelength axis at fixed delay time are shown. The data are the results of an average of 10 spectra for every delay time. A quick view at these maps reveals the presence of a negative signal at low wavelengths common to all samples, which is due to the band gap bleaching (in blue), while at higher wavelengths above 400 nm the signal is dominated by positive signal due to induced absorption (in red). The position of the minimum of the band gap bleaching feature is at ≈ 390 nm for TiO_2 and at ≈ 360 nm in V-TiO_2. In the longer wavelength region (λ_p > 450 nm), the line shape of FTAS spectra is quite similar to the static absorbance spectra, reported as dashed lines in Figure 7.4 a, c, e, the maxima and minima of which are due to interference effects and depend on film thickness. In other words, the FTAS spectra appear to be modulated by the interference effects also observed in static spectra. Such modulations of the FTAS spectra have been previously observed in TiO_2 films[103] and suggest that the signal is strongly affected by changes in the interference pattern brought about by a photoinduced modulation of the refractive index. Interference fringes in pump-probe optical measurements were also have been previously observed in silicon thin films for photovoltaic applications.[104] The change of the refractive index depends on the polarizability and the density of free carriers, and thus, this time-dependent signal can be interpreted as an indirect measurement of the density of free carriers. This method has been applied recently to investigate free carrier dynamics in thin films of metal halide perovskites.[105]

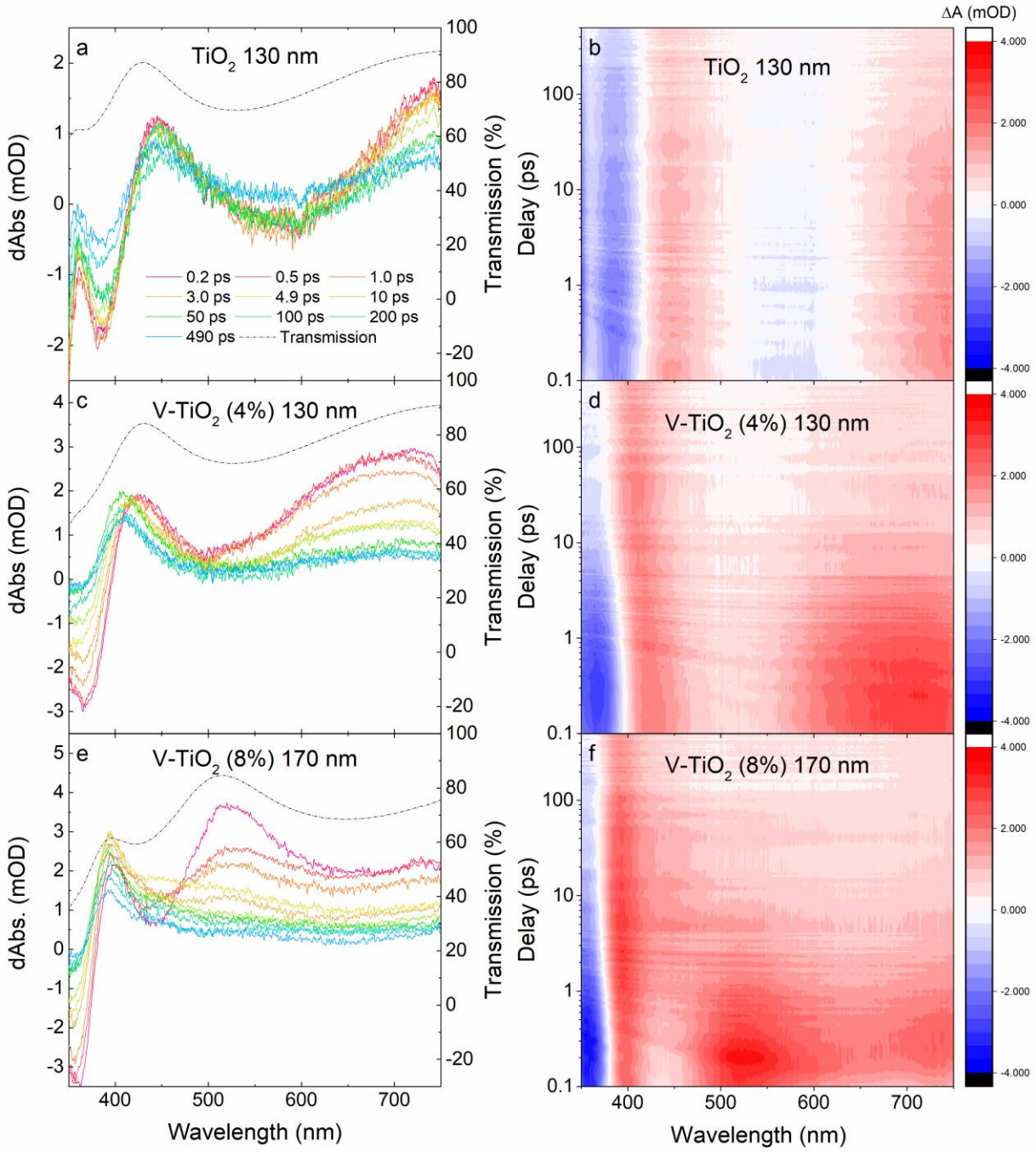

Figure 7.4: Transient differential signal calculated using equation (18) and obtained following the excitation at 300 nm. Figures b, d, f reports 2D representation of data, meanwhile figures a, c, e reports cuts along the wavelength axis at fixed delay time. In these figures, static transmission spectra are reported in dashed lines.

Even though the FTAS spectra are modulated by interference effects, the evolution as a function of time in the region λ_p > 600 nm is a representative of the dynamics of both FEs and TEs, as

amply reported and discussed in the literature.[94,99,100,103] The contribution of the FE signal increases approximately as $\lambda_p^{1.7}$, while trapped electrons usually give FTAS bands centered in the range of 600-800 nm.[95] It is not possible to separate the two contributions without performing measurements in a much wider spectral range. Therefore, in the following, I will refer to the FTAS signal at λ_p > 600 nm simply as the E signal. It is important to note that it is the FEs that contribute to the photoelectrochemical reaction because they can flow into the external circuit. The spectra reported in Figure 7.4 clearly show that the E signal decays more slowly in unmodified TiO_2 compared to that in V-TiO_2, hinting at a faster recombination dynamics induced by V incorporation; this feature will be discussed in the next section. The signature of THs, in the form of a band centered around $\lambda_p \approx 400$ nm, becomes clearly visible in the modified films at long delay times (> 50 ps) in which the amplitude of the E signal is very small. The assignment of FTAS bands centered at 400-500 nm to surface THs is well established for nanostructured TiO_2[95,99] and it is also observed in nanoparticle-assembled V-TiO_2 films, as will be shown later. In the unmodified TiO_2 film, the long-living modulated electron signal along with the photoinduced bleaching effect of the band edge tends to obscure the TH feature. The analysis of the hole dynamics and its decoupling from interference effects will be presented after the discussion of the electron dynamics. Before discussing electron and hole dynamics in detail, it is worth noticing that the presence of interference effects can explain, at least partially, the blue shift of the band gap bleaching signal (350-400 nm) induced by V incorporation. In fact, as can be seen from the dashed lines in Figure 7.4 a, c, e, the static transmission spectra themselves blue-shift, giving rise to the shift of the transient band gap bleaching feature.

7.1.2 Electron dynamics

Following the reasoning outlined above, for the analysis of the electron dynamics, the time evolution of the E signal was inspected at λ_p = 710 nm, that is, far enough from the TH band at $\lambda_p \approx$ 400 nm to exclude superposition of these features. The measured time traces, normalized to a common maximum value for the sake of comparison, are reported in Figure 7.5 a, b for the unmodified and the two V-TiO_2 films. The solid lines represent the best fits of the time traces to the sum of one exponential rise and two exponential decay functions convolved with a Gaussian-shaped IRF

$$\Delta A(t) = \sum_{i=1,2} A_i \frac{\tau_i}{2(\tau_r - \tau_i)} \left(e^{\frac{\sigma^2}{2\tau_r^2} - \frac{t}{\tau_r}}\left(1 + \mathrm{erf}\left(\frac{t}{\sqrt{2}\sigma} - \frac{\sigma}{\sqrt{2}\tau_i}\right)\right) - e^{\frac{\sigma^2}{2\tau_i^2} - \frac{t}{\tau_i}}\left(1 + \mathrm{erf}\left(\frac{t}{\sqrt{2}\sigma} - \frac{\sigma}{\sqrt{2}\tau_i}\right)\right)\right) \qquad (21)$$

in which A_i is the amplitude of the *i*th component, τ_i is the corresponding decay time, τ_r is the rise time, and σ = 30 fs is the standard deviation of the time dependent pump pulse, modelled as a Gaussian function. It is interesting to compare the temporal trend of the E signal with the recovery of the band gap bleaching, represented by the time evolution of the (negative) transient amplitude at λ_p = 360 nm, as reported in Figure 7.5 c, d. The best-fit parameters obtained for the E signal and the bleaching are summarized in Table 7.2. In both cases, the fast rise time, compared to the IRF (≈ 80 fs), is due to the effects of thermalization of the initially excited carriers. This indicates that the E signal in the first few picoseconds is mainly due to FE in the bulk because the characteristic times for electron diffusion and trapping at the surface are much longer (≈ 10 ps). V-incorporation significantly speeds up the decay of both signals, as is evident in Figure 7.5 .In particular, for the E signal, the decay time τ_1 of the fastest decaying component decreases from 51

ps in pure TiO_2 to 3.1 ps at 4% incorporation and to 1.8 at 8% incorporation. Table 7.2 shows a very good match between the τ_1 values obtained for the E signals

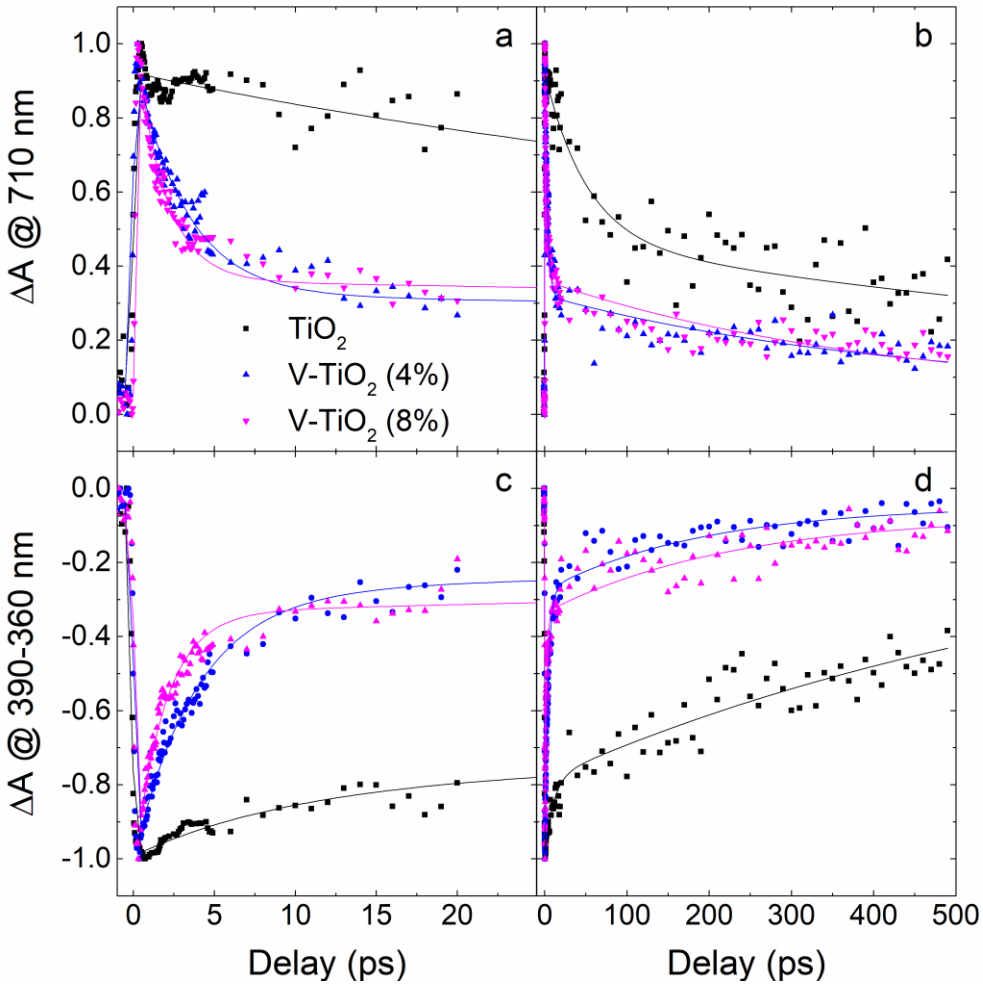

Figure 7.5: Normalized time traces following 300 nm excitation taken at λ_p = 710 nm (a, b) and λ_p = 390 − 360 nm (c,d). The solid lines display the best fit according to the double exponential function reported in equation (21). Short time delays are reported on the left and longer ones on the right.

Table 7.2: Amplitude, rise and decay time of the E (λ_p = 710 nm) and bleaching (λ_p = 390-370 nm) signals obtained from the fit with equation (21). The thickness d of the films is also reported.

	TiO_2		**V-TiO_2 (4%)**		**V-TiO_2 (8%)**	
***d* (nm)**	130 ± 5		130 ± 5		170 ± 5	
λ_p	*390 nm*	*710 nm*	*360 nm*	*710 nm*	*360 nm*	*710 nm*
A_1	-0.21(2)	0.45(0.05)	0.72(0.02)	0.66(0.02)	0.69(0.02)	0.65(0.02)

A_2	0.72(0.02)	0.40(0.06)	0.23(0.02)	0.26(0.02)	0.26(0.01)	0.32(0.01)
τ_r (fs)	83(13)	88(17)	81(10)	68(11)	69(11)	45(10)
τ_1 (ps)	10(2)	50(10)	3.9(0.2)	3.1(0.2)	1.9(0.1)	1.8(0.1)
τ_2 (ps)	720(50)	1000(400)	190(30)	420(60)	220(30)	410(40)

and bleaching signals in the case of V-modified samples. For pure TiO_2, the two values show a larger spread because of the difficulty in determining the position of the bleaching signal since it strongly overlaps with the TH band. Because the bleaching recovers via electron-hole recombination, the similar decay dynamics hints at electron-hole recombination as the dominant mechanism for the decay of the E signal. The detected dependence of τ_1 on the V incorporation level indicates that V dopants act as recombination centres. In addition, this can explain the evidence from photoelectrochemistry measurements that under UV irradiation (λ_e= 300 nm), V incorporation proves to be detrimental for photoelectrocatalysis because it accelerates the recombination of electrons generated in the bulk, reducing the probability to reach the FTO substrate and to be injected in the external circuit. The slower exponential decay of the E signal with the characteristic time τ_2 in the 100 s of the picoseconds range is usually associated with the relaxation of FEs and shallowly TEs into deep traps, which are optically inactive.[95]

7.1.3 Hole dynamics in V-modified samples

In order to decouple the electron and hole dynamics and to recover the time dependence of the TH band at short delays, in which interference effects and bleaching are quite strong, FTAS spectra were fitted as the linear combination of two components. The first one, associated with the interference-modulated E signal and the bleaching, dominates at very short time delays while t e second one is associated with the TH band at 400 nm, which becomes evident in the spectra of the V-modified films after 100 ps. Therefore, in order to represent the first component, the FTAS

spectrum $\Delta A(0.2)$ measured after 0.2 ps was selected, which minimizes the presence of the TH signal. The TH signal, with minimal distortions due to interference and bleaching, was taken as the FTAS spectrum $\Delta A(450)$ measured at a time delay of 450 ps. The temporal evolution of the TA spectra $\Delta A(t)$ was fitted as a linear combination of these two components with time-dependent coefficients $e(t)$ and $h(t)$ according to

$$\Delta A(t) = e(t) \cdot \Delta A(0.2) + h(t) \cdot \Delta A(450) \tag{22}$$

The values of the coefficients $e(t)$ and $h(t)$ were obtained through the Levenberg-Marquardt algorithm by minimizing the difference between the experimental spectrum and the linear combination as in equation (22). The outcome of this procedure is illustrated in Figure 7.6 for the FTAS spectrum at a delay time of 4.9 ps measured on V-TiO_2 (4%).

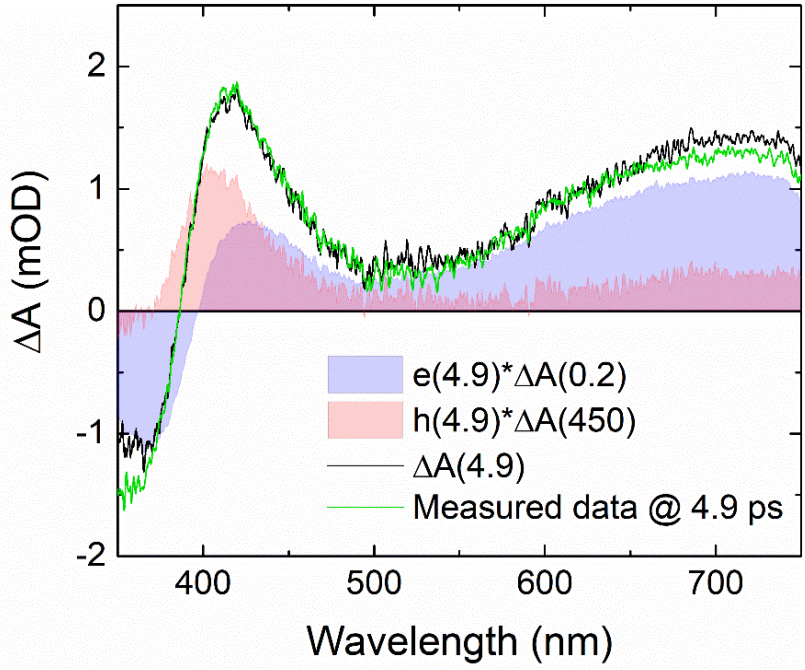

Figure 7.6: Example of the fitting procedure with equation (22) used for extracting the hole signal from sample V-TiO_2 (4%) with a delay time of 4.9 ps.

Further data of all samples and for different delay times are reported Figure 7.7.

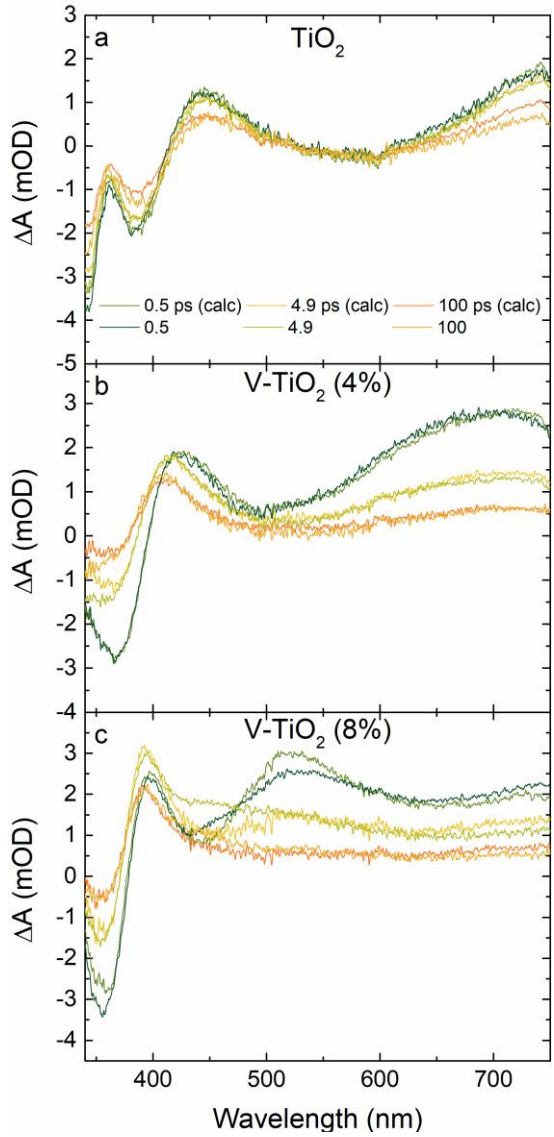

Figure 7.7: Best fits of TAS spectra using equation (21) for undoped and V-TiO_2 films. The selected delay times are indicated in panel a.

The temporal evolution of the $e(t)$ coefficient is reported in Figure 7.8. Because $e(t)$ carries a strong contribution from both the interference-modulated E signal and the bleaching signal, its time dependence is expected to be very similar to the one discussed above for the time traces at λ_p = 710 nm. This is indeed the case, as shown in Figure 7.8. In fact, by fitting $e(t)$ to the double

exponential decay function in equation (21), the decay times listed in Table 7.3 are obtained, and they are in good agreement with those of the E and bleaching signals (Table 7.2). This overall consistency supports the validity of this approach.

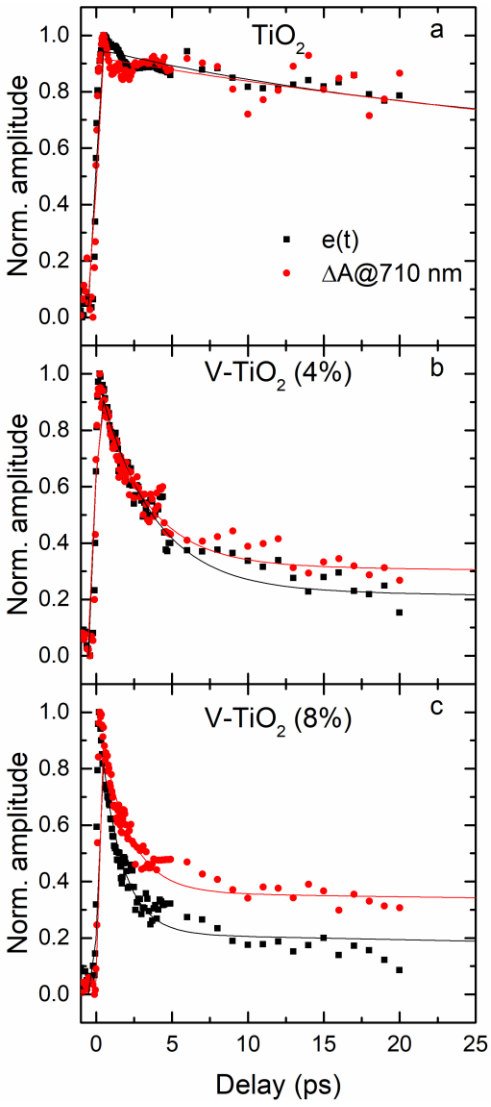

Figure 7.8: Comparison between the time dependence of the E signal @ 710 nm and the scale factor e(t), defined in equation (22) (both normalized).

Table 7.3: Decay times of the e(t) coefficient obtained with a fit using equation (21).

	TiO_2	**V-TiO_2 (4%)**	**V-TiO_2 (8%)**
A_1	0.31(0.02)	0.78(0.02)	0.81(0.02)

A_2	0.64(0.02)	0.23(0.01)	0.22(0.01)
$\tau_r\ (ps)$	0.118(0.009)	0.087(0.012)	0.064(0.012)
$\tau_1\ (ps)$	26(3)	3.5(0.2)	1.4(0.1)
$\tau_2\ (ps)$	800(60)	340(40)	180(20)

The temporal dynamics of THs, described by the $h(t)$ coefficient, is displayed in Figure 7.9. One can see that the TH signal rises within the first few picoseconds and then remains almost constant. The rise time τ_r can be determined by fitting $h(t)$ to an IRF, which corresponds to equation (21) without exponential decay.

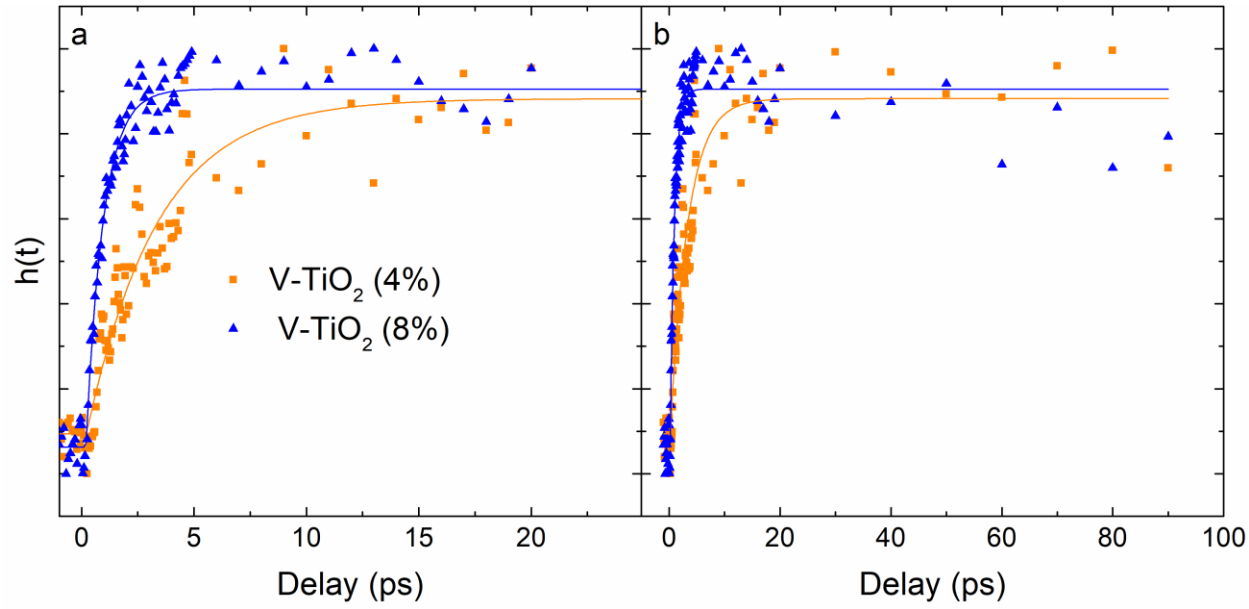

Figure 7.9: Time dependence of the h(t) coefficients with relative fits; time traces have been normalized to unity at long delay times. The plot over a longer delay interval is reported on the right.

The best-fit parameters for the amplitude and rise time of the TH signal are reported in Table 7.4.

Table 7.4: Amplitude and rise time of the TH signal obtained by fitting h(t) to equation (21) without the exponential decay. l is the mean distance travelled by holes in the time τ_r.

	V-TiO_2 (4%)	**V-TiO_2 (8%)**
A_1	0.78 ± 0.02	0.84 ± 0.02
$\tau_r\ (ps)$	3.2 ± 0.3	0.77± 0.05
$\ell\ (nm)$	11	6

The rise time of the TH signal in V-modified thin films is 3.2 ps for 4% V-incorporation and 0.77 ps for 8% V-incorporation. Considering that holes are mostly trapped in surface or subsurface sites, this difference can be ascribed to the different morphology of the systems. In fact, the mean distance traveled by holes in the time τ_r is:

$$\ell = \sqrt{D_{hole}\tau_r} \tag{23}$$

in which D_{hole} = 4 × 10^{-5} m^2/s is the hole diffusion coefficient in TiO_2[106] and ℓ is 11 and 6 nm for 4 and 8% V-incorporation, respectively, also reported in Table 7.4. These distances are much smaller than the film thicknesses (130 and 170 nm), but they are comparable to the penetration depth δ of UV radiation at λ_e = 300 nm. In fact, recalling that δ ranges between 27 and 40 nm, this limits the absorption of incoming photons, and as a consequence the generation of holes, within this distance from the surface. In addition, ℓ is similar to the hole diffusion length in single-crystal TiO_2, $\ell_{TiO_2} \approx 10$ nm.[107] In conclusion, $\ell \cong \ell_{TiO_2} < \delta$, which suggests that most holes are excited within 30-40 nm from the surface, but only those closer than 10-15 nm have a high probability to eventually reach the surface traps. A sketch of the entire process is displayed in Figure 7.10.

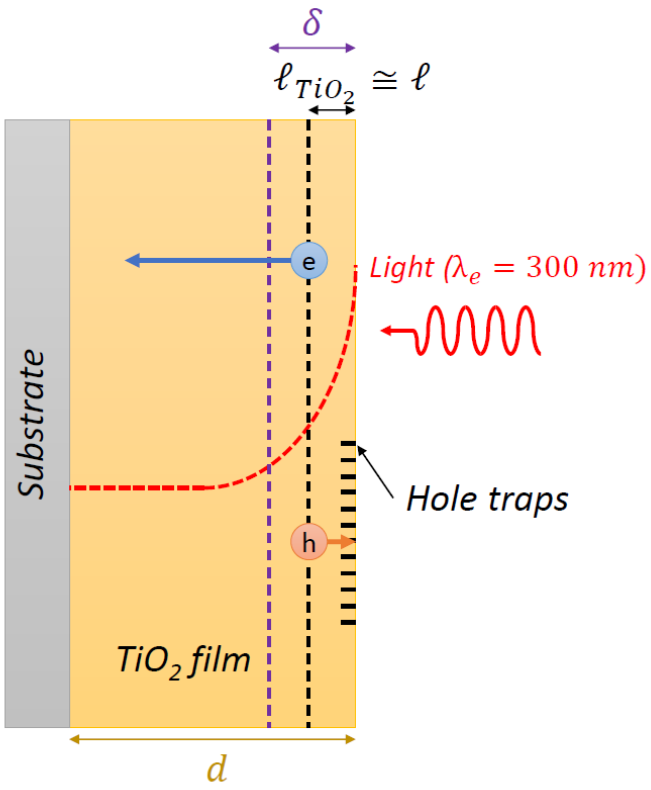

Figure 7.10: Illustration of the generation and trapping process for holes with a pump at 300 nm. The red line represents the exponentially decaying light intensity inside the film.

On the basis of this picture, it is now possible to provide an explanation of the observed results concerning the hole dynamics. The shorter distance traveled by holes in V-TiO_2 (8%) with respect to the 4% incorporation level can be correlated to the faster decay of the E signal due to recombination, as discussed previously. In other words, the accelerated recombination induced by V incorporation reduces the average distance that a free hole can travel before being trapped. On the other hand, the dynamics of surface-THs and FEs are clearly uncorrelated at long delay times: the former live without significant decay up to 100 ps (see Figure 7.9), while for the latter only 30% of the signal survives after 100 ps, further decreasing to 20% after 500 ps. This decoupling suggests that FEs mainly recombine with holes that do not contribute to the TA signal in the measured spectral range.

7.1.4 Hole dynamics: unmodified sample

The temporal dynamics of the THs signal in the case of the pure TiO_2 sample was impossible to extract because of the combination of two factors. First, the shift to higher energies of the TH absorption band in TiO_2 in comparison with that in the modified samples leads to a stronger overlap with the band gap bleaching signal. Second, the longer lifetimes of the electrons in the pure sample make it very difficult to isolate the TH absorption band at long delay times. Nonetheless, a positive contribution at 360 nm was observed at long delay times, with a stronger intensity with respect to short times, suggesting that the TH signal is located in this region in pure TiO_2.

7.1.5 Pump at 390 and 530 nm

FTAS spectra with λ_e = 390 and 530 nm are shown in Figure 7.11. At these wavelengths, since the intensity of the signal is low and the spectra are disturbed by the scattering of pump light into the detector, I will only discuss the line shape of the spectra without analyzing its dynamics. No transient signal was measured in pure TiO_2 because this sample is completely transparent at either of these pump wavelengths. This is consistent with the lack of photoelectrocatalysis for the unmodified sample in the visible range above 390 nm, as previously discussed in paragraph 6.2. Instead, it is evident from Figure 7.11 a, b that with λ_e = 390 nm, V-modified samples still show the E signal modulated by interference fringes and the long-living TH signal at 400-500 nm (the negative signals at 390 are due to the pump pulse). The intensity of the E signal with respect to the TH signal is lower than with λ_e = 300 nm. Finally, with λ_e = 530 nm (Figure 7.11 c, d), the TH signal remains clearly visible and the modulated E signal becomes barely detectable (note that in this case, the negative signals at 530 nm are due to the pump pulse). These results can be related to the photoelectrochemistry of the system. In particular, it is worth noticing that the TH signal

intensity of V-TiO_2 (8%) is about twice that found in the 4% modified film, both at λ_e = 390 and 530 nm, explaining the higher conversion efficiency of the former sample.

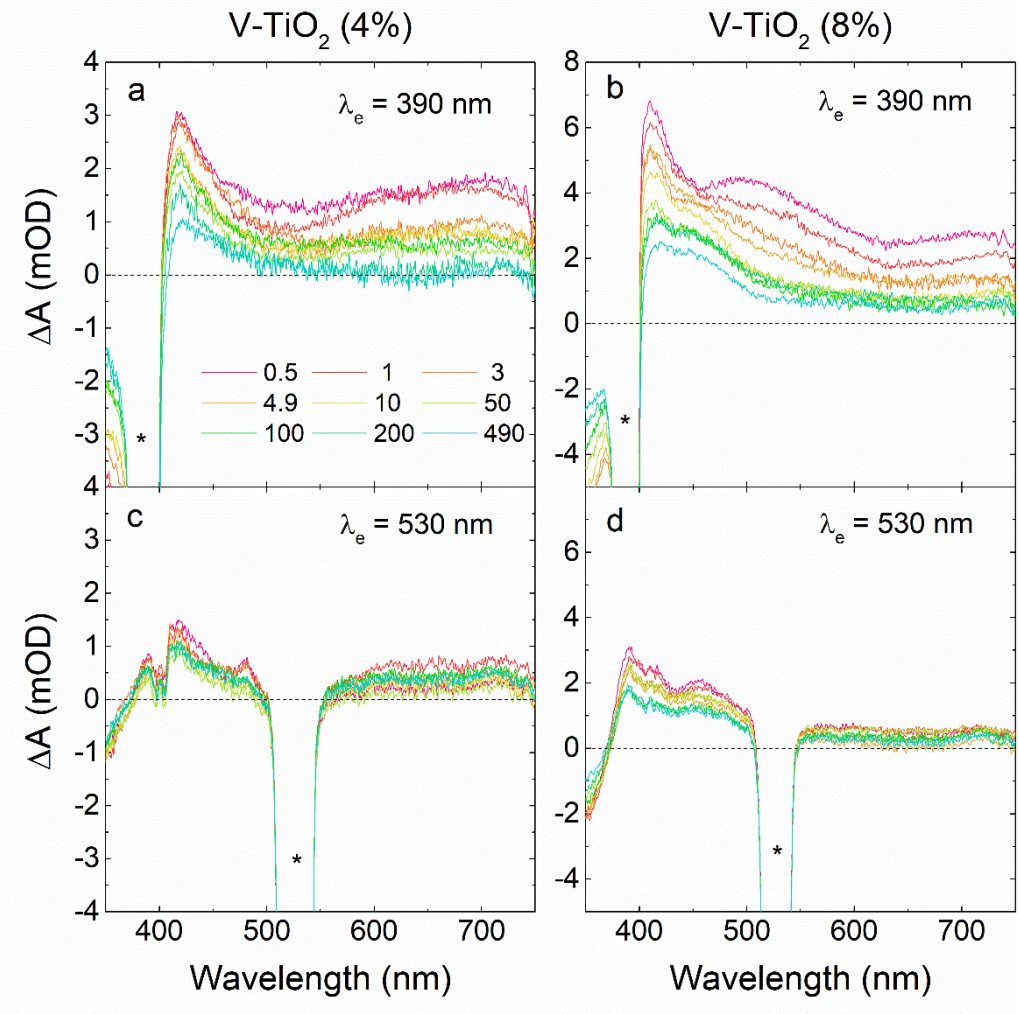

Figure 7.11: FTAS spectra of V- TiO2 4% and 8 % films with pump at 390 nm (top) and at 530 nm (bottom). Asterisks indicate the negative signal due to scattering of the pump light into detector.

The photocatalytic activity in the visible range, mentioned in the paragraph 6.2, indeed relies on the presence of charge carriers that replicate the same dynamics seen in the UV range. Recalling that the energy gap of anatase TiO_2 is equivalent to a wavelength of 390 nm, this means that it is possible to generate FEs in the conduction band (E signal) with an energy lower than the energy gap, down to at least 2.3 eV (= 530 nm). Recalling the paper by Umebayashi et al.[77], a possible

explanation of the origin of these electrons is creation of donor sites within the band gap of TiO_2 due to the introduction of substitutional V. Photoelectrochemistry measurements show a photocatalytic activity that extends up to ≈550 nm, implying that V levels are located at ≈ 2.2 eV below the bottom of the conduction band, below the position calculated by Umebayashi (around 0.5 eV below the bottom of the conduction band). The same conclusion can be derived from the results reported in the next paragraph about V-modified TiO_2 NPs based photoanodes.

7.2 A comparison between V-modified TiO_2 NPs and thin films

As I already mentioned, in the first part of my PhD course, I focused on the preparation and photoelectrochemical characterization of TiO_2 and V-TiO_2 NPs-based photoanodes. These samples were prepared by gas phase condensation using the procedure reported in paragraph 3.1.1. XRD analysis performed on these sample indicates that TiO_2 and V-TiO_2 NPs had a similar phase composition with about 75 wt% rutile, 15 wt% anatase, and 5 wt% brookite. The average size of the NPs was evaluated using a transmission electron microscope and it is 12 ± 1 nm. The V content estimated by EDS was 3.0 ± 0.5 at.%. As reported in paragraph 5.5, these sample were the object of a detailed study based on XANES and EXAFS, which pointed out the substitutional nature of V inside the TiO_2 matrix.[75]

7.2.1 IPCE measurements

For the realization of the photoanodes, 10 mg of NPs were dispersed in 0.2 ml of a 1/1 distilled water/acetylacetone solution. The resulting paste was uniformly distributed by sliding a glass rod onto a glass substrate coated by a 100 nm thick layer of indium tin oxide (ITO glass). The ITO glass was previously treated with an acidic solution to make its surface more hydrophilic and to

avoid the presence of areas uncoated by the NPs. Finally, the photoanodes were annealed at 400 °C in air for 2 h. The final thickness of the NPs layer on ITO was 1 μm.

The IPCE performed on these photoanodes are reported in Figure 7.12, which has to be compared with Figure 6.2.

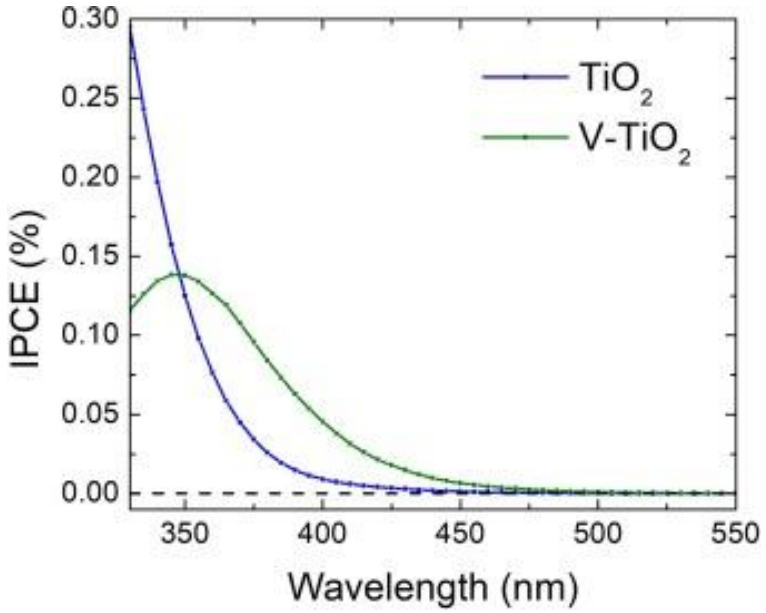

Figure 7.12: IPCE spectra of photoanodes prepared with TiO_2 and V-TiO_2 (3%) NPs.

The low IPCE values for both samples are likely due to the poor ohmic contact achieved with the preparation method. However, the interesting part is the spectral response. Like for thin film based photoanodes, the V-modified sample presents a photoelectrocatalityc activity in the visible range that is not present in the unmodified sample. In addition, following the perfect correspondence with thin films, V-TiO_2 NPs exhibit a lower IPCE in the UV range. As I will report below, this behavior is supported by FTAS measurements, that show how V introduction speeds up the recombination of charges, acting in the same way as in thin films.

7.2.2 Charge carriers dynamics: UV range

Charge dynamics in V-modified NPs was investigated using the same experimental setup used for thin films. The pump pulses were tuned at $\lambda_e = 330$ nm for studying the response in the UV range, then at $\lambda_e = 400$ nm, which is at the edge of the band gap and finally at $\lambda_e = 530$ nm for investigating the response under visible light. The identification of time traces with different charge carriers was based on the same studies reported for thin films (see reference[99] for a general overview), meaning that TH signals were located at $\lambda_p \approx 400$ nm and E signals at $\lambda_p \approx 730$ nm. The fitting analysis was carried out using different functions with respect to the one adopted for thin films. In particular, a sum of a function for second order kinetics, which describes the fast decay in the first tens of ps,[108] and a slow exponential decay was used:

$$A(t) = \frac{A_{2nd}}{kCt + 1} + A_{exp} e^{-t/\tau_e} \tag{24}$$

Despite the different approach with respect to thin films, a comparison is still possible, because a one-to-one correlation can be made between characteristic times obtained by the two procedures. In Figure 7.13 the meaning of the symbols which are going to be used is reported.

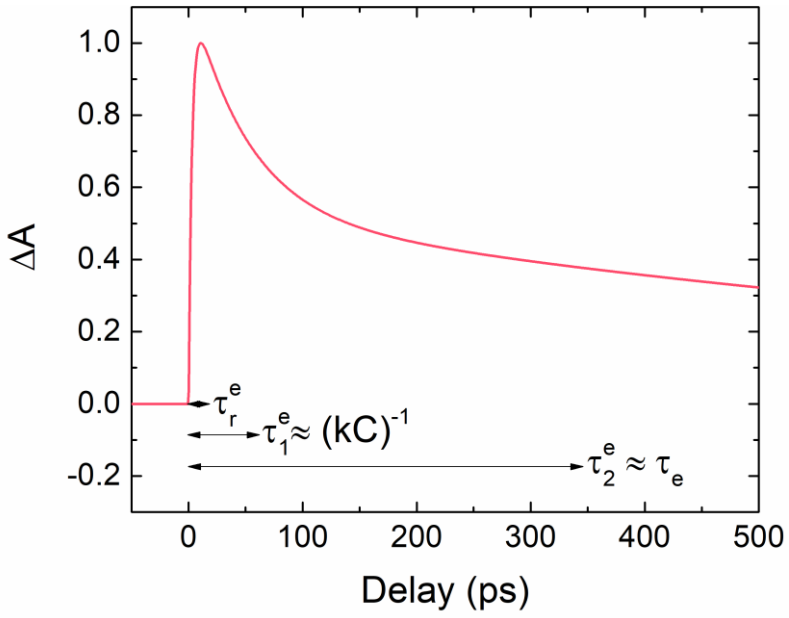

Figure 7.13: Characteristic parameters of electron time traces: τ_r^e refers to the rise time of the transient signal, τ_1^e refers to the decay time at short delay time (<100 ps) and τ_2^e refers to the decay time at long delay time.

For TH dynamics, the time trace was fitted to a sum of two exponentials, one for fast decay (here reported as τ_1^h) and the other for slower one (τ_2^h). In this case, since in thin films TH time traces were considered almost constant after the first rise and within 500 ps, there is an insufficient number of parameters to compare reliably, and in Table 7.5, in which the values of the characteristic times for thin films and NPs are compared, this is indicated with "no decay within 100 ps".

Table 7.5: Comparison between the main parameters of the time traces of thin films and NPs after pumping in the UV range (300-330nm).

		Thin films		**NPs**	
		TiO_2	V-TiO_2 (4%)	TiO_2	V-TiO_2 (3%)
$\boldsymbol{\lambda_e \approx 300\ nm}$	$\tau_r^e\ (fs)$	88	68	80	80
	$\tau_1^e\ (ps)$	50	3.1	1.8	0.6
	$\tau_2^e\ (ps)$	1000	420	210	220

	$\tau_r^h\ (fs)$	/	3200	230	230
	$\tau_1^h\ (ps)$	/	No decay within	No decay	36
	$\tau_2^h\ (ps)$	/	100 ps	within 500 ps	1030

Starting the comparison from the rise time τ_r^e of the electron signal at around $\lambda_p = 700$ nm, it can be noticed that is similar in NPs and thin films and comparable with the time resolution of the instrument; this means that the origin of this signal, which is the photoexcitation from the valence band to the conduction band of FEs in the bulk, is the same in both systems. For what concerns the decay time τ_1^e, this is in general different between thin films and NPs, but the introduction of V significantly speeds up the decay of the E signal in both cases. The decay time τ_2^e, associated with the relaxation time of FEs and shallowly trapped electrons into deep traps which are optical inactive[106], is larger for thin films with respect to NPs but still in the other of hundreds of ps. So far, it is possible to conclude that the electron dynamics in TiO_2 is the same in thin film and NPs and that V-introduction increases the recombination probability in both cases under UV light.

Holes dynamics, on the other hand, presents a significative difference in the rise time τ_r^h of the TH signal; in fact, in NPs τ_r^h is much shorter than in thin films. This is due to the proximity of the nanoparticle surface to the generation site of holes, assuming to be at the center of the NPs, that is ≈ 5 nm from the surface, meanwhile, for thin films, this distance was estimated using Eq. (20) and it is ≈ 10 nm (see Table 7.4). Passing to the dynamics at higher delay time, a direct comparison between the two systems is difficult, due to the lack of the corresponding parameters for thin films.. It worth noticing that, in NPs, the introduction of V reduces the lifetime of TH, passing from the absence of a decay in unmodified TiO_2 to a finite one (see τ_1^h and τ_2^h), but still remaining much higher than τ_1^e and τ_2^e. In thin films no decay was observed in V-modified sample up to 100 ps. As a consequence, the decoupling behavior between E and TH in thin films

(mentioned at the end of the paragraph 7.1.3), remains only partially present in NPs, since V introduction induces the recombination of surface THs with FEs (still available in this time interval), whereas the long time τ_2^h = 1030 ps can be ascribed to slower recombination with deeply trapped electrons. Again, this difference can be attributed to the morphology of the system: in NPs FEs and THs are confined in a small volume and the probability of recombination is higher than in thin films, where a bigger volume is available for the spatial separation of the two charge carriers.

7.2.3 Pump at 400 nm and in visible range

In NPs-based sample, TAS measurements after the excitation with 400 nm reveal a behavior similar to the one upon UV excitation. The TH features is not observable since it overlaps with the pump beam, while the remaining part of the spectrum are qualitatively similar to those observed for ultrabandgap excitation. This means that V still speeds up the decay of the E signal. The only main difference between unmodified and V-modified samples is the intensity of the E transient signal, which is higher in the modified sample. This is consistent with the higher IPCE at 400 nm reported in Figure 7.12. With thin films sample, no signal was detected at this pump wavelength in the unmodified thin film. However, in V-modified thin films, the overall spectral response was qualitative similar to the case of UV excitation, like in the case of NPs.

Finally, for excitation at 530 nm, no signal was detected for unmodified NPs (as for thin films) and only a weak long living E signal characterize the spectrum of V-modified NPs. This is in full agreement with data from thin films.

7.3 Location of V energy states inside TiO_2

The comparison between photoelectrotalytic performance of thin film and NPs-based sample revealed that the two systems present a very similar charge dynamics in the UV and visible spectral regions . The only differences can be attributed to the morphology of the two systems, as expected. In both cases the introduction of substitutional V in TiO_2 modifies the transient optical absorption and photoelectrocatalytic activity. Femtosecond transient absorbance spectroscopy provided the basis to interpret the results of the photoelectrochemistry measurements. In particular, the introduction of vanadium allows TiO_2 to exhibit water-splitting activity in the visible spectral region in which it is normally inactive; on the other hand, it negatively affects the energy conversion performance in the UV range. Light absorption and charge transport are the upstream processes of photoelectrocatalysis, and in fact, they undergo significant alterations because of vanadium incorporation. In particular, it was found that:

- Light absorption is extended from UV (390 nm, the band gap of anatase TiO_2) up to ≈530 nm in the visible range, as shown by the presence of a TA signal after excitation at 530 nm. This is most probably related to the introduction of donor levels associated with V sites inside the TiO_2 energy gap. From these occupied intragap states, electrons can be photoexcited in the conduction band even upon subband gap irradiation. By comparing photoelectrochemistry and TA measurements, a reasonable upper limit for the distribution of V energy levels within the TiO_2 energy gap can be set at ≈ 2.2 eV below the bottom of the conduction band.
- Charge dynamics is influenced by V as well. It was found that V accelerates electron-hole recombination in the modified samples upon UV irradiation. This side effect is probably responsible for decreasing considerably the conversion efficiency in this spectral range.

- Photoelectrocatalysis in the visible range is related to FEs and THs coming from V donor sites in the TiO_2 energy gap. In particular, the holes produced by visible light absorption on V sites migrate to the semiconductor-electrolyte interface where they are captured by long-lived traps and eventually promote water oxidation under visible light.
- The dynamics of TH and E suggests that there is no recombination between FEs in the bulk and THs on the surface because they live much more than electrons.

Based on the results obtained here, a pictorial representation of the processes is reported graphically in Figure 7.14.

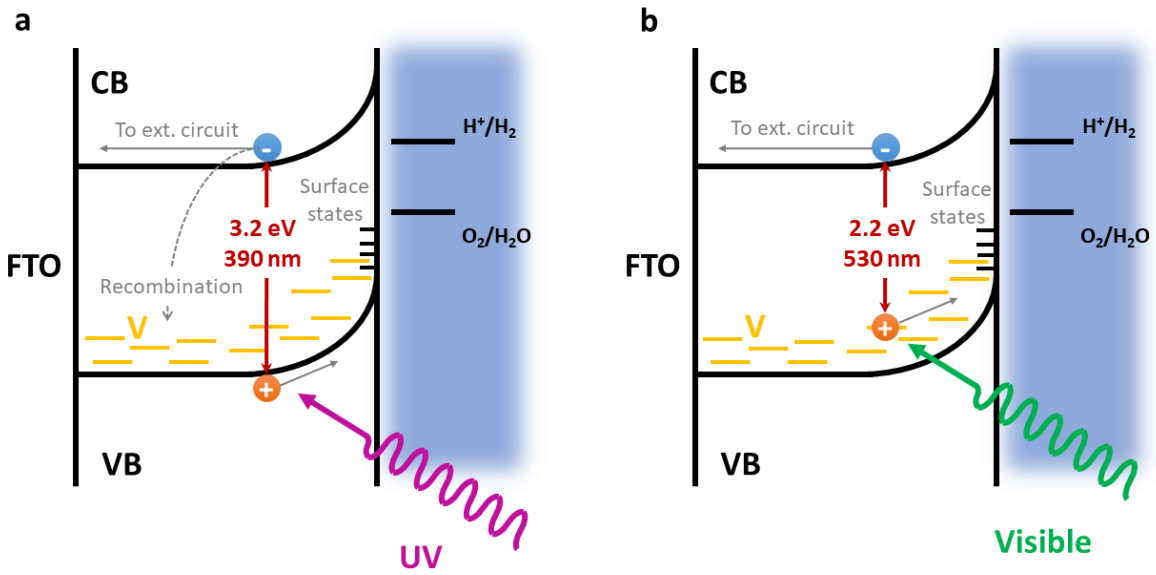

Figure 7.14:Representation of the dynamics of electrons and holes in V modified TiO_2 upon UV (a) and visible (b) light.

CONCLUSIONS

In this thesis, the correlation between conversion efficiency of light into chemical energy and charge transport in V-modified TiO_2 sample was studied. In the first part of the work, samples were prepared using two different technique: RF magnetron sputtering for thin films and GPC for NPs. By means of XRD, XPS, Raman spectroscopy and AFM, it has been shown that V does not induce critical distortion in the TiO_2 crystal structure. In addition, XANES revealed that the local environment of V and Ti inside the TiO_2 matrix is similar, aiming that V substitutional either in thin films and in NPs.

In the second part, the combination of ultrafast optical spectroscopy and photoelectrochemical methods was adopted for studying the charge carrier dynamics of the systems upon UV and visible light. In particular, IPCE revealed that the introduction of V in TiO_2 increases its conversion efficiency in the visible range of solar spectrum, up to 530 nm, an energy range in which pure TiO_2 is inactive. At the same time, V turned out to be detrimental under UV light, since V-modified TiO_2 presents a lower photoelectrocatalytic activity with respect to unmodified samples. This scenario was confirmed by FTAS measurements, performed at three different pump wavelengths (300, 390 and 530 nm) showing that under UV light V speeds up the recombination of FEs excited in the conduction band, explaining why photocurrent in this range is lower for modified samples. On the other hand, V allows the absorption of visible light with energy below the energy gap of TiO_2, producing electrons and holes with enough energy to trigger the water-splitting reaction. The new photoelectrocatalytic activity in the visible range is attributed to the presence of intragap levels at ≈ 2.2 eV below the bottom of the conduction band, caused by the introduction of substitutional V. This was confirmed by long-living transient signals due to

photoexcited charge carriers. In particular, FEs electrons are photoexcited into the conduction band after visible light (530 nm) pulses and injected in the external circuit, meanwhile the remaining holes migrate to the semiconductor-electrolyte interface where they are captured by long-lived traps and eventually promote water oxidation under visible light.

A step forward in this study is the realization of time resolved XES and XAS for tracking charge exchange between V and Ti, as reported in the APPENDIX A. The set of techniques adopted for this thesis work can be adopted for the study of other promising oxide semiconductor, such as $BiVO_4$, WO_3 and modified Fe_2O_3 for photoelectrocatalytic applications.

APPENDIX A: PUMP PROBE XES MEASUREMENTS ON V-MODIFIED TIO_2 THIN FILMS (FEASIBILITY STUDY)

During my stay at the SwissFEL I worked on a preliminary study for femtosecond pump-probe X-ray spectroscopy on solid samples, such as TiO_2 thin films used in this thesis. I collaborated with the group of the Alvra beamline, which is specialized in measuring ultrafast dynamics of photochemical and photobiological systems using a variety of X-ray scattering and spectroscopic techniques, including serial femtosecond crystallography (SFX), X-ray absorption and emission spectroscopy and inelastic X-ray scattering (IXS). The aim of this study was to evaluate all the main parameters required for performing a fs pump-probe experiment with FEL pulses as probe and optical laser as pump, such as the geometry of the set up in relation with the incoming X-ray and optical beam, and the design of a suitable sample holder. Unfortunately, due to the covid-19 pandemic, it has been impossible to perform a complete set of test measurements on my sample and no major results were obtained; only a damage test was carried out, without the use of the pump laser.

A 1 Experimental station Alvra

The layout of the experimental station Alvra (ESA) is shown in Figure A 1. This experimental station is focused mainly on two techniques: SFX and X-ray spectroscopy. Thanks to its variable-gap ondulators, SwissFEL is particularly suited for this kind of measurements, since these allow to easily scan the X-ray energy of the XFEL over a very wide range, allowing techniques such as XANES and EXAFS to be used. ESA has the additional capability of performing X-ray emission spectroscopy which uses X-ray diffraction from a crystal analyzer to measure the scattered or fluorescence X-ray photons with high energy resolution. ESA uses short focal length crystals (25

cm) in a dispersive von Hamos geometry to measure a range of XES energies in a single measurement.

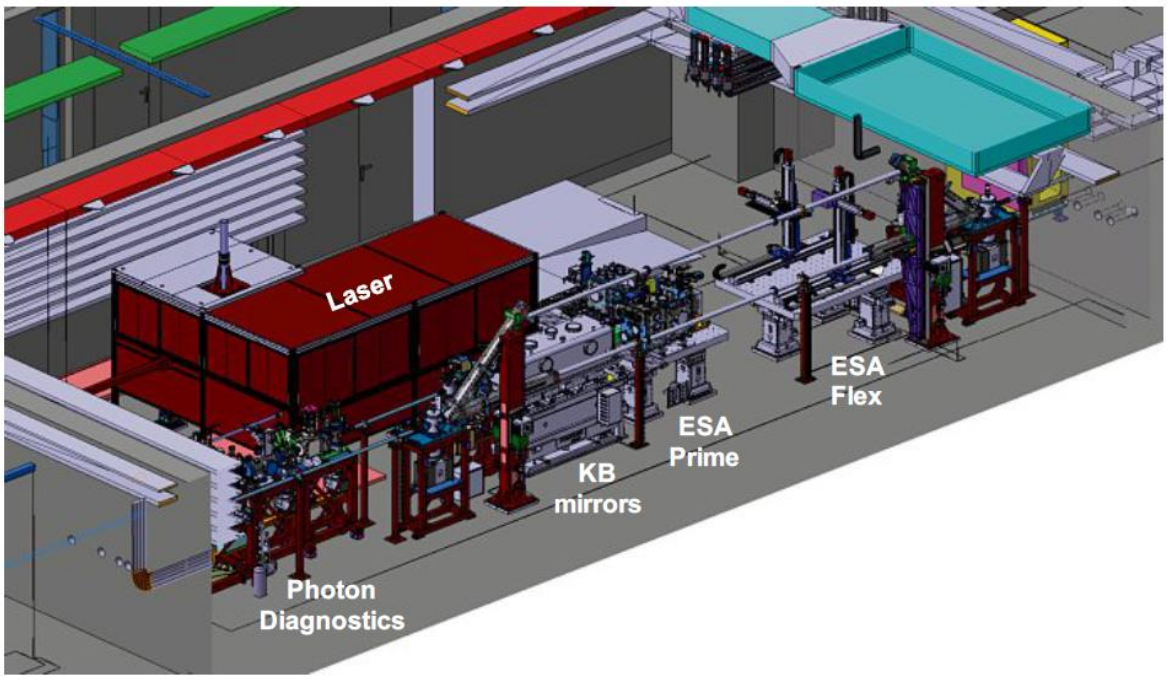

Figure A 1: Layout of ESA showing the location of the various elements within the hutch. The X-rays go through the hutch from left to right.[60]

This spectrometer can also be used for a variety of other scattering measurements including off-resonant techniques and inelastic X-ray scattering (IXS). These techniques are applied to two instruments, which are located in line with the X-ray beam: ESA Prime and ESA Flex. Thanks to the flexible KB (Kirkpatrick-Baez) mirrors the X-rays can be focused at either instrument, with the minimum focus of 1.5 µm achieved at ESA Prime. Additionally, both instruments can be used with the optical laser for pump-probe experiments, with a time resolution around 50 fs. ESA Prime has a chamber that can be operated under vacuum, He, or neutral atmosphere and combines a large 2D Jungfrau detector and a dual-crystal von Hamos X-ray emission spectrometer. This allows experiments to be performed using both scattering and emission techniques simultaneously. ESA

Flex is a flexible instrument that allows users to build up their experiment as required. It is mounted on a motorized table, allowing user to use their own. ESA Flex also includes a configurable X-ray spectrometer that can be mounted in a variety of positions to measure a range of scattering angles, in both vertical and horizontal geometries.[60] Both instruments are shown in Figure A 2.

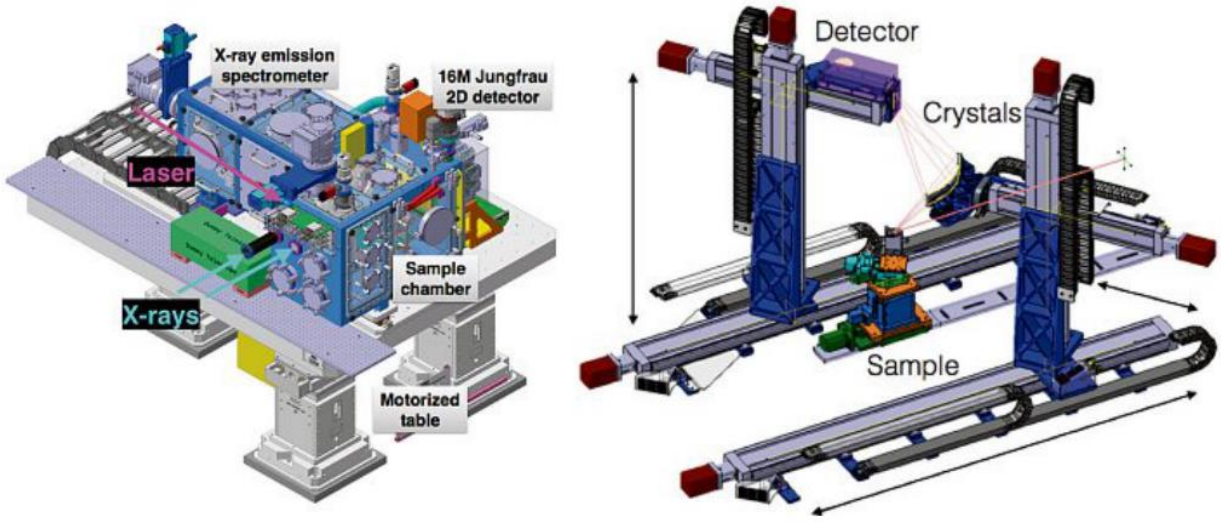

Figure A 2: 3D sketch of the two instruments available at ESA. Left: ESA Prime, right: ESA Flex.[60]

A 2 Preliminary study of the experiment

The aim of the experiment is to exploit the sub-ps time resolution of pump-probe XES and XANES available at the Alvra beamline to study the element-specific photoexcitation pathways in V-modified TiO_2 thin films. More specifically, the goal is to determine whether the ultrafast optical response is associated to charge transfer between dopant (V) and matrix (Ti), as suggested by Rossi et al.[109] in a study performed with differential RIXS spectroscopy using the ID26 beamline of the ESRF in Grenoble, France, and the work reported here on ultrafast transient optical spectroscopy. In order to set up this measurement, I addressed the main experimental issues of a fs pump-probe experiment with FEL pulses as probe and optical laser as pump, such as the geometry of the set up

in relation with the incoming X-ray and optical beam, and the design of a suitable sample holder. The X-ray and optical laser pulses parameters, such as power and spot size have been estimated in order to fulfill all the experimental requirements.

A 3 Description of the experimental part

In Table A 1, the main experimental parameters for these measurements are reported.

Table A 1: Experimental conditions and parameters for time resolved X-ray spectroscopy on V-modified TiO2 thin films.

X-Ray energies	**For XES:** V and Ti K_β at 5.4 and 4.9 KeV, respectively. Resolution 0.1 - 0.2 eV. **For XANES:** V and Ti K_α, similar energies, resolution less stringent.
X-Ray energy range	From 4.9 to 8 KeV
X-Ray focus size	$100 \times 100\ \mu m^2$
Laser wavelength	400 nm
Laser pulse energy	10 mJ
Laser spot size	$200 \times 200\ \mu m^2$

The idea is to perform a pump and probe time resolved XES/XANES experiment using the available laser at 400 nm as a pump and the von Hamos spectrometer to record spectra of the V K_β and Ti K_β emission lines. The choice of a 400 nm laser as pump, being slightly below the energy gap of TiO_2, is crucial to assure that only V-induced gap states are excited. The K_β emission lines are well known to exhibit a shift and a line shape change depending on the oxidation state (~1 eV per unit change of the oxidation state); therefore, it is expected that charge transfer induced by light absorption will predominantly lead to an energy shift of the K_β emission lines of the order of 1 - 2 eV. Pump-probe measurements are performed by varying the time delay between laser pump and X-ray probe with steps of 0.5 ps in the range 0 - 10 ps. The possibility to detect a time

dependent XES signal pump-probe mode using the available experimental conditions is supported by the following reasons:

- TA optical measurements were performed with an intensity of about 1 mJ/cm^2 with 5 μJ pump pulse, intensities which are available at Alvra.
- The successful differential HERFD-XANES experiments at ID26 ESRF were performed with a low power 200 mW continuous wave laser diode, resulting in 20% x-ray excited state fractions for V.[109] The Alvra pulsed laser system provides several orders of magnitude higher power, implying that all V atoms will be excited, maximizing the X-ray spectral contrast.

A 3.1 Setup geometry

ESA has two collinear end stations, called PRIME and FLEX (Figure A 2). In principle, both PRIME and FLEX end stations are suitable for solid sample spectroscopy measurements. The geometry of the Alvra PRIME end station is shown in .

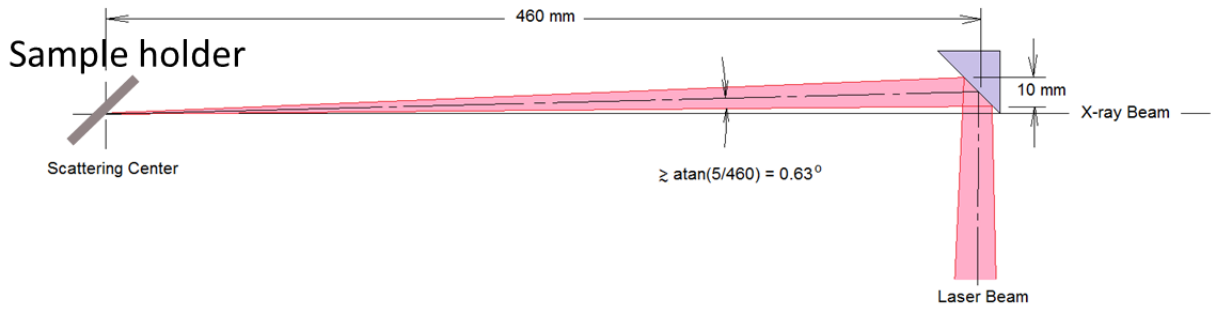

Figure A 3: Setup geometry of the Alvra PRIME end station.

The geometry of the experiment in Alvra FLEX is more flexible than Alvra PRIME, thanks to motorized stage and arms that keep the analyzer and the detector; however, the X-ray probe and the visible pump come from the same direction as in PRIME. Taking into account the average size

of the X-ray spot in PRIME, which is 20 μm of diameter, the trend of the footprint area of the X-ray on the surface of the sample as a function of the incident angle between the X-ray beam and the sample surface is reported in Figure A 4.

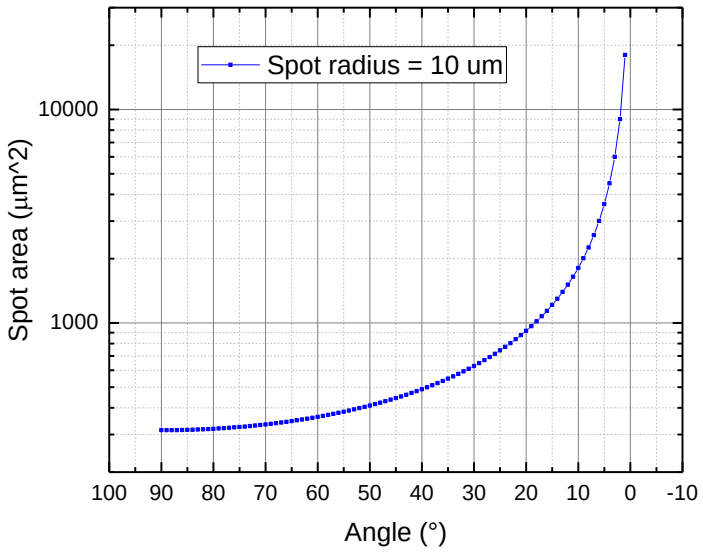

Figure A 4: X-ray spot area on the sample surface in function of the incident angle (PRIME end station).

In Alvra FLEX the X-ray beam can be focused down to 100 μm and the trend of the X-ray spot area on the surface of the sample is reported in Figure A 5.

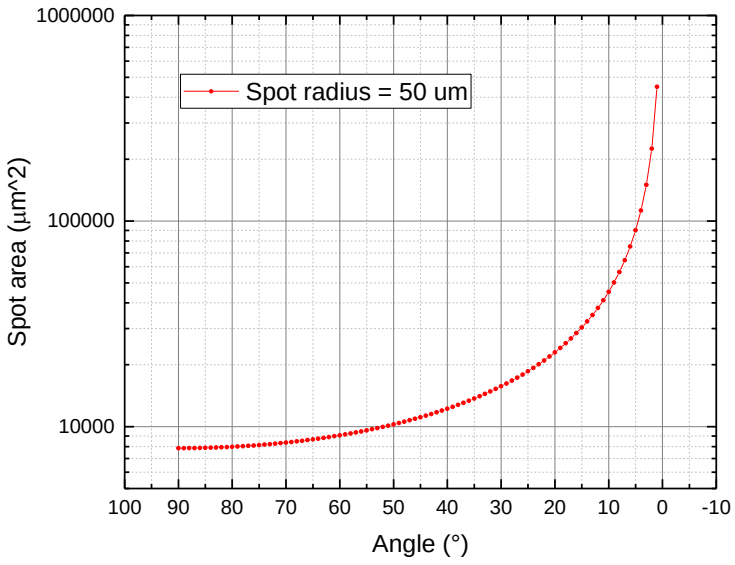

Figure A 5: X-ray spot area on the sample surface in function of the incident angle (FLEX end station).

In Figure A 6 a sketch shows how the x-ray spot area changes from 90° to 45° incidence angle.

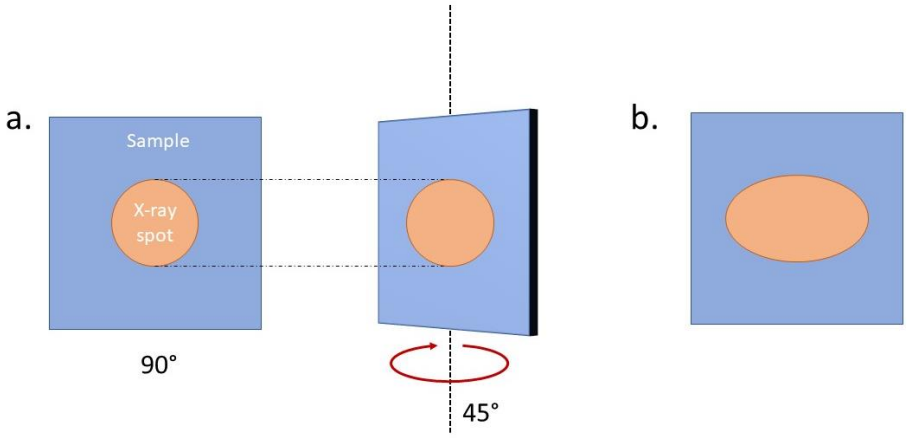

Figure A 6: X-ray spot projection on the sample surface with a 90° (a.) and 45° (b.) incident angle. The area of the X-ray spot is import for calculating the energy density deposited by FEL shots on the film surface.

Assuming a photon dose of 10^{11} photons per pulse[60], the energy density deposited by a single pulse on the sample is shown in Figure A 7 as a function of the incidence angle.

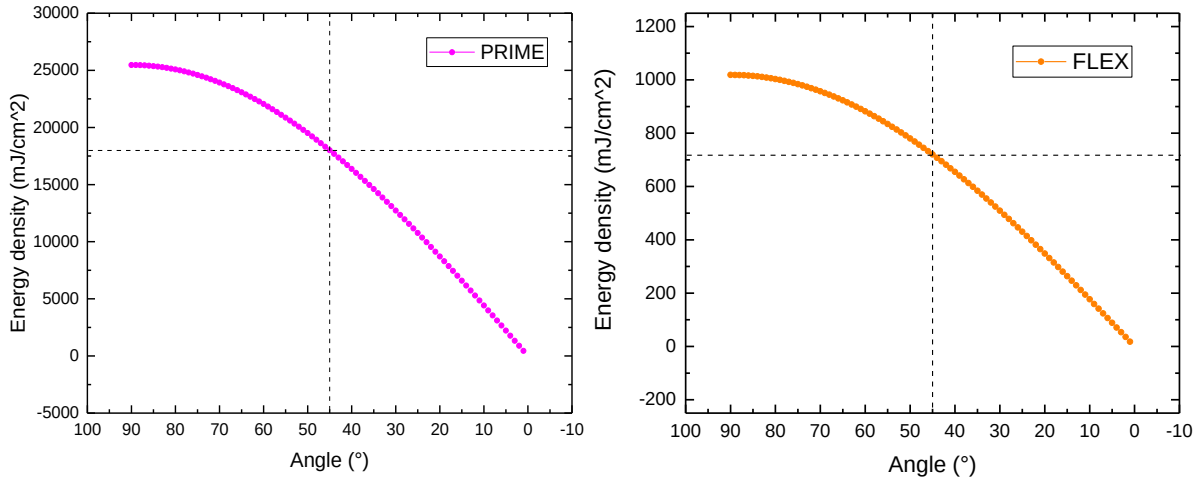

Figure A 7: Energy density deposited on the sample by a single FEL pulse at 5 KeV (PRIME left, FLEX right).

This parameter is important for the evaluation of the sample damage and the signal to noise ratio in these measurements. In fact, one of the main problems of using FEL pulses on solid sample is the damage of the sample itself. This is the reason why during measurements, the sample is moved in order to expose a new area every new run X-ray run, which is composed by several X-ray shots.

The penetration depth of the X-ray beam from the sample surface at different angles is reported in Figure A 8 (left), while the same parameter is reported at a fixed angle (45°, usually adopted) as a in function of the incident energy (Figure A 8 right).

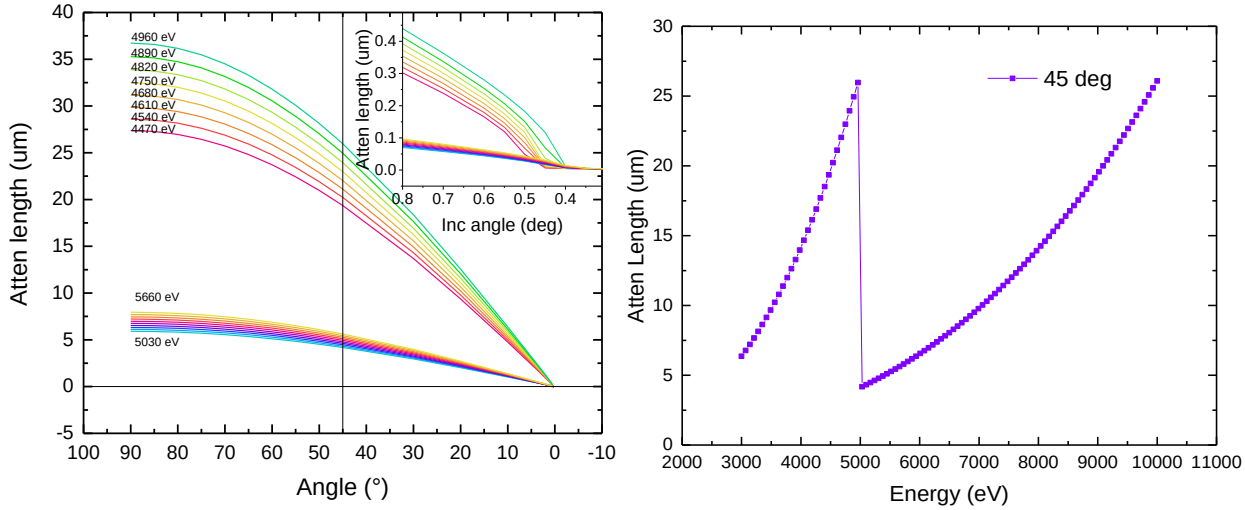

Figure A 8: Attenuation length for different x-ray energy in function of the incident angle (left) and for different incident energy at a fixed angle (right).

Since the attenuation length in the selected energy range for the experiment (of the order of a few μm) is way larger than the film thickness (a few nm), the X-ray beam probes all the sample up to the substrate.

A 3.2 Pump laser

In pump probe measurements it is crucial that the excited volume by the pump pulse is larger than the probed volume by the X-ray probe. Concerning the penetration depth of the pump laser (400 nm) in the TiO_2 sample, it is important to notice that the energy gap of this material is around 3.2 eV (anatase) which corresponds to 387 nm; as a consequence, at 400 nm the transmittance is around 60-70 % (see Figure 7.1), meaning that the film is almost transparent at this wavelength. Therefore, the interaction volume of the pump laser matches the probed volume by the X-ray pulse.

In order to excite selectively vanadium atoms over titanium atoms, the wavelength of the pump laser is tuned slightly below the band gap energy. In fact, substitutional vanadium atoms create energy levels in the energy gap of TiO_2, ~ 2.2 eV below the bottom of the conduction band and extend the absorption region towards the visible range.

A power dependence analysis performed with femtosecond transient absorbance spectroscopy, using different pump wavelengths (300 nm and 390 nm) and different fluences, is reported in Figure A 9.

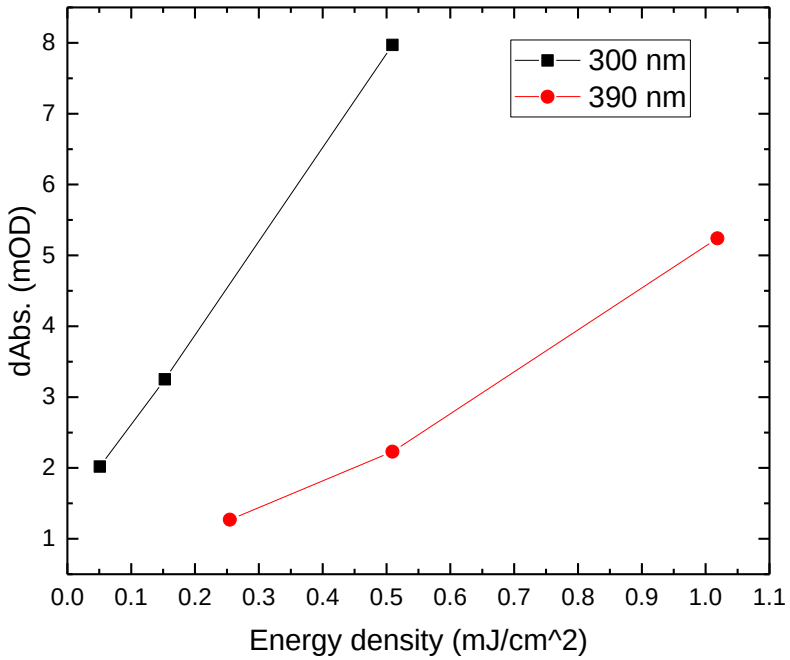

Figure A 9: Power dependence of V-modified TiO2 film at different pump wavelengths.

At both pump wavelengths the differential absorption can be considered still linear with the energy density, excluding possible further mechanism, such as two photons absorption, that can affect the measurement. The intensity and the wavelength of the pump laser are important parameters in order to evaluate the number of absorbers that are excited in the sample.

A 3.3 Sample holder

To perform these measurements, I designed a sample holder that allows both transmission and emission spectroscopy measurements (Figure A 10).

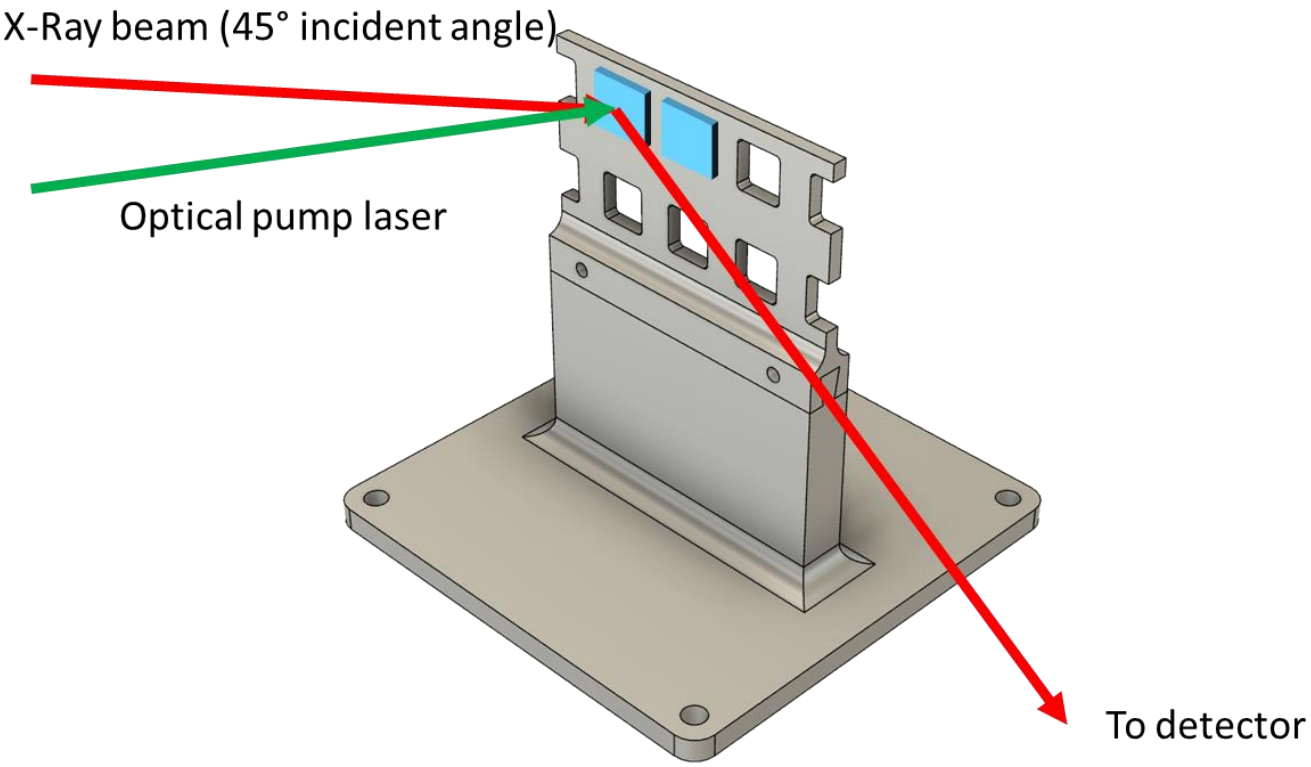

Figure A 10: Design of the the sample holder for emission and transmission X-ray spectroscopy on solid sample.

It is composed by two separable pieces; the base can be screwed on a movable stage allowing the rotation and translation with respect to the incoming X-ray beam and a plate with holes on which solid samples and reference samples can be attached with double-sided tape.

A 4 Preliminary damage test on thin film samples

A preliminary measurement test on V-modified TiO_2 solid sample thin films was performed during the commissioning time of FLEX end station. In particular, non-resonant XES at 8000 eV with analyzer crystals setup for Ti Kα (Si(220)) were adopted. No laser pump was used since the aim of these measurements was the evaluation of the damage caused by XFEL pulses on the thin film surface. The sample measured was V-TiO_2 (8%) with a thickness of 170 nm. Measurements were divided into 10 runs, each one containing 2000 FEL shots, and after every run the sample was shifted in order to expose fresh surface and reduce the damage. In Figure A 11, the signal obtained from the 2D detector after an average of 2000 shots is reported; Ti Kα_1 and Ti Kα_2 are visible on the left at the bottom.

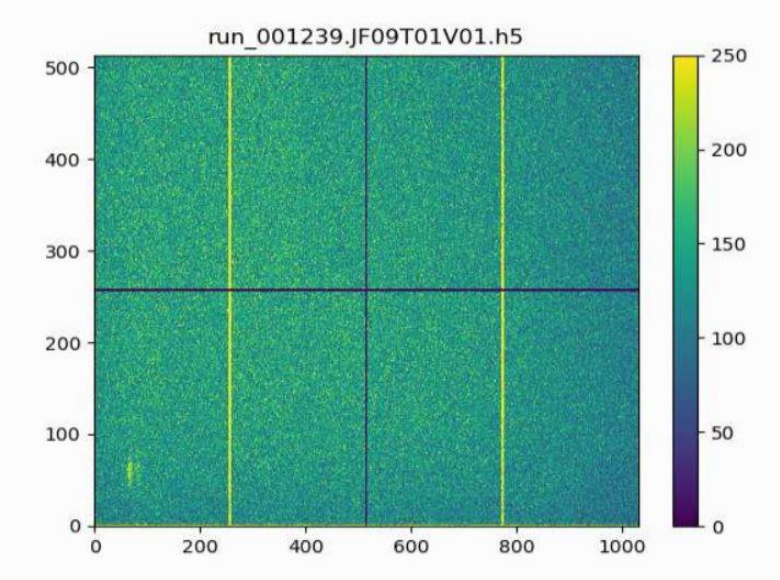

Figure A 11: Ti Ka1 and Ka2 (left, at the bottom) after the integration of 2000 FEL shots.

In order to obtain a spectrum out of this 2D image, the projection of the emission line along the dispersive axis (x axis) of the detector was performed. The result obtained after the integration of 10 runs reported in Figure A 12.

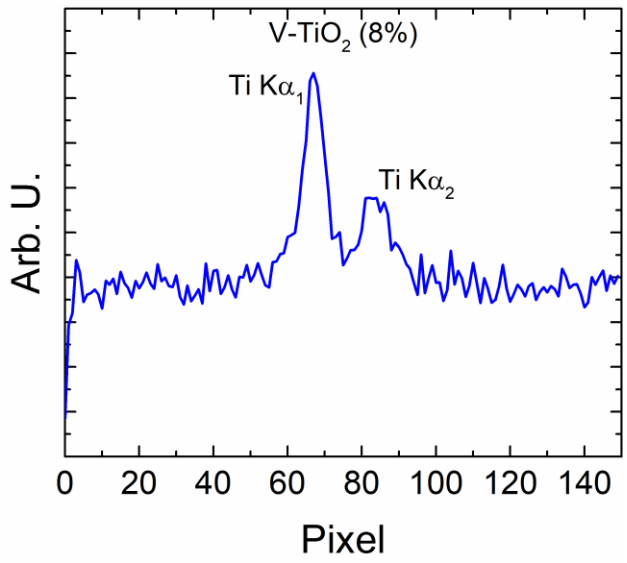

Figure A 12: Ti Ka1 and Ka2 obtained after the integration of 10 runs.

Figure A 13 shows the damage on the film surface after the exposure to FEL pulses.

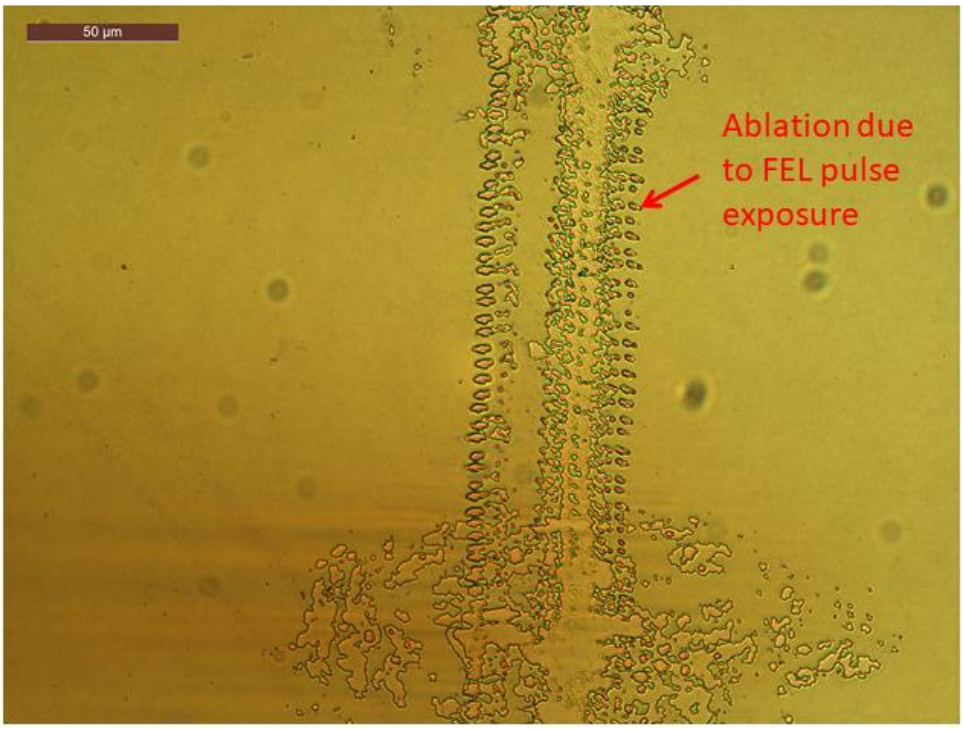

Figure A 13: Visible microscope image of the damage reported by the surface of the thin film after FEL pulses exposure.

It possible to notice the ablation of the thin film along the direction of the scan during the measurements. However, the emission signal remains still detectable after 10 runs (20000 FEL shots), meaning that, despite the surface ablation, which in general is detrimental for the detection of a good emission signal, the film is still present and not completely damaged.

ACKNOWLEDGEMENTS

I would like to conclude this thesis with my grateful thanks to all the people that supported and helped me during the last three years. First of all, I express my special thanks to Professor Federico Boscherini, who patiently introduced me to the world of the scientific research, teaching me how to develop a rigorous scientific method for achieving the best results in this extreme challenging and fascinating world. Then, I want to thank Professor Luca Pasquini for his constant support and helpful advices in every part of my scientific activity, from the experimental to the theoretical one. A huge thanks to all my PhD colleagues, who became real friends during this long journey, with whom I shared professional experiences as well as memorable moments outside the working routine. Thanks to Nicola, Luca, Ilaria, Francesco, Jagadesh and, last but not least, all my NANO-mates Lucia, Liviana, Laura, Giancosimo and Fabio. Thanks to Chris and Claudio for hosting me in the Alvra group at the SwissFEL and sharing their knowledge about the incredible world of free electron lasers. I want to thank also the co-workers of the ISM group of the CNR in Tor Vergata and the ISOF group of the CNR in Bologna.

Finally, my heartfelt thanks to all my friends and family.

REFERENCES

1. Paris Agreement | Climate Action. Available at: https://ec.europa.eu/clima/policies/international/negotiations/paris_en. (Accessed: 16th July 2020)

2. Snam. THE HYDROGEN CHALLENGE: The potential of hydrogen in Italy. 0–11 (2019).

3. IEA. Energy Technology Perspectives. *Energy Technol. Perspect.* (2020).

4. IEA. The Future of Hydrogen for G20. Seizing today's opportunities. *Rep. Prep. by IEA G20, Japan* (2019).

5. Nikolaidis, P. & Poullikkas, A. A comparative overview of hydrogen production processes. *Renewable and Sustainable Energy Reviews* (2017). doi:10.1016/j.rser.2016.09.044

6. Hydrogen Europe. Strategic research and innovation agenda for lightweight. (2020).

7. H2FUTURE PROJECT - Technology. Available at: https://www.h2future-project.eu/technology. (Accessed: 16th July 2020)

8. Lewerenz, H.-J. & Peter, L. *Photoelectrochemical Water Splitting. Materials, Processes and Architectures*. (Royal Society of Chemistry, 2013).

9. Khasekev, O. & Heller, A. A Monolithic Photovoltaic-Photoelectrochemical Device for Hydrogen Production via Water Splitting. *Science (80-.).* **280**, 425–427 (1998).

10. Nandjou, F. & Haussener, S. Degradation in photoelectrochemical devices: Review with an illustrative case study. *J. Phys. D. Appl. Phys.* **50**, (2017).

11. FUJISHIMA, A. & HONDA, K. Electrochemical Photolysis of Water at a Semiconductor Electrode. *Nature* **238**, 37–38 (1972).

12. Van de Krol, R. & Gratzel, M. *Photoelectrochemical Hydrogen Production*. *Electronic Materials Science* (Springer, 2012). doi:10.1002/0471711640

13. Chen, Z., Dinh, H. N. & Miller, E. *Photoelectrochemical Water Splitting - Standards, Experimental Methods, and Protocols*. *Springer Briefs in Energy* (2013). doi:10.1021/jm101179e

14. Vayssieres, L. *On Solar Hydrogen and Nonotechnologies*. (John Wiley and Sons, 2009).

15. Nakata, K., Ochiai, T., Murakami, T. & Fujishima, A. Photoenergy conversion with TiO2 photocatalysis: New materials and recent applications. *Electrochim. Acta* **84**, 103–111 (2012).

16. Mahdjoub, N., Allen, N., Kelly, P. & Vishnyakov, V. Thermally induced phase and photocatalytic activity evolution of polymorphous titania. *J. Photochem. Photobiol. A Chem.* **210**, 125–129 (2010).

17. Carp, O., Huisman, C. L. & Reller, A. Photoinduced reactivity of titanium dioxide. *Prog. Solid State Chem.* **32**, 33–177 (2004).

18. Haggerty, J. E. S. *et al.* High-fraction brookite films from amorphous precursors. *Sci. Rep.* **7**, 1–11 (2017).

19. Berger, T. *et al.* Light-induced charge separation in anatase TiO 2 particles. *J. Phys. Chem. B* **109**, 6061–6068 (2005).

20. Yamashita, H. *et al.* Application of ion beam techniques for preparation of metal ion-implanted TiO2 thin film photocatalyst available under visible light irradiation: Metal ion-implantation and ionized cluster beam method. *J. Synchrotron Radiat.* **8**, 569–571 (2001).

21. Umebayashi, T., Yamaki, T., Itoh, H. & Asai, K. Analysis of electronic structures of 3d transition metal-doped TiO 2 based on band calculations. *J. Phys. Chem. Solids* **63**, 1909–1920 (2002).

22. Anpo, M. Use of visible light. Second-generation titanium oxide photocatalysts prepared by the application of an advanced metal ion-implantation method. *Pure Appl. Chem.* **72**, 1787–1792 (2000).

23. Ihara, T., Miyoshi, M., Ando, M., Sugihara, S. & Iriyama, Y. Preparation of a visible-light-active TiO2 photocatalyst by RF plasma treatment. *J. Mater. Sci.* **36**, 4201–4207 (2001).

24. Sahoo, M. *et al.* Physico-chemical processes and kinetics of sunlight-induced hydrophobic ↔ superhydrophilic switching of transparent N-doped TiO2 thin films. *ACS Appl. Mater. Interfaces* **5**, 3967–3974 (2013).

25. Ramos, R. *et al.* Study of nitrogen ion doping of titanium dioxide films. *Appl. Surf. Sci.* **443**, 619–627 (2018).

26. Dozzi, M. V. & Selli, E. Doping TiO2 with p-block elements: Effects on photocatalytic activity. *J. Photochem. Photobiol. C Photochem. Rev.* **14**, 13–28 (2013).

27. Amidani, L. *et al.* Probing long-lived plasmonic-generated charges in TiO2/Au by high-resolution x-ray absorption spectroscopy. *Angew. Chemie - Int. Ed.* **54**, 5413–5416 (2015).

28. Peeters, H. *et al.* Plasmonic gold-embedded TiO2 thin films as photocatalytic self-cleaning coatings. *Appl. Catal. B Environ.* **267**, (2020).

29. Kamarudheen, R., Kumari, G. & Baldi, A. Plasmon-driven synthesis of individual metal@semiconductor core@shell nanoparticles. *Nat. Commun.* **11**, 1–10 (2020).

30. Hamans, R. F., Kamarudheen, R. & Baldi, A. Single particle approaches to plasmon-driven catalysis. *Nanomaterials* **10**, 1–20 (2020).

31. Anpo, M. *Environmentally Begin Photocatalysis: Application of Titanium Oxide-based Materials*. (2010). doi:10.1007/978-1-4614-4605-7

32. Jafari, T. *et al.* Photocatalytic water splitting - The untamed dream: A review of recent advances. *Molecules* **21**, (2016).

33. Berger, T., Monllor-Satoca, D., Jankulovska, M., Lana-Villarreal, T. & Gómez, R. The electrochemistry of nanostructured titanium dioxide electrodes. *ChemPhysChem* **13**, 2824–2875 (2012).

34. Yamashita, H., Ichihashi, Y., Takeuchi, M., Kishiguchi, S. & Anpo, M. Characterization of metal ion-implanted titanium oxide photocatalysts operating under visible light irradiation. *J. Synchrotron Radiat.* **6**, 451–452 (1999).

35. Rossi, G. *et al.* Charge carrier dynamics and visible light photocatalysis in vanadium-doped TiO2 nanoparticles. *Appl. Catal. B Environ.* **237**, 603–612 (2018).

36. Piccioni, A. *et al.* Ultrafast Charge Carrier Dynamics in Vanadium-Modi fi ed TiO 2 Thin Films and Its Relation to Their Photoelectrocatalytic E ffi ciency for Water Splitting. *J.*

Phys. Chem. C (2020). doi:10.1021/acs.jpcc.0c06790

37. Gratzel, M. Photoelectrochemical cells. *Nature* **414**, 338–344 (2001).

38. Allen, J. B. & Larry, R. F. *Electrochemical Methods*. (2011). doi:10.1360/zd-2013-43-6-1064

39. Marcus, R. A. On the Theory of Oxidation-Reduction Reactions Involving Electron Transfer. *J. Chem. Phys.* **24**, (1955).

40. Nozik, A. J. & Memming, R. Physical chemistry of semiconductor-liquid interfaces. *J. Phys. Chem.* **100**, 13061–13078 (1996).

41. Balluffi, R. W., Allen, S. M. & Carter, W. C. *Kinetics of Materials*. (John Wiley and Sons, 2005).

42. Kelly, P. J. & Arnell, R. D. Magnetron sputtering : a review of recent developments and applications. **56**, 159–172 (2000).

43. Ohring, M. *The Materials Science of Thin Films*. (Academic Press, 1992).

44. Adachi, H., Hata, T. & Matsushima, T. *Handbook of Sputter Deposition Technology*. (2012).

45. Sigmud, P. Theory of Sputtering. I. Sputtering Yield of Amarphous and Polyscristalline Targets. *Phys. Rev.* **184**, (1969).

46. Santato, C., Ulmann, M. & Augustynski, J. Enhanced visible light conversion efficiency using nanocrystalline WO3 films. *Adv. Mater.* **13**, 511–514 (2001).

47. Kavan, L. & Grätzel, M. Highly efficient semiconducting TiO2 photoelectrodes prepared by aerosol pyrolysis. *Electrochim. Acta* **40**, 643–652 (1995).

48. Elgrishi, N. *et al.* A Practical Beginner's Guide to Cyclic Voltammetry. *J. Chem. Educ.* **95**, 197–206 (2018).

49. Fabregat-Santiago, F., Garcia-Belmonte, G., Mora-Seró, I. & Bisquert, J. Characterization of nanostructured hybrid and organic solar cells by impedance spectroscopy. *Phys. Chem. Chem. Phys.* **13**, 9083 (2011).

50. Peter, L. M., Li, J. & Peat, R. Surface recombination at semiconductor electrodes. Part I. Transient and steady-state photocurrents. *J. Electroanal. Chem.* **165**, 29–40 (1984).

51. Randles, J. E. B. Kinetics of rapid electrode reactions. *Discuss. Faraday Soc.* **1**, 11–18 (1947).

52. Klahr, B., Gimenez, S., Fabregat-Santiago, F., Hamann, T. & Bisquert, J. Water oxidation at hematite photoelectrodes: The role of surface states. *J. Am. Chem. Soc.* **134**, 4294–4302 (2012).

53. Schnohr, C. S. *X-Ray Absorption Spectroscopy of Semiconductors*. (Springer, Berlin, Heidelberg, 2014). doi:https://doi.org/10.1007/978-3-662-44362-0

54. Van Oversteeg, C. H. M., Doan, H. Q., De Groot, F. M. F. & Cuk, T. In situ X-ray absorption spectroscopy of transition metal based water oxidation catalysts. *Chem. Soc. Rev.* **46**, 102–125 (2017).

55. Grant, B. *Introduction to Xas: A Practical Guide to X-ray Absorption Fine Structure*

Spectroscopy. (2010).

56. Rehr, J. J. & Albers, R. C. Theoretical approaches to x-ray absorption fine structure. *Rev. Mod. Phys.* **72**, 621–654 (2000).

57. Rehr, J. J. & Ankudinov, A. L. Progress in the theory and interpretation of XANES. *Coord. Chem. Rev.* **249**, 131–140 (2005).

58. Rehr, J. J., Kas, J. J., Vila, F. D., Prange, M. P. & Jorissen, K. Parameter-free calculations of X-ray spectra with FEFF9. *Phys. Chem. Chem. Phys.* **12**, 5503–5513 (2010).

59. Wang, M., Árnadóttir, L., Xu, Z. J. & Feng, Z. In Situ X-ray Absorption Spectroscopy Studies of Nanoscale Electrocatalysts. *Nano-Micro Letters* **11**, (2019).

60. Milne, C. J. *et al.* Opportunities for chemistry at the SwissFEL X-ray free electron laser. *Chimia (Aarau).* **71**, 299–307 (2017).

61. Fracchia, M., Ghigna, P., Vertova, A., Rondinini, S. & Minguzzi, A. Time-Resolved X-ray Absorption Spectroscopy in (Photo)Electrochemistry. *Surfaces* **1**, 138–150 (2018).

62. Szlachetko, J. *et al.* A von Hamos x-ray spectrometer based on a segmented-type diffraction crystal for single-shot x-ray emission spectroscopy and time-resolved resonant inelastic x-ray scattering studies. *Rev. Sci. Instrum.* **83**, (2012).

63. Santomauro, F. G. *et al.* Femtosecond X-ray absorption study of electron localization in photoexcited anatase TiO 2. *Sci. Rep.* **5**, (2015).

64. Uemura, Y. *et al.* Dynamics of Photoelectrons and Structural Changes of Tungsten Trioxide Observed by Femtosecond Transient XAFS. *Angew. Chemie - Int. Ed.* **55**, 1364–1367

(2016).

65. Stevie, F. A. & Donley, C. L. Introduction to x-ray photoelectron spectroscopy. *J. Vac. Sci. Technol. A* **38**, 063204 (2020).

66. Hippert, F., Geissler, E., Hodeau, J. L., Lelièvre-Berna, E. & Regnard, J. R. *Neutron and X-ray spectroscopy*. (Springer, 2006).

67. Schultze, M. *et al.* Attosecond band-gap dynamics in silicon. *Sci. Rep.* **346**, 1348–1352 (2014).

68. Baran, T. *et al*. Operando and Time-Resolved X-Ray Absorption Spectroscopy for the Study of Photoelectrode Architectures. *Electrochim. Acta* **207**, 16–21 (2016).

69. Maiuri, M., Garavelli, M. & Cerullo, G. Ultrafast Spectroscopy: State of the Art and Open Challenges. *J. Am. Chem. Soc.* **142**, 3–15 (2020).

70. Cooper, J. K. *et al.* Physical Origins of the Transient Absorption Spectra and Dynamics in Thin-Film Semiconductors: The Case of BiVO4. *J. Phys. Chem. C* **122**, 20642–20652 (2018).

71. Grigioni, I. *et al.* In Operando Photoelectrochemical Femtosecond Transient Absorption Spectroscopy of WO3/BiVO4 Heterojunctions. *ACS Energy Lett.* **4**, 2213–2219 (2019).

72. Vengris, M. Introduction to time-resolved spectroscopy.

73. Berera, R., van Grondelle, R. & Kennis, J. T. M. Ultrafast transient absorption spectroscopy: Principles and application to photosynthetic systems. *Photosynth. Res.* **101**, 105–118 (2009).

74. Rossi, G. *et al.* Charge carrier dynamics and visible light photocatalysis in vanadium-doped TiO<inf>2</inf> nanoparticles. *Appl. Catal. B Environ.* **237**, (2018).

75. Rossi, G. *et al.* Local Structure of v Dopants in TiO<inf>2</inf> Nanoparticles: X-ray Absorption Spectroscopy, Including Ab-Initio and Full Potential Simulations. *J. Phys. Chem. C* **120**, (2016).

76. Jaiswal, R., Patel, N., Kothari, D. C. & Miotello, A. Improved visible light photocatalytic activity of TiO2 co-doped with Vanadium and Nitrogen. *Appl. Catal. B Environ.* **126**, 47–54 (2012).

77. Umebayashi, T., Yamaki, T., Itoh, H. & Asai, K. Analysis of electronic structures of 3d transition metal-doped TiO2 based on band calculations. *J. Phys. Chem. Solids* **63**, 1909–1920 (2002).

78. Perdew, J. P. & Levy, M. Physical content of the exact kohn-sham orbital energies: Band gaps and derivative discontinuities. *Phys. Rev. Lett.* **51**, 1884–1887 (1983).

79. Stampfl, C., Mannstadt, W., Asahi, R. & Freeman, A. J. Electronic structure and physical properties of early transition metal mononitrides: Density-functional theory LDA, GGA, and screened-exchange LDA FLAPW calculations. *Phys. Rev. B - Condens. Matter Mater. Phys.* **63**, 1–11 (2001).

80. Stagi, L., Carbonaro, C. M., Corpino, R., Chiriu, D. & Ricci, P. C. Light induced TiO2 phase transformation: Correlation with luminescent surface defects. *Phys. Status Solidi Basic Res.* **252**, 124–129 (2015).

81. Alhomoudi, I. A. & Newaz, G. Residual stresses and Raman shift relation in anatase TiO2 thin film. *Thin Solid Films* **517**, 4372–4378 (2009).

82. El Koura, Z. *et al.* XANES study of vanadium and nitrogen dopants in photocatalytic TiO_2 thin films. *Phys. Chem. Chem. Phys.* **20**, 221–231 (2018).

83. Zhu, K. R., Zhang, M. S., Chen, Q. & Yin, Z. Size and phonon-confinement effects on low-frequency Raman mode of anatase TiO2 nanocrystal. *Phys. Lett. Sect. A Gen. At. Solid State Phys.* **340**, 220–227 (2005).

84. Barreca, D., Gasparotto, A., Maccato, C., Maragno, C. & Tondello, E. TiO 2 Thin Films by Chemical Vapor Deposition: An XPS Characterization . *Surf. Sci. Spectra* **14**, 27–33 (2007).

85. Stoch, J. & Gablankowska-Kukucz, J. The effect of carbonate contaminations on the XPS O 1s band structure in metal oxides. *Surf. Interface Anal.* **17**, 165–167 (1991).

86. Yan, J. *et al.* Understanding the effect of surface/bulk defects on the photocatalytic activity of TiO2: Anatase versus rutile. *Phys. Chem. Chem. Phys.* **15**, 10978–10988 (2013).

87. casaxps. www.casaxps.com

88. Silversmit, G., Depla, D., Poelman, H., Marin, G. B. & De Gryse, R. Determination of the V2p XPS binding energies for different vanadium oxidation states (V5+ to V0+). *J. Electron Spectros. Relat. Phenomena* **135**, 167–175 (2004).

89. El Koura, Z. *et al.* XANES study of vanadium and nitrogen dopants in photocatalytic TiO 2 thin films. *Phys. Chem. Chem. Phys.* **20**, 221–231 (2018).

90. Siefke, T. *et al.* Materials Pushing the Application Limits of Wire Grid Polarizers further into the Deep Ultraviolet Spectral Range. *Adv. Opt. Mater.* **4**, 1780–1786 (2016).

91. Sarkar, S. *et al.* Hybridized Guided-Mode Resonances via Colloidal Plasmonic Self-Assembled Grating. *ACS Appl. Mater. Interfaces* **11**, 13752–13760 (2019).

92. Leng, W. H., Zhang, Z., Zhang, J. Q. & Cao, C. N. Investigation of the kinetics of a TiO2 photoelectrocatalytic reaction involving charge transfer and recombination through surface states by electrochemical impedance spectroscopy. *J. Phys. Chem. B* **109**, 15008–15023 (2005).

93. Centurioni, E. Generalized matrix method for calculation of internal light energy flux in mixed coherent and incoherent multilayers. *Appl. Opt.* **44**, 7532 (2005).

94. Rossi, G. *et al.* Charge carrier dynamics and visible light photocatalysis in vanadium-doped TiO 2 nanoparticles. *Appl. Catal. B Environ.* **237**, 603–612 (2018).

95. Tamaki, Y. *et al.* Trapping dynamics of electrons and holes in a nanocrystalline TiO2 film revealed by femtosecond visible/near-infrared transient absorption spectroscopy. *Comptes Rendus Chim.* (2006). doi:10.1016/j.crci.2005.05.018

96. Toshitada, Y. *et al.* Identification of Reactive Species in Photoexcited Nanocrystalline TiO2 Films by Wide-Wavelength-Range (400-2500 nm) Transient Absorption Spectroscopy. *J. Phys. Chem. B* **108**, 3817–3823 (2003).

97. Tamaki, Y. *et al.* Dynamics of efficient electron–hole separation in TiO $_2$ nanoparticles revealed by femtosecond transient absorption spectroscopy under the weak-excitation

condition. *Phys. Chem. Chem. Phys.* **9**, 1453–1460 (2007).

98. Rothenberger, G., Moser, J., Gratzel, M., Serpone, N. & Sharma, D. K. Charge carrier trapping and recombination dynamics in small semiconductor particles. *J. Am. Chem. Soc.* **107**, 8054–8059 (1985).

99. Schneider, J. & Bahnemann, D. Strong Transient Absorption of Trapped Holes in Anatase and Rutile TiO 2 at High Laser Intensities. (2018). doi:10.1021/acs.jpcc.8b01109

100. Nunzi, F., De Angelis, F. & Selloni, A. Ab Initio Simulation of the Absorption Spectra of Photoexcited Carriers in TiO2 Nanoparticles. *J. Phys. Chem. Lett.* **7**, 3597–3602 (2016).

101. Sun, J. *et al.* Ultrafast carrier trapping of a metal-doped titanium dioxide semiconductor revealed by femtosecond transient absorption spectroscopy. *ACS Appl. Mater. Interfaces* **6**, 10022–10027 (2014).

102. Ikeda, S. *et al.* Photocatalytic activity of transition-metal-loaded titanium(IV) oxide powders suspended in aqueous solutions: Correlation with electron-hole recombination kinetics. *Phys. Chem. Chem. Phys.* **3**, 267–273 (2001).

103. Sachs, M., Pastor, E., Ka, A. & Durrant, J. R. Evaluation of Surface State Mediated Charge Recombination in Anatase and Rutile TiO2. *J. Phys. Chem. Lett.* **7**, 3742–3746 (2016).

104. Moon, J. A. & Tauc, J. Interference effects in pump-probe spectroscopy of thin films. *J. Appl. Phys.* **73**, 4571–4578 (1993).

105. Pasanen, H. P., Vivo, P., Canil, L., Abate, A. & Tkachenko, N. Refractive index change dominates the transient absorption response of metal halide perovskite thin films in the near

infrared. *Phys. Chem. Chem. Phys.* **21**, 14663–14670 (2019).

106. Enright, B. & Fitzmaurice, D. Spectroscopic determination of electron and hole effective masses in a nanocrystalline semiconductor film. *J. Phys. Chem.* **100**, 1027–1035 (1996).

107. Salvador, P. Hole diffusion length in n-TiO2 single crystals and sintered electrodes: Photoelectrochemical determination and comparative analysis. *J. Appl. Phys.* **55**, 2977–2985 (1984).

108. Tamaki, Y., Hara, K., Katoh, R., Tachiya, M. & Furube, A. Femtosecond Visible-to-IR Spectroscopy of TiO 2 Nanocrystalline Films : Elucidation of the Electron Mobility before Deep Trapping †. 11741–11746 (2009). doi:10.1021/jp901833j

109. Rossi, G. *et al.* Element-specific channels for the photoexcitation of V-doped TiO 2 nanoparticles. *Phys. Rev. B* **96**, 45303 (2017).